TECHNOLOGY • RESEARCH HIGHLIGHTS • VISIONS • SCIENCE
296

Concentrated solar power and circulating fluidized bed power plant hybrids

Final results of the COMBO-CFB project

Elina Hakkarainen | Suvi Suojanen | Matti Tähtinen | Toni Pikkarainen | Antton Tapani | Teemu Sihvonen | Markus Hurskainen |

VTT TECHNOLOGY 296

Concentrated solar power and circulating fluidized bed power plant hybrids

Final results of the COMBO-CFB project

Elina Hakkarainen, Suvi Suojanen, Matti Tähtinen, Toni Pikkarainen, Antton Tapani, Teemu Sihvonen, Markus Hurskainen, Hannu Mikkonen, Jari Lappalainen & Heidi Saastamoinen

VTT Technical Research Centre of Finland Ltd

ISBN 978-951-38-8531-1 (URL: http://www.vttresearch.com/impact/publications)

VTT Technology 296

ISSN-L 2242-1211
ISSN 2242-122X (Online)
http://urn.fi/URN:ISBN:978-951-38-8531-1

JULKAISIJA – UTGIVARE – PUBLISHER

Teknologian tutkimuskeskus VTT Oy
PL 1000 (Tekniikantie 4 A, Espoo)
02044 VTT
Puh. 020 722 111, faksi 020 722 7001

Teknologiska forskningscentralen VTT Ab
PB 1000 (Teknikvägen 4 A, Esbo)
FI-02044 VTT
Tfn +358 20 722 111, telefax +358 20 722 7001

VTT Technical Research Centre of Finland Ltd
P.O. Box 1000 (Tekniikantie 4 A, Espoo)
FI-02044 VTT, Finland
Tel. +358 20 722 111, fax +358 20 722 7001

Cover image: Elina Hakkarainen, VTT Technical Research Centre of Finland Ltd

Preface

Combination of Concentrated Solar Power with Circulating Fluidized Bed Power Plants (COMBO-CFB) project was a joint project to develop hybrid power plant concepts combining concentrated solar power and circulating fluidized bed power plants. The goal of the project was to increase the knowledge on the CSP technology and its opportunities to enhance the renewable centralized power production.

This work was carried out in the COMBO-CFB (Combination of Concentrated Solar Power with Circulating Fluidized Bed Power Plants) research project (40066/14) coordinated by VTT Technical Research Centre of Finland Ltd with funding from Tekes – the Finnish Funding Agency for Innovation.

VTT Technical Research Centre of Finland Ltd and the University of Oulu were the research partners in the project. VTT was the coordinator of the project. Participating companies were Amec Foster Wheeler, Vaisala Oyj and Telog Oy. Pöyry Finland Oy, Energiateollisuus ry and Teknologiateollisuus ry participated to the steering group work as expert members. International collaboration was conducted with DLR (Deutsches Zentrum für Luft- und Raumfahrt e.V.) as a research exchange. Project participated actively to the events organized by SolarPACES (Solar Power and Chemical Energy Systems, A technology collaboration programme of the International Energy Agency).

8.3.2017
Authors

Contents

List of symbols

Abbreviations

BFB	Bubbling fluidized bed
CFB	Circulating fluidized bed
CLFR	Compact linear Fresnel reflector
COMBO-CFB	Combination of concentrated solar power with circulating fluidized bed power plants
CPC	Compound parabolic concentrator
CR	Central receiver
CSP	Concentrated solar power
DMR	Dry methane reforming
DMS	Direct molten salt
DSG	Direct steam generation
EIC	Electric indication and control
EPS	Emission performance standard
ET	Electric transmitter
FC	Flow control
FIC	Flow indication and control
FT	Flow transmitter
FWH	Feedwater preheater
HP	High pressure
HRSG	Heat recovery steam generator
HTF	Heat transfer fluid
IAM	Incidence angle modifier

IP	Intermediate pressure
ISCC	Integrated solar combined cycle
LCOE	Levelised cost of electricity
LFC	Linear Fresnel collector
LHV	Lower heating value
LIC	Level indication and control
LMTD	Logarithmic mean temperature difference
LP	Low pressure
LUVO	*Luftvorwärmer*, engl. air preheating
LT	Level transmitter
MCR	Maximum continuous rating
MPC	Model predictive control
MS	Molten salt
O&M	Operation and maintenance
PCC	Pulverised coal combustion
PD	Parabolic dish
PI	Proportional-Integral –controller
PIC	Pressure indication and control
PT	Pressure transmitter
PTC	Parabolic trough collector
PV	Photovoltaics
RE	Renewable energy
RH	Reheater
R&D	Research and development
SAPG	Solar aided power generation
sCO_2	Supercritical carbon dioxide
SF	Solar field
SG	Steam generator
SH	Superheater
SMR	Steam methane reforming

ST	Solar tower
TL	Turbidity Linke factor

Symbols

A	area
m	mass
P	power
Q	energy
U	energetic upgrade factor
η	efficiency

Subscriptions

ap	aperture
atm	atmospheric
att	attenuation
block	blocking
cl	cleanliness
comp	compressor
cos	cosine
e	electrical
L	longitudinal
I	first law
loss	thermal loss
net	net
opt	optical
p	pump
rec	receiver
refl	reflection
shade	shading
spill	spill
T	transversal

tur	turbine
th	thermal
0	peak

1. Introduction

Concentrated solar power (CSP) and conventional solid fuel-fired hybrid power plant is one of the possible technical solutions to increase the share of renewable energy (RE) in the energy system and to decrease greenhouse gas emission levels and fuel consumption of conventional solid fuel-fired power plants. CSP technology has been attracting more and more attention due to the characteristics of solar irradiation as a clean, free and non-exhausting source of energy. In addition, conventional solid fuel-fired power plants are being criticized due to their environmental impacts, such as pollutions, greenhouse gas emissions and diminishing of fossil fuel resources.

1.1 Novel concentrated solar power and conventional solid fuel-fired hybrid power plant concepts

In a novel CSP and conventional solid fuel-fired hybrid power plant, the solar field is strongly integrated with the power cycle of the solid fuel-fired power plant. The solar field and the conventional power plant share the main components of the power cycle, such as turbines, condenser and feedwater preheaters. The main objective of the novel hybrid CSP plant is to produce electricity reliably and according to demand with less fuel and emissions, while improving the system efficiency, lowering the costs of CSP technology and extending the operation timeframe and market areas of CSP technology. The hybrid CSP plant is an attractive option for power generation in countries, which are rich in solar resources, such as Australia, China, India (Suresh et al. 2010), South Africa (Pierce et al. 2013) and the United States (Lovegrove et al. 2012). However, only a few CSP and solid fuel-fired hybrid power plants are operational (Table 1), even though hybrid CSP plants are not a novel research area. The first serious attempts to study hybrid CSP plants were conducted in the 1970's due to the oil crisis (Petrov et al. 2012).

Table 1. Operational and planned CSP and conventional solid fuel-fired hybrid power plant concepts.

Power plant	Country	Status	CSP technology/ heat transfer fluid	Solar [MW_e]	Fuel	Solid fuel-fired [MW_{th}/MW_e]
Termosolar Borges [1]	Spain	Operational	Parabolic Trough/ Thermal oil	22.5 (total)	Biomass /gas	44 MW_{th}
Liddell Power Station [2]	Australia	Operational	Linear Fresnel/ Water	6.0	Coal	2000 MW_e
Kogan Creek [3,4]	Australia	Withdrawn	Linear Fresnel/ Water	44.0	Coal	750 MW_e
Sundt Solar Boost [5]	USA	Develop-ment	Linear Fresnel/ Water	5.0	Coal/gas	156 MW_e

[1](NREL, 2016), [2](AREVA Solar, 2010), [3](AREVA Solar, 2011a), [4](Arena, 2016), [5](AREVA Solar, 2012)

CSP integration can be done to repower an existing power plant unit or by constructing a new CSP hybrid plant. However, the CSP retrofit installations need to be carefully considered, since the lifetime of existing fossil fuel-fired power plants should not be extended and investments in RE power should not be delayed. For example, coal-fired power plants are designed to have a lifetime of approximately 40 years, whereas CSP plants can currently require lifetime of up to 20 years in order to break even in investment costs. Peterseim et al. (2014a) suggest that retrofits should not be done to units older than 10 to 15 years, as in older units the short operation time of the hybrid system can offset the avoided CO_2 emissions due to the typically low solar share. (Peterseim et al. 2014a) Thus, it may be more attractive to construct new hybrid plants, in which the size and performance of the shared components are optimized according to the thermal power of the solar field, while maximizing the achievable solar share (Petrov et al. 2012).

1.2 Key drivers for the development of hybrid CSP concepts

There are multiple drivers for the development and implementation of hybrid CSP plants. These include:

1. Generation of dispatchable renewable energy.
2. Lowering the levelised costs of electricity (LCOE) with respect to stand-alone CSP.
3. Extension of the market area for CSP technology.
4. Assisting the conventional solid fuel-fired power plants to meet their emission reduction targets.
5. Supporting the sustainable use of biomass-based fuels.
6. Improving efficiency compared to stand-alone CSP and solid fuel-fired solutions.
7. Improving solar energy yield compared to stand-alone CSP solutions.

Increasing share of variable RE production sets challenges to the stability of the power grid due to the intermittent nature of wind and solar resources. The chal-

lenges include rapid and unpredictable changes in power production, sudden disappearances of power generation and poor availability of energy sources. In hybrid CSP plant, the electricity production can be stabilised by utilizing all the available solar energy and covering the rest of the electricity demand with solid fuels. (Paska et al. 2009)

Hybrid CSP plants could boost the CSP industry by reducing the LCOE of CSP technology (Peterseim et al. 2013). The LCOE of CSP in utility-scale was in the range of 170 to 280 USD/MWh in 2014. On the other hand, the LCOE of fossil fuel-fired power plants was in the range of 45 to 140 USD/MWh, and the LCOE of PV was in the range of 60 to 400 USD/MWh, as can be seen in Figure 1. (International Renewable Energy Agency 2015) The possible LCOE reductions of CSP technology are mainly due to the joint use of equipment in the case of hybrid plant and learning curve reductions like in the case of PV and wind power technologies (Peterseim et al. 2013). IEA foresees LCOE of 64 − 94 USD/MWh for stand-alone CSP with storage in 2050 (International Energy Agency 2014).

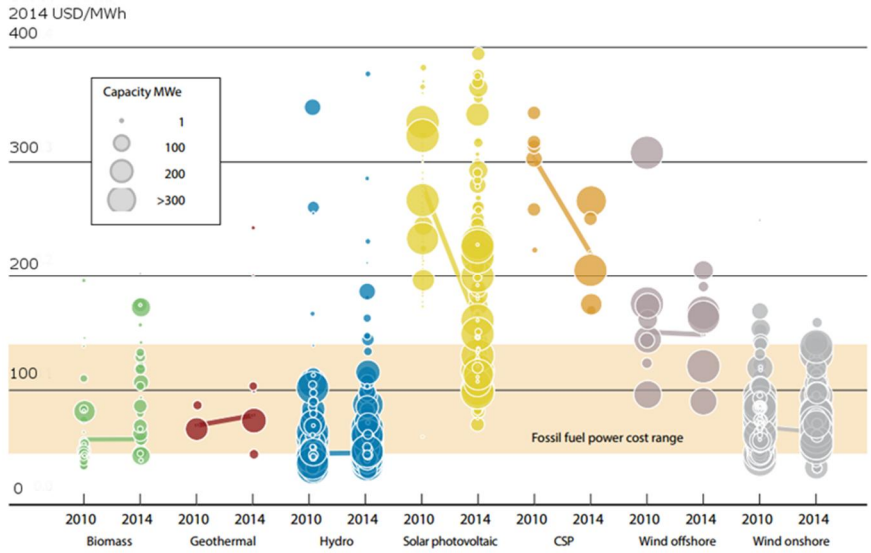

Figure 1. The LCOEs of utility-scale renewable technologies in 2010 and 2014 (Modified from IRENA 2015).

In February 2016, global operational CSP capacity was 4.75 GW (SolarPACES 2016). CSP capacity represents approximately 0.08% of the world's installed power generation capacity, which was 6,163 GW in 2014 (International Energy Agency 2015). The share of CSP capacity is relatively small compared to photovoltaic (PV) and wind power technologies and to conventional solid fuel-fired power plants. Installed PV and wind power capacities are about 40 and 70 times higher than CSP capacity, respectively. In 2014, installed PV capacity was 176 GW and wind power capacity 350 GW. (International Energy Agency 2015) The low share

of CSP is mainly due to a gradual learning curve of the technology (Petrov et al. 2012), expensive costs of the technology (Peterseim et al. 2013) and the current economic and financial crisis.

Hybrid CSP plants can extend the market area of CSP technology from typically arid areas to the semi-arid and temperate areas with lower DNI than suitable for stand-alone solutions. Typically, stand-alone CSP plants require annual average direct normal irradiance (DNI) level over 2,000 kWh/m^2/year, and the most promising areas locate on the "solar belt" between 20 to 40 degrees latitude North and South (Petrov et al. 2012). These are, for example, the North African desert, South Africa, Central and Western Australia, the Southwest United States and Southern Spain. In the case of hybrid CSP plants, even broader areas may be considered, as the power production is supported by the conventional power plant. According to Peterseim et al. (2013), CSP hybrids can be located in areas where the annual average DNI level is over 1,700 kWh/m^2/year. (Peterseim et al. 2013) This brings the hybrid technology closer to load centres and locations with higher biomass potential.

The CSP integration can assist conventional solid fuel-fired power plants to reduce their fuel consumption and CO_2 emission level. The emission performance standards (EPS) indicate a CO_2 emission level of 420 – 550 gCO_2/kWh (Figure 2). Canada has presented an EPS limit of 420 gCO_2/kWh for new and old fossil-fired units (Canadian Environmental Protection Act 2016). The EPS of European Investment Bank prevents banks from lending producers, which emit more than 550 gCO_2/kWh (European Investment Bank 2013). As a result, CO_2 emission level has to be reduced by at least 33% in a reference plant, which combusts 100% coal with net efficiency of 44%. For current average coal-fired power plants, the CO_2 emission level has to be reduced by over 40%.

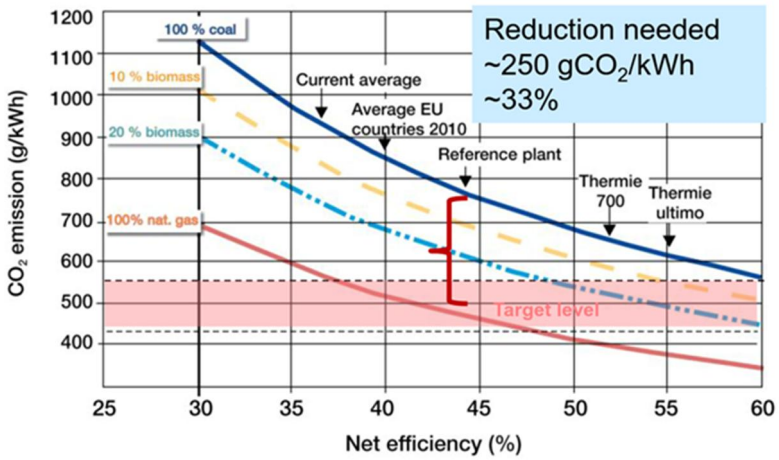

Figure 2. CO_2 emission reduction possibilities for conventional power plants.

Biomass sustainability, availability and resource efficiency are key aspects for bioenergy production. The solar share in the hybrid power plant and the increased overall efficiency decrease the use of biomass and, thus, increase the year-round availability of the biomass. With hybrid solutions, biomass combustion can be expanded to areas with lower biomass resource density. This makes for example Southern Spain very attractive for hybrid technology when considering moderate DNI resource and identified agricultural reside resources. The biomass supply was some 10% of the total world's energy supply in 2012, and approximately 50% of the bioenergy was consumed in developing countries for traditional uses with a very low efficiency (International Renewable Energy Agency 2015). Therefore, it is essential to develop affordable technologies that increase the electrical efficiency of biomass combustion. According to IRENA, the optimal size for biomass CHP plants appears to be around 20 MW_e in typical feedstock conditions in Europe, when taking into account the reasonable feedstock sourcing distance of <50 km. Thus, the reduction in fuel consumption by solar field integration is important to reduce the biomass sourcing distance and to thereby increase sustainability (resources are usually scarce in sunny regions).

The conservation of fuel resources can be further supported by improving the efficiency of energy system. Compared to stand-alone CSP and conventional power plants, the hybrid CSP plant has higher first and second law efficiencies (Hu et al. 2010; Gupta et al. 2009). In addition, solar energy can be utilized more efficiently in a hybrid plant compared to a stand-alone solution. The hybrid CSP plant has higher solar-to-electricity conversion efficiency (Yan et al. 2010) and up to 25% greater annual electricity generation (Pierce et al. 2013) compared to stand-alone CSP plant.

1.3 Structure of the COMBO-CFB project

The main objective of the project "Combination of Concentrated Solar Power (CSP) with Circulating Fluidized Bed (CFB) power plants" (COMBO-CFB) was to develop innovative, flexible and high-efficient hybrid concept, in which solar thermal energy is integrated with a steam power plant. The COMBO-CFB brought together different technologies and know-how with strong industrial contribution on research to ensure the performance of the novel hybrid concept (Figure 3). Amec Foster Wheeler's long-term experience in CFB boiler design and combustion behaviour was utilized to find the optimal boiler solution for the hybrid concept and to take better into account limitations related to the boiler design, in particular to the design of heat transfer surfaces. Vaisala provided insights for the solar irradiance forecasting and required forecast resolution and time horizon, enabling prediction of upcoming load changes. Telog and University of Oulu supported the concept development in terms of the solar field requirements and upper level coordination and optimisation of the plant.

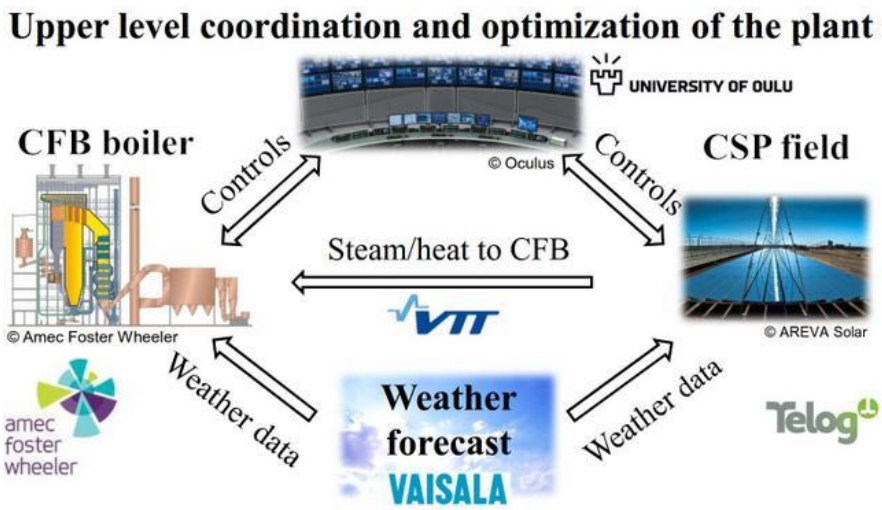

Figure 3. The approach and partners in the COMBO-CFB project.

The novel hybrid concept is required to be flexible in operation while utilizing the joint infrastructure and balancing the distributed intermittent production. The concept development in COMBO-CFB project is carried out through theoretical and experimental research and through dynamic modelling and simulation (Figure 4).

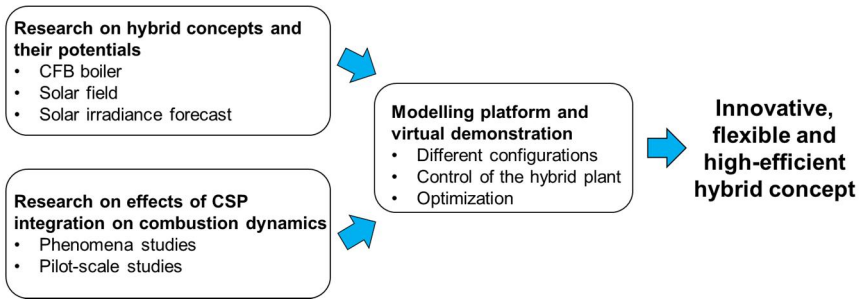

Figure 4. Main research topics and objective of the COMBO-CFB project.

The research on hybrid concepts and their potentials includes investigation of CFB boilers, solar fields and weather forecasting in order to gather information for the modelling and virtual demonstration. The research on effects of CSP integration on combustion dynamics includes test sets for a pilot-scale CFB boiler, in which the combustion phenomena and emission formation were studied during rapid load changes typical for a hybrid CSP plant. In modelling platform and virtual demonstration, multiple CSP technologies and hybrid concepts were dynamically modelled and simulated in order to analyze the interactions between the solar field and the steam boiler, to develop control strategies, to analyse the effects of different hybridisation schemes and to define and compare performance figures.

2. Stand-alone and hybrid concentrated solar power technologies

A typical concentrated solar power (CSP) plant can be divided into three main subsystems; a solar collector field, a solar receiver and a power conversion system (Figure 5). The solar irradiation is redirected and concentrated by on reflector into a small area called as a receiver. In the receiver, solar energy is absorbed to a heat transfer fluid (HTF), which flows either directly or indirectly to the power block to generate electricity. An energy storage system can be added to the plant in order to enhance performance and increase the capacity factor. (Barlev et al. 2011; Conlon et al. 2011)

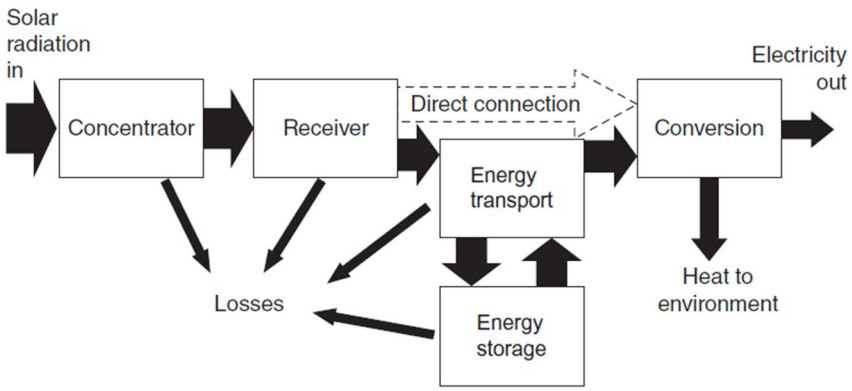

Figure 5. Subsystems of a typical CSP power plant (Lovegrove et al. 2012).

The HTF is commonly thermal oil, molten salt, organic fluid or water, of which thermal oils are mostly used today. Air and other gases as well as liquid metals are also potential HTFs, but they are still relatively uncommon. Thermal oils, molten salts and organic fluids require an additional heat exchanger between the solar field and the power block. When water/steam is applied in the solar field for direct steam generation (DSG), no additional heat exchanger between the solar field and the power block is needed. This increases the net efficiency of the plant, simplifies the plant configuration and lowers investment costs compared to other HTFs. (Vignarooban et al. 2015) Thermal storage systems based on molten salts as

storage medium are currently applied to CSP plants (Vignarooban et al. 2015), whereas thermal storage systems for DSG plants are being developed (Laing et al. 2011). In the CSP plants using oil as HTF, heat can be stored in a two-tank storage system containing the heat transfer fluid itself or molten salt. The latter option requires an oil/salt heat exchanger. (Birnbaum et al. 2010) In the case of molten salt solar field, heat can be directly stored to a storage system. These heat transfer fluid also require an additional heat exchanger between the storage and power cycle (Birnbaum et al. 2010).

A desired HTF has high boiling point, high thermal stability, high thermal conductivity, high heat capacity, low melting point, low vapour pressure at high temperatures, low corrosion with metal alloys, low viscosity, and low costs (Vignarooban et al. 2015). Thermal oils are preferred due to their relatively low volatility and thus low stress on the absorber tubes. However, thermal oils are not applied in high-temperature applications, since oils start to degrade at around 400 °C. (Fernández-García et al. 2010) In addition, another issue is the high cost of thermal oils (Vignarooban et al. 2015). Higher temperatures up to 550 °C can be reached with water, which is less expensive than other HTFs and has no environmental risks (Fernández-García et al. 2010). The main problems of water are the water scarcity in desert regions (Vignarooban et al. 2015) and high vapour pressure at high temperatures, which results in higher stress on the receiver tubes than compared to other HTFs (Barlev et al. 2011). In addition, water may freeze in the tubes (Fernández-García et al. 2010). With molten salts, even higher temperatures up to 800 °C are anticipated. Currently temperatures over 500 °C are achievable. Molten salts have been widely studied due to their advantages, which include high operation temperature, high heat capacity, high stability at high temperatures and low vapor pressure. However, the high operation temperature induces corrosive issues with the metal alloys. (Vignarooban et al. 2015)

CSP technology can be applied to generate electricity in a stand-alone (Chapter 2.1) or in a hybrid CSP power plant (Chapter 2.2). In the case of COMBO-CFB project, hybrid technologies applying solid fuel-fired power plants were in the scope of reserach. Thus, other hybridisation possibilities were excluded, such as hybridisation with combined cycle power plant, geothermal power plant and wind power plant (Peterseim et al. 2014a). In addition to electricity generation, utilization of the high-temperature heat from solar field in other processes was investigated in the COMBO-CFB. The heat can be used for example in the production of synthetic fuels called as solar fuels (Chapter 2.3). Other possible processes were excluded, such as air conditioning and cooling, desalination and enhanced oil recovery.

2.1 Stand-alone concentrated solar power technologies

Stand-alone CSP technologies can be divided into four types: parabolic trough collectors (PTC), solar towers (ST) called also as central receivers (CR), linear Fresnel collectors (LFC), and parabolic dishes (PD) (Barlev et al. 2011) (Figure 6).

Currently, PTCs represent over 95% of the installed capacity, CRs approximately 3%, LFCs approximately 1% and PDs less than 1% (Vignarooban et al. 2015).

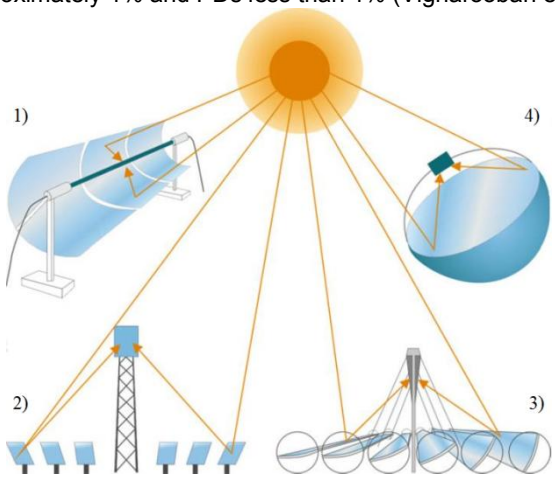

Figure 6. Four main CSP technologies: 1) parabolic trough 2) central receiver 3) linear Fresnel and 4) parabolic dish (Modified from Guerrero-Lemus & Martínez-Duart 2013).

CSP technologies can be classified by the focus arrangement (a focal point or a focal line) and by the receiver type (fixed or mobile) (Figure 7). In addition, CSP technologies can be classified by the concentration ratio, which describes the intensity of concentrated radiation; geometric concentration ratio is determined as a ratio of collector aperture area to receiver area. Line focusing systems concentrate the irradiation by 50-100 times, and the corresponding value for point focusing systems is from 500 to several thousands. (Lovegrove et al. 2012)

Receiver type \ *Focus type*	***Line focus*** *Collectors track the sun along a single axis and focus irradiance on a linear receiver. This makes tracking the sun simpler.*	***Point focus*** *Collectors track the sun along two axes and focus irradiance at a single point receiver. This allows for good receiver efficiency at higher temperatures.*
Fixed Fixed receivers are stationary devices that remain independent of the plant's focusing device. This eases the transport of collected heat to the power block.	Linear Fresnel reflectors	Towers
Mobile Mobile receivers move together with the focusing device. In both line focus and point focus designs, mobile receivers collect more energy.	Parabolic troughs	Parabolic dishes

Figure 7. CSP technologies classified by focusing arrangement and receiver type (International Energy Agency 2014).

PTCs (Chapter 2.1.1), LFCs (Chapter 2.1.2) and CRs (Chapter 2.1.3) are commonly used in utility-scale Rankine cycles, whereas PDs are often used in 1−30 kW_e sized modular power generation systems with a Stirling or Brayton engine (Zhu et al. 2014). Thus, PDs are excluded from this report. Identifying the ideal CSP technology to a specific power plant location is highly dependent on local conditions, such as DNI and climate, land and water availability, and topography (Peterseim et al. 2013).

2.1.1 Parabolic trough technology

Parabolic trough collector consists of a group of parabolic reflectors, which are assembled as long troughs. Troughs are assembled in parallel to form a solar field. Reflectors are usually coated with silvered acrylic, which reflects the sunbeams onto a receiver tube mounted in the focal line of the parabola (Figure 8). The receiver tube is a black metal pipe, which is encased within a glass pipe in order to limit heat loss by convection. A vacuum is placed between the casings in order to also prevent heat loss by convection. The metal tube is covered with a selective coating, which enhances high solar absorbance and low thermal emittance. In addition, the glass tube is covered with an anti-reflective coating, which enhances transmissivity. (Barlev et al. 2011) PTCs use typically thermal oil or organic fluid as a HTF, but a few plants use molten salt, one plant applies direct steam generation and one plant uses air as a HTF (NREL 2016).

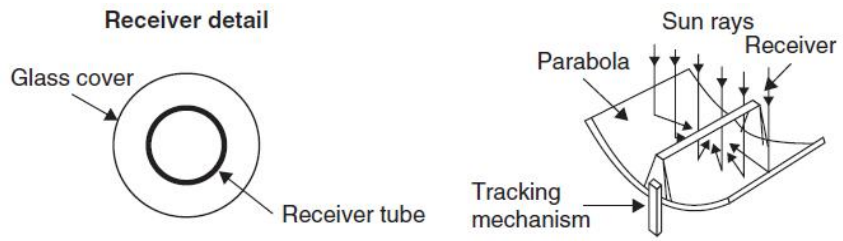

Figure 8. Schematic of a PTC collector (Kalogirou 2014).

The reflector and receiver tube of the PTC move in tandem with the sun in order to keep solar irradiation focused on the receiver tube throughout the day. PTCs are mounted on a single-axis sun-tracking system, which is oriented either East-West or North-South. The East-West oriented field tracks the sun from South to North, whereas the North-South oriented field tracks the sun from East to West. The choice of tracking mode depends on the need of energy during winter and summer, and also on the application. The annual output is more constant in East-West oriented field, which collects more energy in winter and less in summer than North-South oriented field. However, North-South oriented field provides slightly more thermal energy annually (Barlev et al. 2011; Kalogirou 2014). North-South

orientation is used in all commercial PTC plants, since the yearly production is maximised (Fernández-García et al. 2010).

A major advantage of PTCs is the maturity of the technology (Barlev et al. 2011; Kalogirou 2014), as considerable experience of the manufacturing, installation and operation of the collectors has been gained, and the technology is developed and marketed by a small commercial industry. Most of the operating PTC plants have capacities in the range of 14–100 MW_e, but some larger plants are under construction and development. The world's largest PTC power plant is a 280 MW_e plant, Solana, located in Arizona USA. (NREL 2016) The solar-to-electricity efficiency of parabolic troughs is around 14−16% and the capacity factor is in the range of 25% to 30% depending on the location. By adding a molten salt storage system to the solar field, the capacity factor can be increased to over 40%. (IEA-ETSAP & IRENA 2013)

However, PTCs have some challenges. One challenge is the exposure to wind drag. As a result, the tracking system needs to be robust enough to account for wind loads and prevent deviations from normal incidence angle between the solar irradiation and the reflector (Barlev et al. 2011). Therefore, investment costs are higher compared to using flat reflectors. Another challenge associated with PTCs is thermal uniformity in the receiver tube. The heat input of the receiver tube is asymmetric, which causes a temperature difference between the heated and non-heated side of the receiver tube. The temperature difference induces thermal stress on the wall of the receiver tube. This problem concerns especially DSG applications due to the two-phase flow and evaporation inside the tube. In addition, the operating pressure inside the receiver tube superposes the thermal stress especially in the joints between the collectors. The amount of overall stress depends on the wall thickness and on the chosen material, and needs to be considered at the design phase of the system. (Hirsch et al. 2014)

2.1.2 Linear Fresnel technology

Linear Fresnel technology is similar to the PTC technology, since several linear Fresnel collectors can be used to approximate the parabolic shape of PTC. Unlike PTC, LFC consists of multiple flat reflectors on the ground, which concentrate solar irradiation onto a receiver tube (Figure 9). The receiver tube locates on a tall tower above and along the arrays of reflectors. (Barlev et al. 2011; Kalogirou 2014) LFCs have not reached their full industrial maturity as only a few of the existing and planned CSP plants use LFC technology. Most of the existing LFC plants use water as HTF, and the technical improvements of the collector have made LFCs suitable for high-temperature CSP applications to generate electricity at utility-scale. Most of the operating LFC plants have capacities in the range of 0.25–30 MW_e (NREL 2016), but the world's largest LFC power plant is a 100 MW_e plant, Dhursar, located in Dhursar, Rajasthan, India (Reliance Power Ltd 2014).

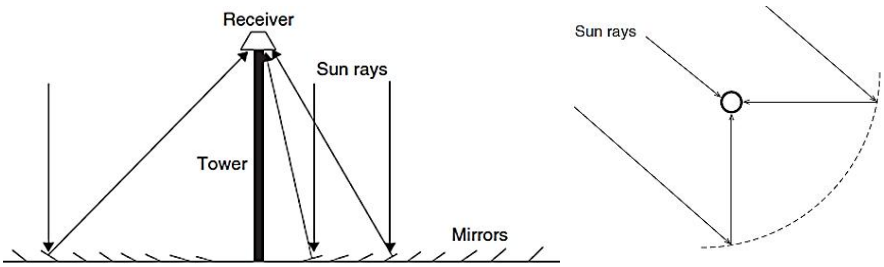

Figure 9. Schematic of LFC field and the receiver (Modified from Kalogirou 2014).

LFCs have some advantages over PTCs. One advantage is the fixed receiver, which does not track the sun. Therefore, only the flat reflectors track the sun, which makes tracking simpler, more accurate and more efficient than with mobile receivers. (Barlev et al. 2011) Another advantage is the lower price due to the flat and elastic reflectors, which are cheaper to produce than parabolic troughs. Furthermore, the reflectors can vary by size and by arrangement, and the concentration ratio can be increased without increasing the wind load due to the flexible architecture of LFCs. This provides a variety of different applications with different target temperatures. (Zhu et al. 2014) In addition, LFCs have lower land requirement and cleaning water consumption than other CSP technologies, which lowers the costs even further (Peterseim et al. 2013). LFCs can also withstand higher operation pressures and temperatures than PTCs due to their fixed receiver configuration, which reduces the need for heat and pressure resistant joints (Popov 2011).

The disadvantage of the LFRs is larger optical losses compared to PTCs due to shading and blocking of solar irradiation between adjacent collector rows. Thus, the LFCs have lower annual thermal power output than PTCs especially during early mornings and late afternoons, and also in winter. However, the optical losses can be compensated by increasing the concentration ratio and the size of the solar field or by building a taller receiver tower, but these modifications increase costs. (Zhu et al. 2014)

One solution for the shading and blocking has been developed by Mills and Morrison at Sydney University, Australia (Kalogirou 2014). The developed compact linear Fresnel reflector (CLFR) uses at least two receiver towers, which allows the individual reflectors to focus sunbeams on either one of the towers (Figure 10). Thus, closely packed reflectors avoid shading and blocking, and the size of the solar field and the height of the receiver tower can be reduced. Furthermore, CLFR field decreases the investment costs, which include ground preparation, array substructure, tower structure and steam lines. In addition, thermal losses from the steam lines are smaller. CLFR provides maximum system output with limited ground area if the technology is applied to urban area or next to an existing power plant. However, a more sophisticated tracking mechanism has to be applied to the CLFR field compared to the LFC field, and the maintenance costs of CLFR field are higher. (Zhu et al. 2014)

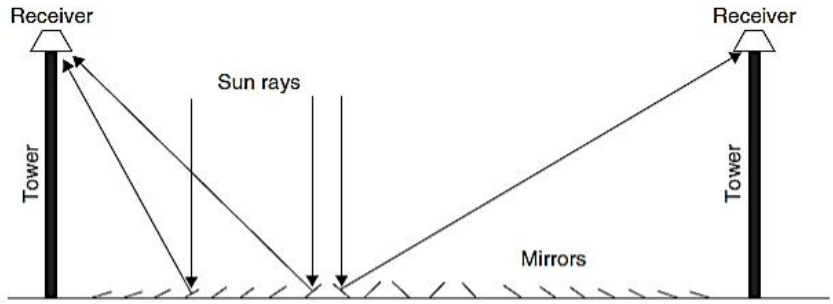

Figure 10. Schematic of CLFR field (Kalogirou 2014).

In addition to CLFR, some other innovations have been made in order to compensate the lower optical efficiency. One innovation is the use of secondary reflector whilst using a single receiver tube (Figure 11a). This increases the optical performance of the collector, but the design of the secondary reflector is difficult to optimize. (Zhu et al. 2014) Another innovation is the addition of an inverted cavity receiver with a planar array of boiling tubes (Figure 11b). This trapezoidal multi-tube receiver uses non-vacuumed receiver tubes, and sidewall insulation is added to reduce thermal loss. However, thermal loss can be very significant from this kind of receiver whilst producing steam at temperature higher than 400 °C (Zhu et al. 2014).

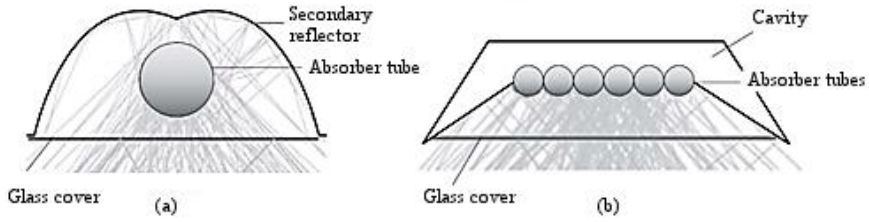

Figure 11. The two main types of LFC receiver design a) single tube cavity receiver with secondary reflector and b) multi-tube trapezoidal cavity receiver (Modified from Lovegrove et al. 2012).

All the reflector and receiver innovations have further reduced costs of LFCs (Barlev et al. 2011). The US Department of Energy has identified CSP plants with LFCs to be the potential pathway to reach the level of LCOE, which can be cost-competitive with conventional power plants without any incentives or government subsidies (Zhu et al. 2014).

2.1.3 Central receiver technology

Central receiver plants exist in wide range of scales from few megawatts to several hundred megawatts. Largest central receiver plant is currently operating in Ivanpah, California and plants of comparable size are under construction in China, South Africa and Chile. Typical heat transfer fluids are water, molten salt or oil. Molten salt has gained popularity due to good heat transfer properties and the ability to use thermal energy storage. In case of water, high pressure steam is produced and it is used to directly drive turbines to produce electricity. When molten salt or oil is used as the heat transfer medium, a heat exchanger is also required to transfer heat into a steam loop, wherein electricity is generated with a conventional steam turbine. Other heat transfer mediums such as air or solid particles can be used as well, but their uses are currently limited to smaller scale research facilities and are not prevalent in the industry.

One intriguing prospect of central receiver systems is the ability to use high temperature thermal energy storage. While other types of solar collectors can use thermal storage, central receiver plant can achieve higher efficiencies and storage capacities due to higher receiver temperatures. When molten salt is used as heat transfer medium, the hot salt from the receiver can be circulated through a hot storage tank when solar radiation is in excess to the needs of the grid. Conversely, when the sun does not shine, hot salt is circulated from the hot storage tank through the steam generator. Illustration of a central receiver plant with salt based heat transfer loop, salt storage and separate steam generator is shown in Figure 12.

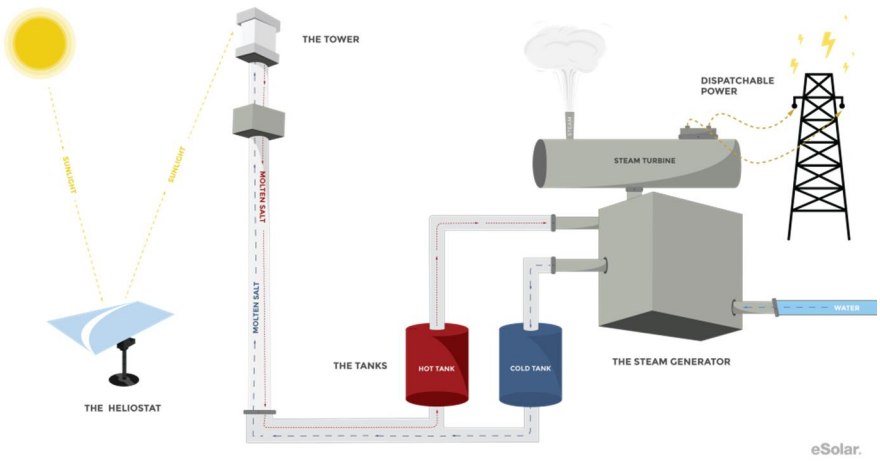

Figure 12. Central receiver power plant with molten salt storage (eSolar).

The mirrors are most commonly arranged in radial pattern around the receiver, surrounding the receiver partially or entirely. On the Earth's northern hemisphere, fields are commonly arranged on the norther side of the receiver, since field effi-

ciency is the highest in this configuration. The fields of the Spanish Planta Solar facilities are arranged this way as shown in Figure 13. Similarly south field is the most optimal on the southern hemisphere. Surrounding field is most optimal close to the equator where the sun shines directly overhead most of the year. The difference between north and surrounding fields becomes greater when moving to higher latitudes, as the sun shines at steeper angles, and parts of the field is forced to reflect the light at unfavourable angles.

Figure 13. Planta Solar power plants PS10 and PS20 with north field (Müller-Steinhagen 2013).

However, overall cost of construction needs to be considered in deciding field layout. Greater performance may be achievable with surrounding field even when north field would theoretically be more optimal, because a single receiving tower can be used with larger number of heliostats using a surrounding field, lowering the costs. Local light attenuation and spill losses also become a limiting factor in a large north field, as the farthest mirrors operate suboptimally. The Crescent Dunes power plant, as an example, is situated in comparable latitudes as Planta Solar and uses surrounding field instead of north field configuration.

Current commercial solar projects are focused primarily on large plants with very large unit size of hundreds of megawatts. This has the clear disadvantage of long construction times and difficulty in estimating costs and performance. Some interest exists for smaller scale facilities such as the Greenway Mersin power plant in Turkey and markets exist for smaller companies. Esolar in particular uses decidedly smaller towers and fields focusing on lowering costs by simplifying construction and high volume manufacturing of the power plant components. These plants are to be constructed modularly in required quantities to accommodate any plant size, while keeping the costs more predictable than large unit installations.

Unlike in the case of PTC and LFC technologies, in central receiver systems the sun tracking is done with mirror panels mounted on armatures that turn on two axes (Figure 14) instead of single-axis tracking.

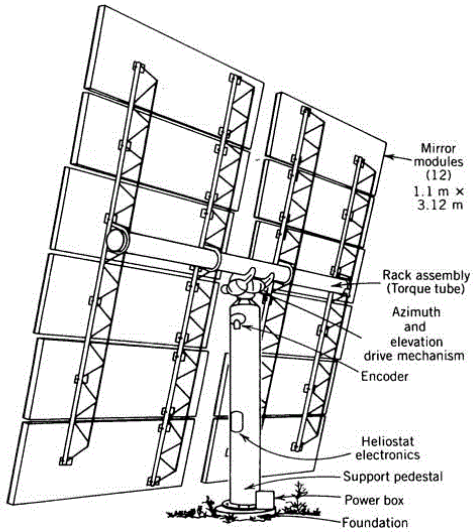

Figure 14. Single heliostat assembly (Southern California Edison).

At the focus point of the collector is the receiver. A simple receiver consists of vertical pipes arranged into a membrane wall in shape of a plane or a cylinder. Heat transfer fluid is passed through the pipes where it heats up to a high temperature. If water is used as the fluid, portion of the pipes can be used as boilers and others as superheaters. Many solar projects have opted to using molten salt as HTF, which makes receiver construction and operation simpler as there occurs no phase change inside heating tubes. This configuration requires separate steam generator for the power conversion.

Cavity receiver encloses high temperature surfaces onto a cavity with a smaller aperture area without trading off absorber surface area. Small aperture leads to smaller emission and convection losses on the receiver. Cavity receiver is structurally more complex than external receiver, which will increase receiver construction cost, but higher efficiencies can lead to smaller required collector area, resulting in savings from other parts of the project. Cavities can be only partial such is the case with the PS10 project (Romero-Alvarez & Zarza 2007), wherein simpler cavity construction is used to gain moderate increases in receiver efficiency.

Cavities can be open to the atmosphere, i.e. there is no window in the aperture, and light can enter the cavity unobstructed. Radiation losses remain low, but in strong wind conditions there can still be convection losses through open apertures. Fully closed cavity has negligible convection losses caused by wind, but they must have a transparent window that can pass high solar fluxes through, which increases the size and mass of the receiver. Windowed receiver can be

pressurized, which increases heat transfer properties in cases where gas is used as heat transfer medium. Higher temperatures can be used as well, which allows using Brayton cycle gas turbines in a combined cycle power plant. Figure 15 shows a pressurized cavity receiver with a volumetric absorber. This concept has been demonstrated at Plataforma Solar de Almería at temperatures up to 1,050 ºC and pressures up to 15 bar, with 230 kW output power. (Müller-Steinhagen 2013)

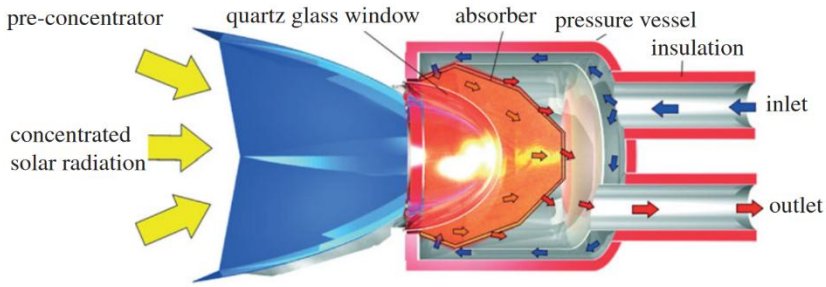

Figure 15. Pressurized volumetric cavity receiver (Müller-Steinhage 2013).

Volumetric receivers work by drawing in gas through porous ceramic material. The gas can be air directly from atmosphere, or any suitable gas contained within the receiver loop, if the receiver is closed to the atmosphere. Ceramic materials can withstand higher temperatures than metallic receivers, but have poorer heat conduction properties through the material. In a volumetric receiver, airflow through the porous material aids in keeping the bulk of the material at more uniform temperature even deeper behind the surface, which greatly increases the heat transfer contact area. This allows more gas to be passed through the receiver and also increases the structural durability under varying conditions.

2.2 Hybrid concentrated solar power technologies for electricity production

Operation modes of hybrid CSP plants for electricity production can be roughly divided in two categories: 1) Power boost mode, in which more electricity is produced with the same amount of fuel (Figure 16, left), or 2) Fuel saving mode, in which the same amount of electricity is produced with less fuel (Figure 16, right).

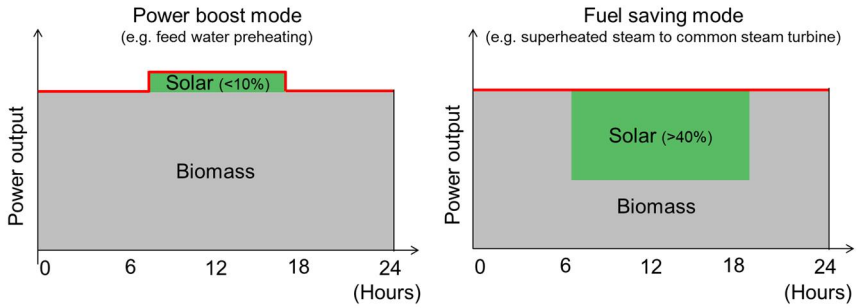

Figure 16. Operation modes of hybrid CSP plants (Modified from Yan et al. 2011).

Both operation modes are realistic, as modern turbines are capable of handling increased steam mass flows up to 110% of the rated turbine capacity (Petrov et al. 2012). During sunshine peak hours, the power boost mode is particularly suitable to meet the electricity demand, which increases due to air conditioning. In addition, Petrov et al. (2012) suggest power boost mode for new hybrid plants, which have inbuilt flexibility to utilize the solar augmentation while maximising equipment usage (Petrov et al. 2012). Peterseim et al. (2013) propose the power boost mode for plants with low CO_2 emissions and the fuel saving mode for plants, which use expensive fuels and generate high level of CO_2 emissions (Peterseim et al. 2013).

The solar field can be integrated in parallel with different power cycles, such as Rankine cycle, combined cycle, Brayton cycle and Stirling cycle. The most mature hybrid CSP solution includes a parabolic trough solar field using thermal oil and combined cycle gas turbine plant using natural gas (Table 13, Appendix A). Solar thermal energy is transferred through a heat exchanger to the heat recovery steam generator (HRSG). The solution is also called as an integrated solar combined cycle (ISCC). For solid fuel-fired power plants (Table 14, Appendix A), direct steam generating linear Fresnel solar field is the predominant technology. COMBO-CFB studied hybrid CSP concepts integrating solar field to solid fuel-fired power plants. Direct hybridisation concepts are presented more closely in Chapter 2.2.1 and indirect hybridisation concepts in Chapter 2.2.2.

2.2.1 Direct hybridisation of concentrated solar power and solid fuel-fired power plants

In direct hybridisation of CSP and solid fuel-fired power plant, a solar field generates steam directly to the joint steam cycle without additional heat exchanger between the solar field and the power block. The two subsystems share components, such as turbine, condenser and feedwater preheaters, and the solar share is typically below 10% of the installed power plant capacity (Table 14, Appendix A). Thus, the solar field cannot be operated without the solid fuel-fired power plant, but the solid fuel-fired power plant can be operated without the solar field. (Peterseim et al. 2014a) In direct hybridisation, the system does not include a

thermal storage for solar energy, as an efficient and cost-effective large-scale thermal storage technology for direct steam generating (DSG) solar fields is currently under development (Hirsch et al. 2014). The possible process configurations for direct hybridisation include at least:

1. Feedwater preheating, in which feedwater heated in the solar field is fed to the feedwater line (Figure 17);
2. Feedwater preheating, in which superheated steam from the solar field is fed to the bled off steam line (Figure 17);
3. Cold reheat line, in which superheated steam from the solar field is fed to the cold reheat line after HP turbine (Figure 18);
4. High pressure turbine, in which superheated steam from the solar field is fed to the inlet of high pressure (HP) turbine (Figure 19);
5. Intermediate pressure turbine, in which superheated steam from the solar field is fed to the inlet of intermediate pressure (IP) turbine (Figure 20);
6. Steam drum, in which saturated steam from the solar field is fed to the steam drum of the steam boiler (Figure 21).

The configuration (2) is applied at Liddell Power Station, in which a 9.3 MW_{th} LFC solar field was retrofitted to an existing 2,000 MW_e coal-fired unit to produce steam at 270 °C and 55 bar for feedwater preheating and to replace part of the coal consumption (AREVA Solar 2010; Novatec Solar 2016). The configuration (3) was selected at Kogan Creek Power Station, in which a 44 MW_e LFC solar field was planned to be retrofitted to an existing 750 MW_e coal-fired unit to produce superheated steam at 370 °C and 60 bar into cold reheat line and increase the power output and fuel efficiency of the existing unit (AREVA Solar 2011a). In the Sundt Solar Boost Project, a 5 MW_e LFC solar field with DSG was integrated into an existing 156 MW_e coal and natural gas fired unit. The power output of Unit 4 was increased by 5 MW_e while the same amount of fuel is combusted, but the process arrangement remains unclear (AREVA Solar 2012; Peterseim et al. 2013).

Based on literature, feedwater preheating, called also as solar aided power generation (SAPG), is the most researched option for integrating a solar field with DSG to a steam power plant. In both feedwater preheating configurations (1)−(2) (Figure 17), the solar field is operated parallel with the feedwater preheaters (FWHs) replacing bled off steam from the turbines, which is normally used for feedwater preheating (Hu et al. 2010). The configurations (1)−(2) are suitable for low-temperature applications of PTCs and LFCs (Hu et al. 2010; Peterseim et al. 2013).

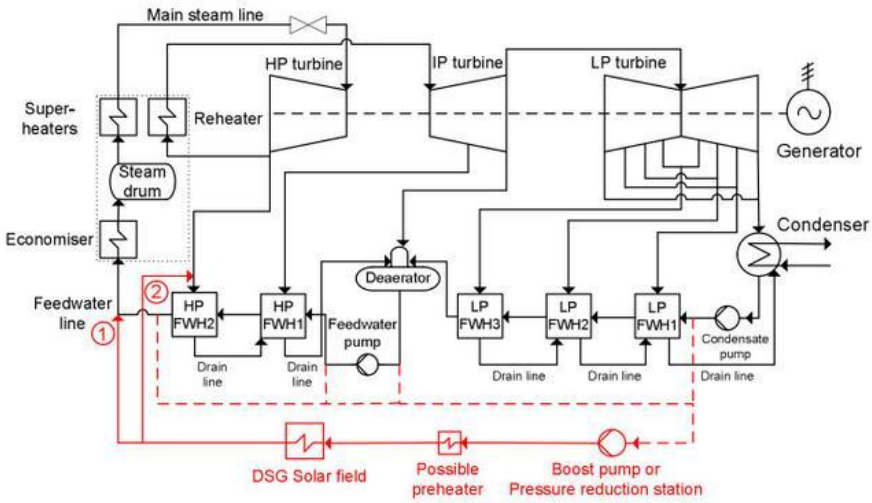

Figure 17. Feedwater preheating configurations, which feed solar steam 1) to feedwater line and 2) to bled off steam line.

The benefit of the feedwater preheating configuration is the possibility for multi-point and multi-level integration. The solar field can replace all FWHs or just a single FWH, and the replacement of FWHs can be done partially or fully (Suresh et al. 2010; Yan et al. 2010). Hu et al. (2010), Petrov et al. (2012) and Suresh et al. (2010) conclude that solar contribution is relevant in both high-temperature and low-temperature applications, but the profit is much greater in the case of substituting HP FWHs compared to substituting low pressure (LP) FWHs. Substitution of the highest pressure FWH alone results in 5−6% additional power generation or fuel saving, whereas the number is less than 1% in the substitution of a single LP FWH (Suresh et al. 2010). The substitution of all FWHs leads to 14−19% fuel saving when operating on fuel saving mode. Other benefits of SAPG are its simple integration and operational flexibility with the steam boiler without incurring substantial costs. (Hu et al. 2010; Lovegrove et al. 2012) Thus, feedwater preheating is a realistic integration approach especially in retrofits, since the changes in the existing steam cycle can be considered as little invasive as possible.

In the cold reheat line configuration (3), superheated solar steam is injected to the steam line after the HP turbine and through the reheaters (Figure 18). Thus, it increases the steam mass flow through the reheating and affects the thermal balance of the heat surfaces and different turbine sections (Yang et al. 2008). The advantage is that the reheaters can assure the quality of the steam if the steam boiler is operated on adequate load. The configuration can be seen as a short-term goal for hybrids, as the steam parameters of approximately 40 bar and 340 °C can be already achieved with all CSP and DSG technologies. Central receiver technology can realise the steam parameters, but the technology is designed for high-temperature applications (Peterseim et al. 2013).

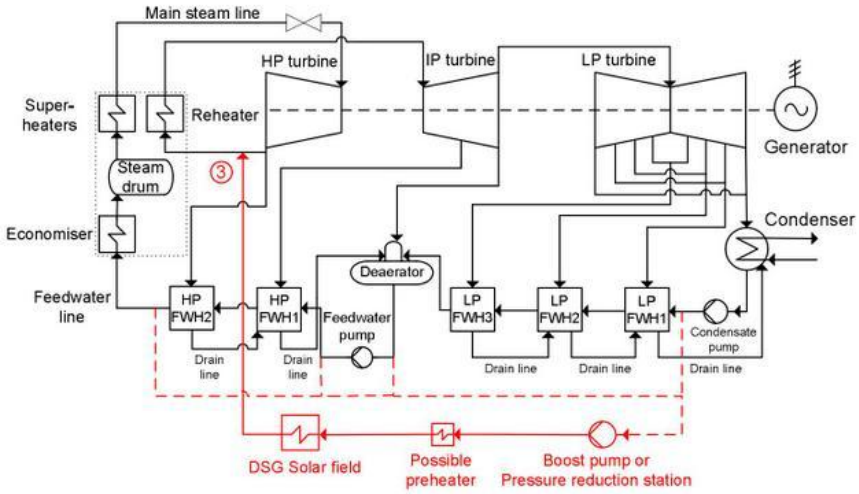

Figure 18. Cold reheat line configuration.

In the HP turbine configuration (4), the solar field produces steam at live steam parameters of the steam boiler (Figure 19). For central receiver with DSG, the configuration is applicable (Peterseim et al. 2013). For line-focusing solar fields, the live steam temperature up to 550 °C is achievable (Alguacil et al. 2014), but the high pressure sets challenges to the collector durability especially in the joints between the collectors in parabolic trough solar field (Fernández-García et al. 2010). The high-temperature collectors are more expensive than low-temperature collectors due to the need for vacuumed receiver tubes (Morin et al. 2012 a). In addition, the high-temperature collectors have lower efficiency with respect to low-temperature collectors due to increased thermal losses (Schenk et al. 2012). On the other hand, the power cycle efficiency is higher in high-temperature applications with respect to low-temperature applications. The HP turbine configuration can be considered as a long-term goal for CSP hybrids and it promotes the development of affordable stand-alone CSP plants. However, the configuration might be technically challenging due to rapid load changes (Lovegrove et al. 2012).

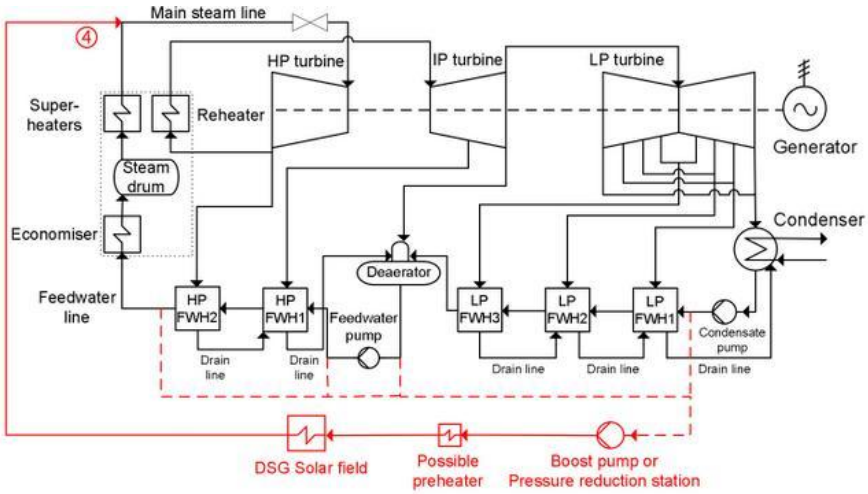

Figure 19. High pressure turbine configuration.

In the intermediate pressure turbine configuration (5), solar steam bypasses entirely the steam boiler and produces steam approximately at 40 bar and 540 °C to the inlet of the IP turbine (Figure 20). Thus, it assists to preserve the thermal balance of the heat surfaces compared to cold reheat line configuration (3), but the HP and other turbine sections are still imbalanced. The configuration can be considered as a medium-term goal, as the steam parameters are already achievable with any CSP technology with DSG. However, the configuration might be a little challenging, as the solar field has to superheat the steam almost 290 °C.

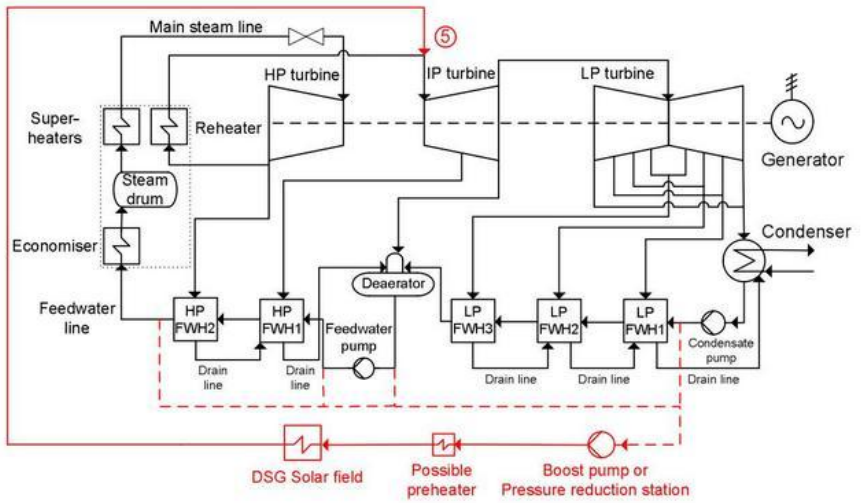

Figure 20. Intermediate pressure turbine configuration.

In the steam drum configuration (6), the solar field is operated parallel with the economiser and evaporator of the steam boiler (Figure 21). The solar field does not include superheating part, as it produces saturated steam or a mixture of steam and water to the steam drum of the boiler. The steam temperature of the solar field is kept at saturation point during unsteady irradiation conditions (Yinghong et al. 2007). The advantage of the configuration is that the superheaters of the steam boiler can assure the quality of live steam if the boiler is operated with adequate load.

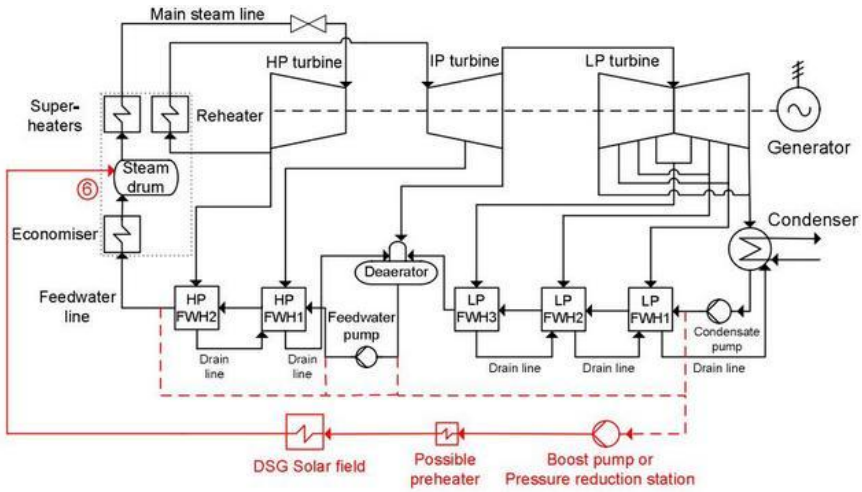

Figure 21. Steam drum configuration.

In addition to several possible process configurations, there are also several possible extraction points for the feedwater to the solar field. Four typical points are 1) after the condensate pump, 2) after the deaerator, 3) after the feedwater pump, and 4) before the economiser. Larger solar share is achieved if feedwater is extracted at lower temperature and feedwater preheating is conducted in the solar field instead of the feedwater preheaters. If the feedwater is extracted after the condensate pump, an additional boost pump is needed before the solar field, because the pressure losses occurring along the solar field must be compensated and the required pressure stage of the integration point needs to be met. If the feedwater is extracted after the feedwater pump, a pressure reduction station might be needed before the solar field, since the water pressure may not be suitable for the solar field. (Yang et al. 2008) To avoid the Ledinegg instability in the solar field, an additional preheater might be needed before the solar field.

2.2.2 Indirect hybridisation of concentrated solar power and solid fuel-fired power plants

In indirect hybridisation, the possible process configurations are similar to the direct hybridisation. Compared to direct hybridisation, an additional heat exchanger is installed between the solar field and the power block (Figure 22). Thermal energy storage system can be integrated to the solar field. If the HTF applied in the solar field is thermal oil, the process configurations (1)−(3) and (6) are applicable, as the thermal oil starts to degrade at temperatures over 400 °C. For molten salt solar fields, the configurations (4)−(5) requiring higher temperature levels are also applicable, since molten salts are suitable for high-temperature applications over 400 °C. (Peterseim et al. 2013)

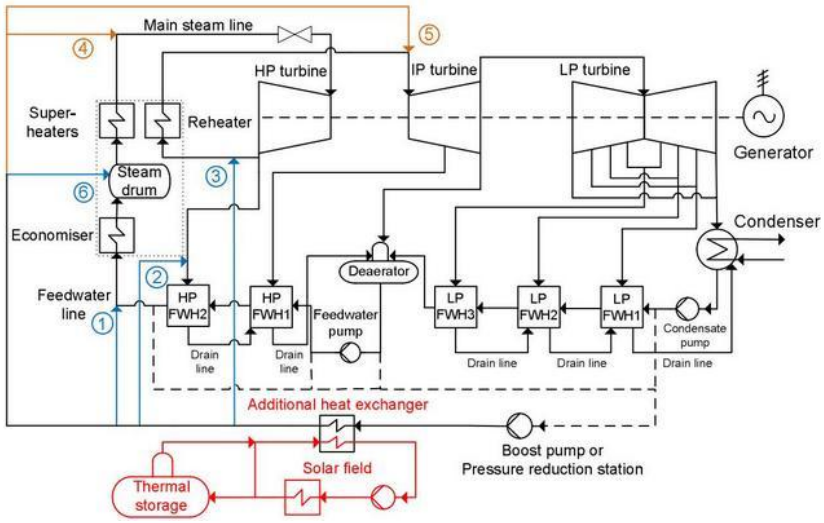

Figure 22. Process configurations for indirect hybridisation of solar field and solid fuel-fired power plant.

The only operational indirect CSP and solid fuel-fired hybrid plant of relevant size so far is the 22.5 MW_e Termosolar Borges, which applies PTCs with thermal oil, two biomass boilers (2 x 22 MW_{th}) and a small auxiliary boiler (Figure 23). The aim of the configuration is to achieve high renewable electricity output and major stability of the system. (Cot et al. 2010) The plant is considered as a strong CSP hybrid, in which the solar share is much higher than in the current direct hybridisation concepts (Table 14, Appendix A) (Peterseim et al. 2014a). Since PTC solar field with oil as HTF produces saturated steam at <400 ºC, the steam is superheated to the final steam temperature of 520 ºC with either biomass or natural gas.

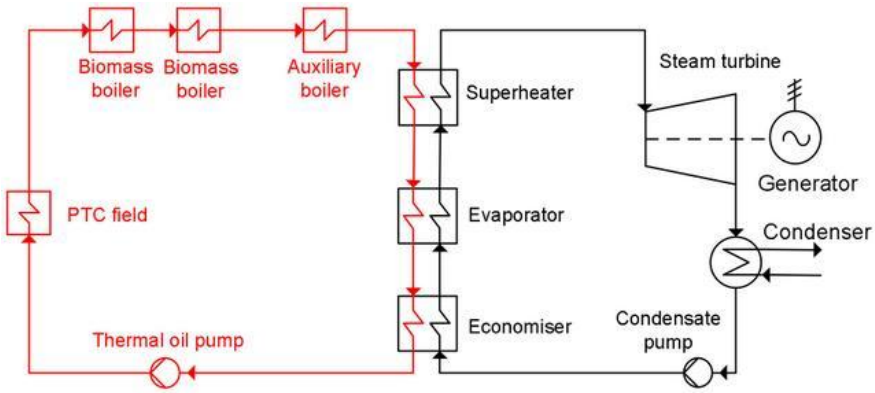

Figure 23. Schematic of the process configuration in Termosolar Borges plant (Cot et al. 2010).

Boilers can combust either biomass (forest residues and agricultural crops) or natural gas depending on the irradiation conditions. Biomass is combusted at night or in completely cloudy days in order to achieve at least 50% load of the turbine. During cloudy periods, natural gas is combusted in order to obtain faster and more accurate control of the system. The auxiliary boiler is installed for assistance during extreme process conditions. As a result, the solution allows expanding the CSP technology to areas with lower irradiation levels (~1,800 kWh/m^2) and enables the use of different kinds of fuels in CSP plants. (Cot et al. 2010)

2.3 Thermochemical processes and applications

Besides direct electricity production, CSP can be applied to various thermochemical processes. In solar thermochemical process, concentrated solar radiation is used as a source of energy (in form of heat) to drive highly endothermic chemical reactions requiring high temperatures (500–2,000 °C). Most of the applications are related to producing fuels and the product of such a process is commonly referred to as a “solar fuel” or “solarised fuel”. (Simakov et al. 2015) The basic principle of solar fuel process is illustrated in Figure 24, which shows solar hydrogen production as an example. Chemicals or material commodities such as lime or metals can be produced via similar processes.

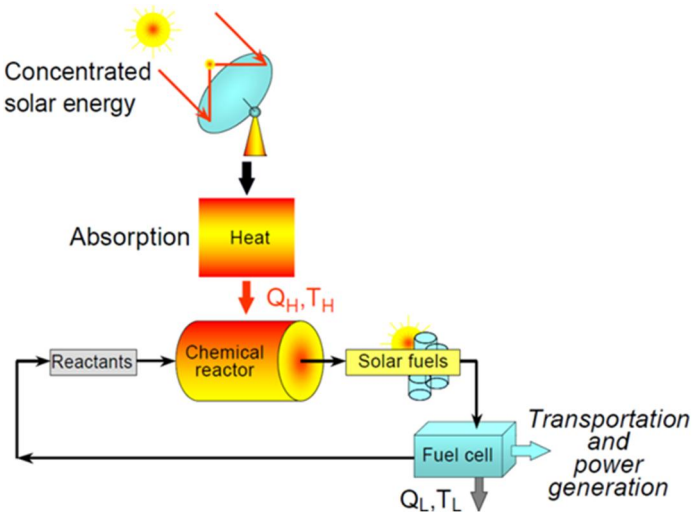

Figure 24. The basic principle of thermochemical solar fuel process (Steinfeld et al. 2004).

In traditional thermochemical processes, the needed heat to drive the reactions is typically supplied either by burning part of the reactants or some fossil fuel, such as natural gas. By utilising concentrated solar radiation instead, emissions can be lowered and more end-products can be obtained from the same amount of starting material. In some cases, there are also additional benefits, such as better end product purity. Furthermore, as solar fuels can be stored long term and transported long range, they could be produced in the sunny and desert regions and transported to the industrialised and populated centres, where majority of the energy is needed.

The main thermochemical pathways of solar fuels are reforming and cracking of gaseous hydrocarbons, thermochemical splitting of water or CO_2 and gasification of solid fuels (coal, biomass) (Figure 25) (Agrafiotis et al. 2014). The end product is hydrogen gas or syngas, which can be used as chemical feedstock or as a fuel for gas turbines.

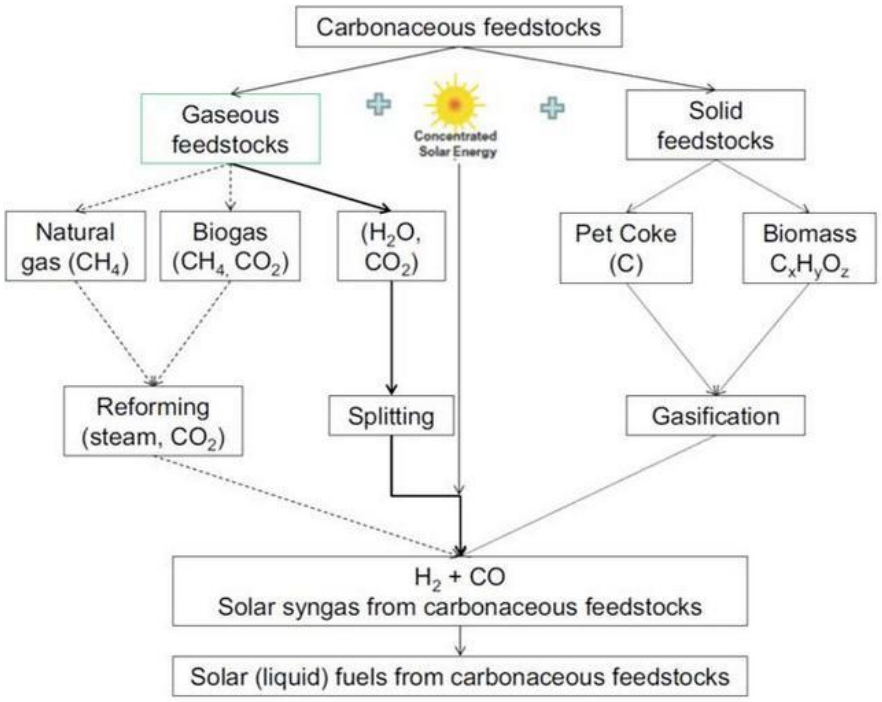

Figure 25. Various thermochemical pathways of solar fuels (Agrafiotis et al. 2014).

In thermochemical applications of CSP technology, the plain receiver is often replaced with a combined receiver-reactor, in which the chemical reactions occur. The available CSP technologies are central receivers and parabolic dishes in high-temperature applications (>600 °C) and parabolic trough collectors in low-temperature applications (<600 °C). (Simakov et al 2015) For commercial scale high-temperature applications, the beam-down CR with compound parabolic concentrator (CPC) (Figure 26) is especially suitable, since the receiver-reactor can be placed on ground and the CPC enhances the concentration of solar energy (Kodama et al. 2007). Figure 27 shows indicative temperature ranges requires in different solar fuel processes.

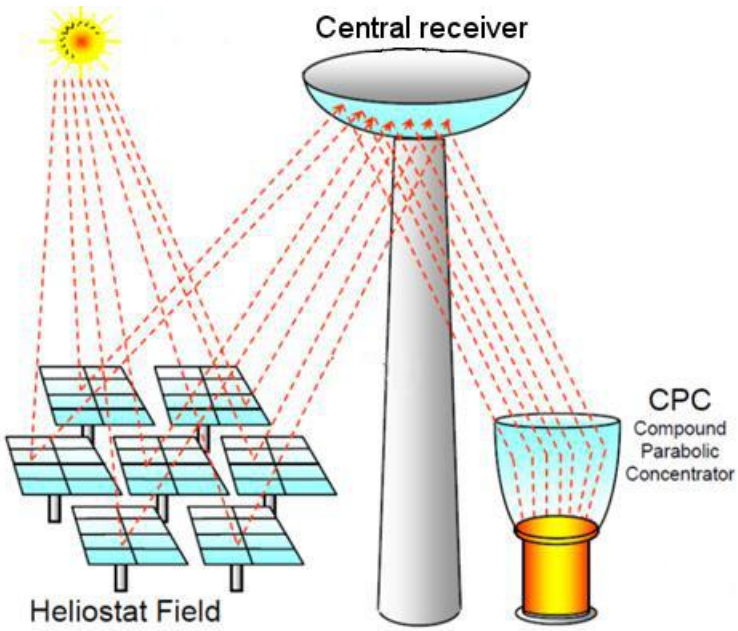

Figure 26. The beam-down variant of central receiver equipped with compound parabolic concentrator (CPC) for achieving higher tempertures (Courtesy of Weizmann Institute of Science).

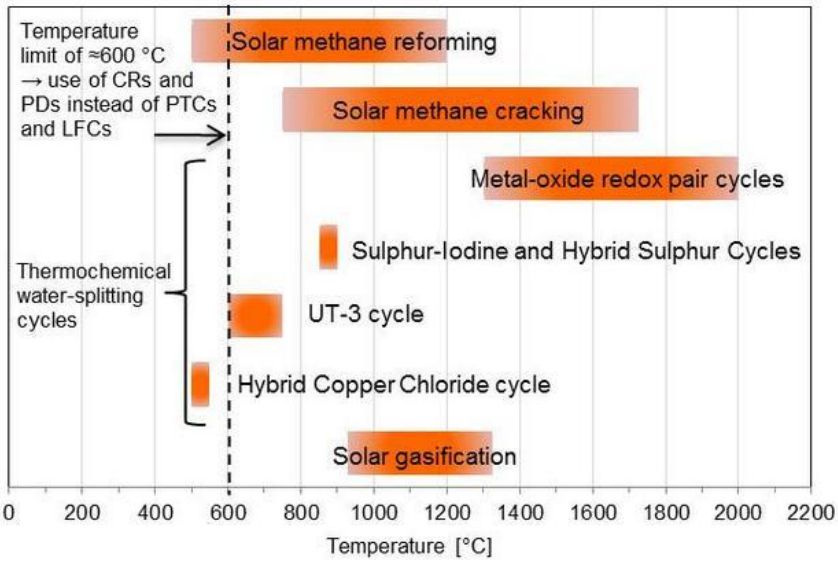

Figure 27. Indicative temperature ranges of the solar fuel processes.

The measure of how efficiently the solar energy input is converted into the chemical energy of the end products is the solar-to-fuel energy conversion efficiency, which can be defined as:

$$\eta_{solar-to-fuel} = \frac{m_{products} \times LHV_{products}}{Q_{solar} + m_{feedstock} \times LHV_{feedstock}} \quad (1)$$

where Q_{solar} is the total solar energy delivered through the receiver's aperture over the duration of the experimental run, m is the mass (integrated over the duration of the production run), and LHV is the lower heating value. The energetic upgrade factor (U) is defined as the ratio of the energy content of the products and feedstock on LHV basis:

$$U = \frac{m_{products} \times LHV_{products}}{m_{feedstock} \times LHV_{feedstock}} \quad (2)$$

If the U is higher than 1, the products contain more energy compared to the feedstock. And if the process was carried out using solar energy, the extra energy of the products is solar-based energy.

2.3.1 Solar thermal reforming of methane

Reforming is a process where hydrocarbon fuels (most commonly methane) is converted into hydrogen and carbon monoxide (i.e. syngas). The typical temperature levels of industrial applications are in the range of 800–1,000 °C due to high conversion rate of methane (Simakov et al. 2015). The possible solar thermal reforming techniques for methane are steam methane reforming (SMR) and dry methane reforming (DMR). In SMR, the reactant gases are methane and steam (Eq. 3), whereas the steam is replaced with CO_2 in DMR (Eq. 4). The SMR is more promising than DMR, as CO_2 streams are not readily available. In SMR and DMR, the energetic upgrade factor U of the end products are respectively 1.26 and 1.31 with stoichiometric reaction compared to LHV of methane (50 MJ/kg, 802.1 kJ/mol). (Simakov et al. 2015)

$$CH_4 + H_2O(g) \leftrightarrow 3\,H_2 + CO, \Delta H^0_{298\,K} = +206\ kJ/mol \quad (3)$$

$$CH_4 + CO_2(g) \leftrightarrow 3\,H_2 + CO, \Delta H^0_{298\,K} = +247\ kJ/mol \quad (4)$$

The advantage of the solar thermal reforming of methane is the similarity with conventional reformers, as the only difference is the heat source. In addition, the receiver-reactor can be operated on hybrid mode, in which the natural gas can be used as a heat source at times when solar irradiation is not sufficient. (Simakov et al. 2015) The solar thermal reforming of methane is confirmed to be technically feasible during steady-state and transient irradiation conditions (Böhmer et al.

1991), but the disadvantages are high capital costs due to expensive materials and catalyst. The costs could be lowered with low-temperature SMR (<600 °C), which enables the use of cheaper materials and simpler design. However, low-temperature regime requires the development of H_2 separation membranes in order to enhance the conversion process. In addition, the catalytic materials have to be developed, as the materials have to be very active, stable to oxidation and resistant to coking. Despite the clear potential in solar reforming, its practical implementation is still very challenging. As a result, widespread commercialisation of solar reforming has not been realised, although important proof-of-concept facilities are already operational. (Simakov et al. 2015)

2.3.2 Solar thermal cracking of methane

In thermal cracking of methane, natural gas (or other hydrocarbon) is decomposed into H_2-rich gas and solid carbon (Eq. 5). The typical temperature level is in the range of 1,327−1,727 °C (Ibrik et al. 2012), but the temperature level can be lowered to the range of 750−1,000 °C with reactor design (Paxman et al. 2014). With theoretical energy balance calculation, the U value of 1.09 could be reached.

$$CH_4 \xrightarrow{\text{heat}} 2\,H_2 + C(s),\ \Delta H^0_{298\,K} = +75\ \text{kJ/mol} \qquad (5)$$

The advantages of methane cracking are CO_2 free hydrogen production and the utilisation possibilities of the solid carbon, which is a marketable nanomaterial called “carbon black”. The quality of the carbon black determines the possible end-use applications, which include using carbon black as reinforcing filler in tires and other rubber products and as a pigment in plastics, paints and inks. In addition, thermal cracking accomplishes the removal and separation of carbon in a single step, whereas methane reforming requires additional steps to shift CO and remove CO_2. Furthermore, handling and storing of solid carbon is easier compared to gaseous CO_2. (Meier et al. 2012) A disadvantage of methane cracking is its expensive operative costs due to regeneration of the catalyst with steam gasification or air oxidation. In addition, the profitability of the process is dependent on the market value of the solid carbon. Thus, methane cracking is not applied in industrial scale, as it is not cost competitive with other hydrogen production processes. (Amin et al. 2011) However, several experimental reactors have been developed and tested (Rodat et al. 2010; Maag et al. 2009; Paxman et al. 2014).

2.3.3 Solar gasification

In gasification, solid carbonaceous feedstocks are converted into gaseous end products with sub-stoichiometric amount of steam and/or oxygen. Gasification is an endothermic reaction (Eq. 6), which typically requires combustion of part of the feedstock. In solar gasification, the energy is provided in the form of concentrated solar heat. The temperature level of gasification is in the range of 700–1,400 °C,

and it depends on the feedstock and the gasification technology. Solar gasification has been tested in the temperature range of 927–1,327 °C (Kodama et al. 2002; Piatkowski et al. 2011). With gasification, the U value of 1.35–1.5 can be reached (Piatkowski et al. 2011; Trommer et al. 2005). In addition, solar-to-chemical efficiency in the range of 17–29% has been achieved in experimental investigations (Piatkowski et al. 2009).

$$CH_xO_y(s) + (1-y)H_2O \rightarrow (1+\frac{x}{2}-y)\,H_2 + CO \quad (6)$$

The advantages of solar-driven gasification include high syngas output per unit of feedstock, avoiding contamination of syngas with combustion by-products, higher obtainable temperatures (>1,100 °C) and there is no need for an upstream air separation unit, as the only gasifying agent is steam (Wieckert et al. 2013). The disadvantage of gasification is the need of steam, as solar-rich areas are typically low in water resources. In addition, intermittent solar irradiation conditions can result in short term peaks in syngas production, which require extra capacity of the handling equipment of the end products. (Piatkowski et al. 2011)

The development of solar gasifiers is still at an early stage even though some pilot-scale gasifiers has been tested (Puig-Arvanat et al. 2013). The challenges of solar gasifiers involve scaling up the technology, design of the receiver for the efficient absorption of irradiation and operation of the solar reactor and peripheral components under transient conditions (Wieckert et al. 2013).

2.3.4 Thermochemical splitting of water and carbon dioxide

The basic idea of thermochemical water (or CO_2) splitting cycles is to use heat to produce H_2 and O_2 (or CO and O_2). The rationale behind the thermochemical water-splitting cycles is that they can – in theory – produce hydrogen with better efficiency compared to solar powered water electrolysis. The thermochemical water splitting cycles include multiple reaction steps, which result in the same overall reaction than single-step thermal dissociation of water to hydrogen and oxygen (Table 2). The cycles allow lower operation temperature (in the range of 500–2,000 °C) than the single step dissociation (above 2,227 °C) while simultaneously avoiding the problems of recombination of H_2 and O_2 (back to H_2O) and formation of explosive mixtures. The cycles include Sulphur-Iodine cycle, Hybrid Sulphur cycle, UT-3 cycle, Hybrid Copper-Chlorine cycle and various metal oxide redox pairs. The metal oxide redox pairs are at particular interest of CSP applications, as the processes are relative simple in theory compared to other cycles, and CSP is capable of generating very high temperatures. (Agrafiotis et al. 2015) The other cycles involve numerous of challenges including use of expensive and corrosive reactants, complex reactor design and durability of materials (Perret 2011).

Table 2. Thermochemical splitting cycles (Da Costa Coelho 2014; Agrafiotis et al. 2015)

Cycle	Reaction steps	Temperature [°C]
Sulphur-Iodine Cycle	$H_2SO_4 \rightarrow H_2SO_4 + H_2O$	875
	$H_2SO_4 \rightarrow H_2O + SO_2 + \frac{1}{2}O_2$	875–1,275
	$2H_2O + I_2 + SO_2 \rightarrow H_2SO_4 + 2HI$ (Bunsen reaction)	100
	$2HI \rightarrow I_2 + H_2$	300–500
Hybrid Sulphur Cycle	$H_2SO_4 \rightarrow H_2SO_4 + H_2O$	875
	$H_2SO_4 \rightarrow H_2O + SO_2 + \frac{1}{2}O_2$	875-1275
	$H_2O + SO_2 \rightarrow H_2SO_4 + H_2$ (electrolysis)	80
UT-3 cycle	$CaBr_2 + H_2O \rightarrow CaO + 2HBr$	700–760
	$CaO + Br_2 \rightarrow CaBr_2 + \frac{1}{2}O_2$	500–600
	$Fe_3O_4 + 8HBr \rightarrow 3FeBr_2 + Br_2 + 4H_2O$	200–300
	$3FeBr_2 + 4H_2O \rightarrow Fe_3O_4 + 8HBr_2 + H_2$	550–650
Hybrid Copper-Chlorine cycle	$2CU_2 + 2HCl \rightarrow 2CuCl + H_2$	425
	$4CuCl \rightarrow 2Cu + 2CuCl_2$ (electrochemical)	25 (ambient)
	$2CuCl_2 + H_2O \rightarrow Cu_2OCl_2 + 2HCl$	325
	$Cu_2OCl_2 \rightarrow 2CuCl + \frac{1}{2}O_2$	550
Metal oxide redox pair (for water)	$M_xO_y \xrightarrow{heat} xM + \frac{y}{2}O_2$	1,227–2,027
	$Mx + y\,H_2O\,(g) \rightarrow M_xO_y + y\,H_2\,(g) + heat$	127–427
	where M = metal (Fe,Co,Ni etc.)	
Metal oxide redox pair (for CO_2)	$M_xO_y \xrightarrow{heat} xM + \frac{y}{2}O_2$	1,227–2,027
	$Mx + y\,CO_2\,(g) \rightarrow M_xO_y + y\,CO\,(g) + heat$	127–427
	where M = metal (Fe,Co,Ni etc.)	

In metal oxide redox pair cycles, the overall reaction is divided into two steps (Figure 28). The first step is thermal reduction of metal oxide to elemental metal (or to a lower valence state) in a highly endothermic reaction at very high temperature (1,200–2,000 °C). The reduction reaction is followed by an exothermic hydrolysis reaction, in which water or CO_2 reacts with reduced metal to form hydrogen or CO and metal oxide. Syngas can be generated by combining both H_2O and CO_2 splitting cycles (Agrafiotis et al. 2015)

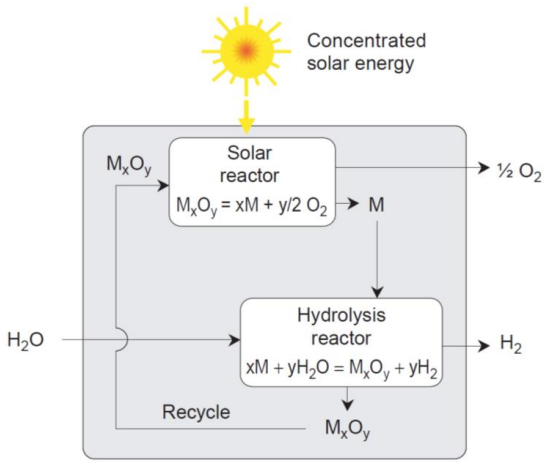

Figure 28. An illustration of a generic two-step water splitting thermochemical cycle based on metal oxide redox reactions (Steinfeld et al. 2004).

The cycles can be classified to volatile and non-volatile cycles according to the phase of metal compounds during the entire process. In volatile cycles, the metal compound is vaporised in the first step. As a result, the products of the first step need to be either cooled down rapidly or separated electrolytically in order to prevent their recombination. The cooling introduces irreversibility and poses severe design challenges for commercial scale systems. (Steinfeld et al. 2004) In non-volatile cycles, the metal compound stays in solid phase avoiding the issue with recombination. The important characteristics of non-volatile metal oxide are its physicochemical characteristics such as specific surface area, particle size, intra-particle porosity etc.

According to Steinfeld et al. 2014, the most potent candidate metal oxide redox pairs are ZnO/Zn (volatile) and Fe_3O_4/FeO (non-volatile). The solar-to-chemical efficiencies of ZnO/Zn and Fe_3O_4/FeO are 39% and 29%, respectively (Gálvez et al. 2008). Even though some of the metal oxide redox pair cycles have been already successfully demonstrated at bench-scale and pilot-scale, crucial technical challenges have still not been solved and there is a notable way to go for potential commercial exploitation. The 'non-volatile' metal oxide redox pairs, in which the metals remain in solid state for the whole cycle, seem to be more promising for commercial applications. (Agrafiotis et al. 2015) One inherent challenge related to all metal oxide redox systems is the need for very high temperatures, which basically means that reduction step can be driven only when solar irradiation is adequately available and thus, it must be able to handle intermittent operation.

2.3.5 Economics of the thermochemical applications

Da Costa Coelho (2014) compared the economics of the thermochemical applications (Table 3) assuming hydrogen is the desired product. The prices should be considered as indicative, as the majority of the technologies are still in project/prototype scale and it is difficult to obtain comparable results.

Table 3. Hydrogen production costs and efficiencies per cycle (Da Costa Coelho 2014).

Cycle	Production costs (€/kg)	Operating temperature of cycle (ºC)	Cycle efficiencies (%)	Efficiencies solar to hydrogen (%)
Metal oxide cycles	3.5 – 13 [a]	1400 - 2300	45-60 [b]	17-22 [b]
Westinghouse cycle	3.9 - 5.6 [a]	875 – 1275	51 [c]	22 [c]
General Atomics process	2.4 - 7.9 [d]	875 – 1275	45 [c]	19 [c]
UT -3 cycle	3.9 – 4.2 [e]	700 – 760	47 [e]	8 [e]
Hybrid Copper chloride	4.0 - 5.5 [f]	550	49 [g]	23 [g]
Water electrolysis with CSP electricity	2.1 - 6.8 [a]	-	30 [g]	14 [g]
High temperature solar steam electrolysis [a]	5.5 – 6.7 [d]	750 – 950	45 [g]	20 [g]
Solar methane cracking	3.0 - 3.9 [h]	1600 – 1900	70 [h]	9.1-31 [i]
Solar steam reforming of methane	1.8 - 1.9 [j]	900	86 [j]	63 [j]
Solar petroleum coke gasification	-	1600 - 2100	48 - 87 [k]	9-20 [k]
Commercial coal gasification (with / without carbon sequestration)	0.8 / 0.64 [l]	600 – 1000	63 [m]	-
Commercial natural gas steam reforming (with / without carbon sequestration)	0.66 / 0.53 [l]	900	83 [m]	-
Biomass gasification	0.85 - 1.7 [l]	1100	40 – 50 [m]	-
Photo-catalytic water splitting	3.5 [l]	-	10 -14 [m]	-

[a] adjusted prices based on a 50 MWth CSP plant [14].

[b] based on a 46 MWth CPC Si-G reactor receiver on a CRS [13].

[c] based on a solid particle 700 MWth receiver [13].

[d] adjusted prices based on current process designs and small scale pilot plants [15].

[e] based on a CRS-CSP with day and night operation for a projected output of 20000 Nm^3/h [36].

[f] hybrid copper chloride cycle coppled with a desalinization plant using nuclear adjusting the capital costs to solar energy [37].

[g] based on a molten salt 700 MWth receiver on a CRS-CSP plant configuration [13].

[h] CRS-CSP with a heliostat field from 2188-8750 m^2 with elemental carbon production based on [50].

[i] based on a 5 kW particle flow reactor in a solar furnace [26].

[j] based on the SOLASYS reformer with 50 MWth [21].

[k] based on based on a 5 kW reactor in a solar furnace [19, 20].

[l] based on [51] and considering a cost increase of 25% for the provision and implementation of the carbon capture costs [14].

[m] process energy efficiency - energy value of produced hydrogen divided by the energy input - based on [51].

As a result, the solar (assisted) processes are not yet competitive with current fossil fuel or biomass based processes. Solar steam reforming of methane was estimated to have the lowest production cost of the solar assisted technologies, and it could thus be the first step of the integration of CSP in hydrogen production. This would offer partial decarbonisation and could be the technological bridge form current technologies to completely renewable hydrogen production from water. The analysis did not unfortunately include H_2 production cost via solar gasification, which could also be interesting first step solution. However, it seems that there are more technical challenges in solar gasification compared to methane reforming where only gas phase reactants and products exist. On the other hand, gasification can be carried out without catalysts.

3. Effects of CSP integration on CFB combustion dynamics

The challenges of large-scale power plants include demanding performance requirements defined by the customer or by the electric grid operator. In addition, the emission regulations for large-scale power plants are continuously tightened. As a result, new operational requirements are set for the boilers:

1. The operational range of large-scale power plants should be increased by degreasing the minimum achievable load level;
2. The boiler should be capable of fast and frequent load changes in a wide load range;
3. The emission limits have to be met during steady-state operation as well as during fast load changes.

One of the state-of-the-art boiler technologies is circulating fluidized bed (CFB) boiler (Chapter 3.1). It is expected that through research (Chapter 3.2), the minimum load of CFB boilers can be decreased from 30% of maximum continuous rating (MCR) to 15 − 20% of MCR, and maximum load change rate can be increased from 5% of MCR/30s up to 10% of MCR/30s. (Kettunen et al. 2014)

3.1 Circulating fluidized bed boilers

CFB boilers are typically utilized in large-scale applications (100 MW_e–800 MW_e). Thus, the CFB boilers are typically larger than stokers but smaller than pulverised coal combustion (PCC) boilers. The established benefits of CFB boilers include high efficiency and availability, broad fuel flexibility, low emission levels and low installation costs (Chapter 3.1.1). The process requirements and restrictions of the steam boiler and other components (Chapter 3.1.2) need to be taken into account, as the solar integration affects the operation conditions of the shared components in the joint steam cycle.

In a CFB boiler, fuel is fed to a furnace, which contains limestone and inert bed material, such as sand or ash (Figure 29). The fuel, limestone and bed material are kept in a suspension due to stream of combustion air, which is distributed throughout the furnace floor. The average bed particle diameter is 0.1−0.3 mm

and the fluidizing velocity of CFB boiler is 4.5 m/s−7 m/s, which is over the entrainment velocity of particles (Rayaprolu 2009). Thus, the solids are carried out from the furnace and circulated back by a cyclone. The solids circulation loop is called as a hotloop. The separated flue gas enters the flue gas duct, which contains superheater, reheater, economiser and input gas preheaters in order to superheat the generated steam, preheat the feedwater entering the boiler and preheat the combustion air entering the furnace. Particles are removed from the flue gas by an electrostatic precipitator before the flue gas enters the stack.

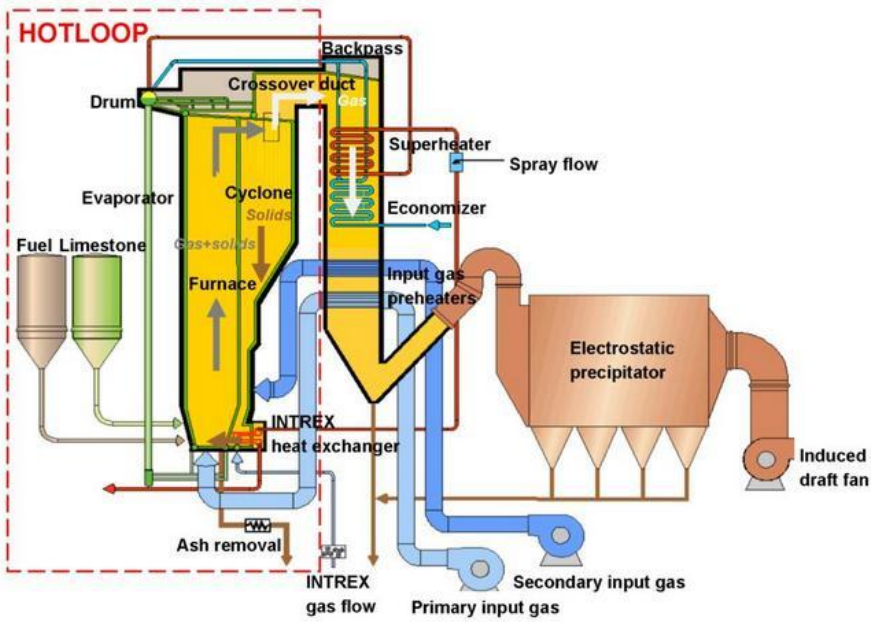

Figure 29. Schematic of the CFB boiler and its operations. The hotloop is highlighted with the dashed line (Kovács et al. 2015).

3.1.1 Benefits of CFB boilers

CFB boilers enhance the use of different kinds of low-quality fuels, such as by-products of the forest industry, other residue biomasses and wastes. The bed material acts as disperser for the fuel, and stores a large amount of thermal energy, which ignites the fuel quickly. Due to effective mixing and turbulence of the bed, heat transfer is enhanced, and the generation of heat inside the bed material is lower and more evenly distributed than in PCC boilers. In addition, the bed material provides adequate retention time to complete the combustion process. (Rayaprolu 2009)

The low emission levels are due to in situ control of SO_2 emissions, lower combustion temperature and staging of combustion air (Teir 2002). The in situ

control of SO_2 emissions is conducted by desulfurisation during combustion process, which eliminates the need for separate and expensive flue gas desulfurisation facilities. The bed material always contains excess amount of limestone, which acts as a sorbent for SO_2. The lower combustion temperature and staging of combustion air lowers the NO_x emissions (Teir 2002). The thermally induced NO_x begins to form, as the combustion temperature in the furnace reaches 1,300 °C. However, in CFB boilers the temperature of the bed material is typically around 780-900 °C, which is well below the temperature range, where thermally induced NO_x production occurs. By staging the combustion air to different air zones in the furnace, the formation of fuel-bound NO_x can be minimized.

3.1.2 Process requirements and restrictions of CFB boiler in CSP hybrid plant

The main process requirements and restrictions of a CFB boiler are the operational limitations for FWHs, turbines, and boiler. For the optimum performance of FWHs, the steam extractions from turbines should be optimized in order to maintain the heating requirements for feedwater preheating (Sharma et al. 2015). In other words, the pressures and mass flow rates of bled off steams should be kept constant. In addition, the turbine inlet conditions are designed to be kept as constant as possible, and flow instabilities should be avoided during spatially and temporally changing irradiation conditions (Eck et al. 2007). For example, if the turbine inlet conditions vary, the mass flow through the turbine and the pressure difference between each stage of the turbine varies (Hong-juan et al. 2013). Furthermore, the extraction of additional steam from one point of turbine affects the following extraction points. If the amount of bled off steam is increased at one point, it decreases the pressure at that stage and vice versa. Consequently, the pressure is lower also in the following points, which corresponds to lower quality of bled off steam to the following FWHs. Thus, the knowledge of the load behaviour is crucial for the optimum design of FWHs.

Most modern boilers and turbines are capable to handle increased loads up to 10% above the nominal continuous load (Petrov et al. 2012). However, running the boiler continuously at its peak load should be avoided, since the lifetime of the boiler is decreased due to continuously higher temperatures in the heat surfaces of the furnace. Thus, the maximum peak load duration is considered to be 4 h per day without significant reduction in boiler's lifetime. If the peak load rating or duration is higher, the boiler should be resized to adapt to the increased peak rating. As a result, the turbine has to be also resized. The optimum operation of the steam power plant should be assured also when solar energy is not available. Therefore, oversizing of the components should be avoided, since oversized components reduce the efficiency of the plant and increase the investment and operational costs. (Rayaprolu 2009)

Steam boiler has to be capable of compensating transients from the solar field under fluctuating solar irradiation conditions. Currently, the requested load change rate of CFB boilers is 2−5% of MCR/30 s, but load change rate up to 10% of

MCR/30s is foreseen to be achievable in the future in coordination with the steam turbine (Kettunen et al. 2014). Heat stress should be kept as minimum as possible in order to promote lifetime of the components. Metal temperatures of the boiler heat transfer surfaces are controlled with spray water, which amount is usually limited to approx. 8% of the total flow in order to reduce the thermal shock on steam pipes and to ensure the full vaporization of water droplets before HP turbine (Rayaprolu 2009).

The absolute live steam temperature to the turbine should not exceed the rated temperature by more than 28 °C, whereas the absolute pressure should not exceed the rated pressure by more than 120%. Rotation speed of the turbine should be kept between 98% and 101% of the rated value. As a rule of thumb, the acceptable steam temperature gradients for turbine are smaller than 5 °C /min, but the allowable steam temperature transient varies between different turbine types and manufacturers. (Birnbaum et al. 2011) The water fraction of the exhaust steam must be kept under 12% in order to avoid condensation inside the turbine (Rayaprolu 2009). Currently, Siemens promotes themselves as the world market leader of CSP plant suitable steam turbines, which have been optimised to handle the intermittent power generation and periodicity of solar irradiation (Siemens 2011).

In order to accommodate the system for higher solar share without oversizing the components, the boiler needs to be run at partial load, while the turbine is operated at its maximum load. Due to the fouling of the heat surfaces and erosion of the boiler components during aging, thermal performance of the boiler is usually designed to be slightly better at lower loads than at the maximum continuous load rate (Popov 2011). The efficiency of the boiler is typically designed to be optimum at normal continuous load rate, which is 90% of the maximum continuous load (Rayaprolu 2009). If the boiler is designed to be operated on partial loads for longer time periods, the part load performance data have to be obtained from the boiler manufacturer, as the part load performance varies among boilers and technologies. For example, the part load performance of bubbling fluidized bed (BFB) boilers is significantly lower with respect to CFB and PCC boilers. (Rayaprolu 2009) In addition, partial load of the boiler affects the performance of heat surfaces. At lower loads, the temperature of the flue gases decreases, and larger heat transfer surfaces are required to maintain live steam and reheated steam temperatures constant. Typically, the load range is 70% to 100% of the MCR, in which the steam temperatures after superheaters and reheaters are required to be held constant. (Rayaprolu 2009) Furthermore, the final temperature of the flue gases should be 140 °C to 150 °C if the flue gases contain sulphur (Raiko et al. 2013). In other words, the final temperature of the flue gases should not be decreased under the dew point of the flue gases.

3.2 Pilot-scale CFB combustion tests

Pilot-scale CFB combustion tests were conducted at VTT's facilities to study combustion dynamics and emission formation during minimum boiler load and maximum load changes, which can lead to e.g. unexpected emission formation, gasification reactions, local hotspots and defluidization of the bed material. The target of the dynamic tests was to characterize combustion dynamics of different fuels and effects of different combustion conditions on the combustion dynamics. Three types of fuels, bituminous coal, anthracite and spruce bark (biomass), were selected for the test series (Figure 30):

1. Stationary 30% load test.
2. ±10% stepwise tests in fuel feeding during low load operation (including 30 min stabilization between tests).
3. Fast load change test (7% of MCR/30s) from 30% to 100% load.
4. Stationary 100% load test.
5. Fast load change test (7% of MCR/30s) from 100% to 30% load.
6. Stabilization and change of fuel type.

The effects of different combustion conditions on the dynamics were sought in the case of bituminous coal with two additional test series similar to the one in Figure 30:

1. Increased bed temperature.
2. Staging 30% of fuel feed into the top of the combustor.

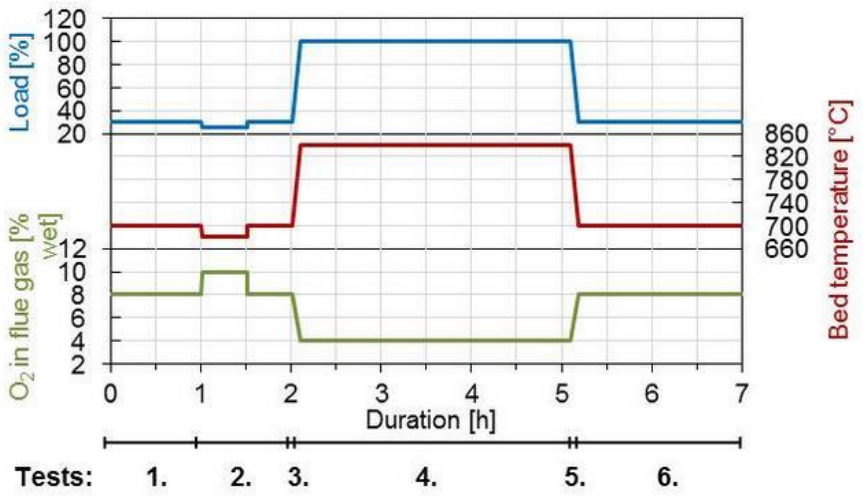

Figure 30. The series of combustion tests carried out for each fuel type and for two additional test series for bituminous coal.

In the ±10% stepwise and fast load change (7% of MCR/30s) tests, fuel reactivity differences between fuel types were observed. Changes in flue gas oxygen level and bed temperature revealed to be slower with anthracite (lower volatiles content) than with bituminous coal and bark. The flue gas O_2 stabilization times were approx. 5 min for bark, 10−20 min for bituminous coal and 15−20 min for anthracite, respectively (Figure 31).

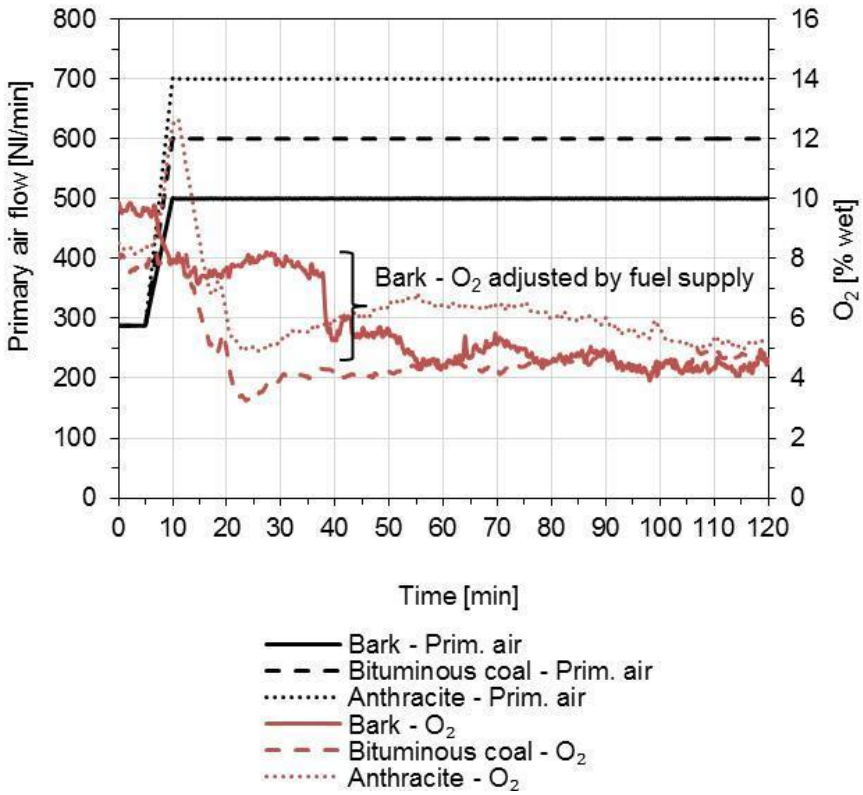

Figure 31. The flue gas O_2 stabilization for selected fuels during 7% of MCR/30s load increase.

The stabilization times for circulation and bed material temperatures were rather long (>90 min) for all the fuel types (Figure 32). The long times were due to heating or cooling of the solids in the circulation loop, which is related to the small-scale test rig and its dimensions. In the bed area, the changes in heat transfer followed the changes in the bed temperature. In the freeboard area, the changes in heat transfer followed the changes in the suspension density.

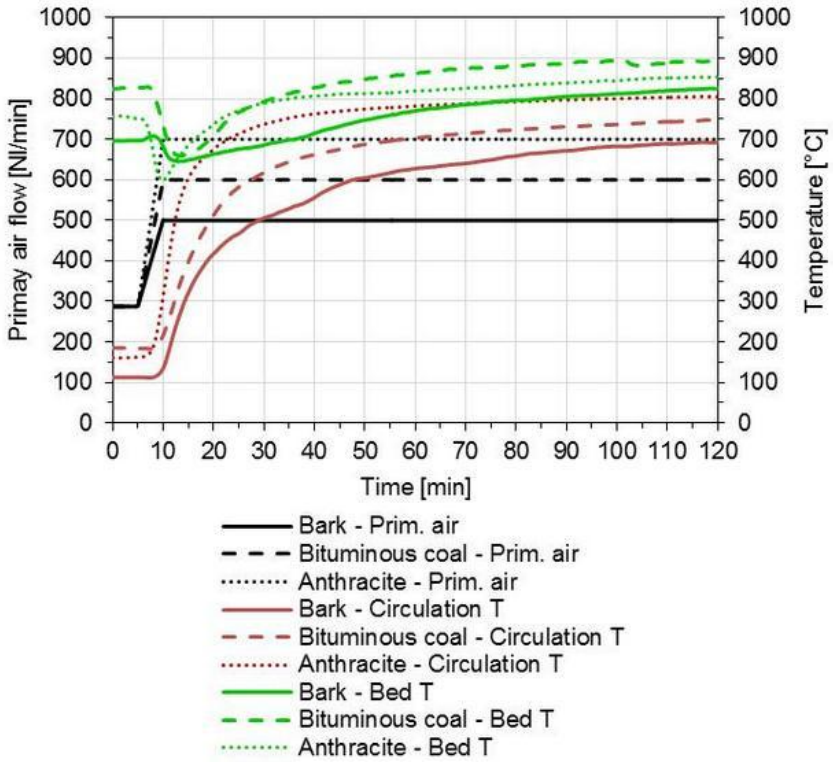

Figure 32. Bed and circulation material temperature responses with selected fuels during 7% of MCR/30s load increase.

During load changes, faster responses in CO and NO levels were observed with respect to SO_2 levels (Figure 33), which responses were very slowly due to long residence time of limestone in the hot loop. The stabilization time of CO and NO emissions was relatively long (tens of minutes) after initial peaking.

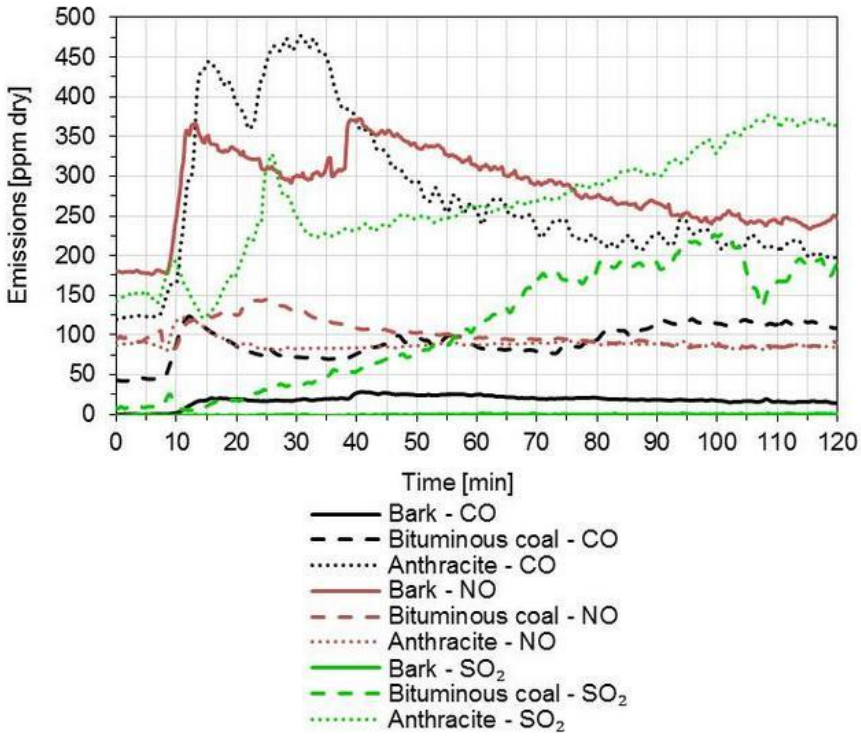

Figure 33. Responses of flue gas emissions with selected fuels during 7% of MCR/30s load increase.

In the additional test sets for bituminous coal, the unburned carbon losses to fly ash and CO emissions were not increased in the stationary tests. In the stepwise tests (±10%), the higher bed temperature and fuel feed staging did not have remarkable effect on the temperature responses or the flue gas oxygen level. On the contrary, the process dynamics were clearly enhanced during the maximum load changes (7% of MCR/30s) at pilot-scale (Figure 34). Fuel staging enhanced the heat up of the hot loop during maximum load increase and thus speeded up the load change rate. The circulation material temperature of 700 ºC was achieved 20 min after the end of the feed ramp, whereas without the fuel staging, the time required was 50 min. Higher bed temperature also speeded up the load change rate, as the target temperature of 700 ºC was achieved in 30 min instead of 50 min.

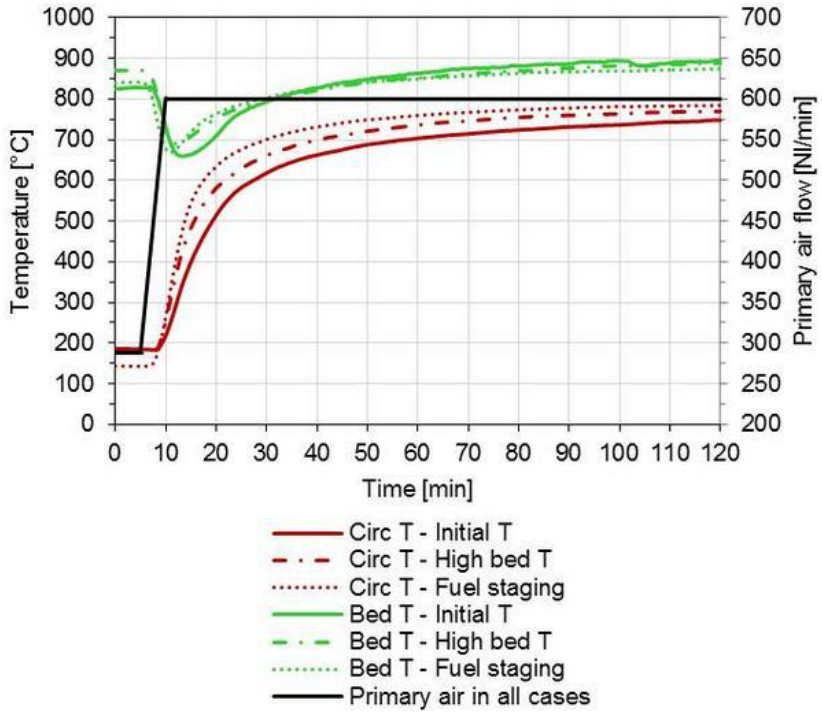

Figure 34. Circulation and bed material temperature responses with bituminous coal under varied combustion conditions during 7% of MCR/30s load increase.

Higher bed temperature level or fuel staging had no remarkable effect on flue gas oxygen level (Figure 35). CO emissions were similar in fuel staging and higher bed temperature level tests, so it can be concluded that the fuel staging did not increase CO emission formation compared to the higher bed temperature level test. However, the CO emission level was lower with initial bed temperature level and a lower peak was observed during the load increase.

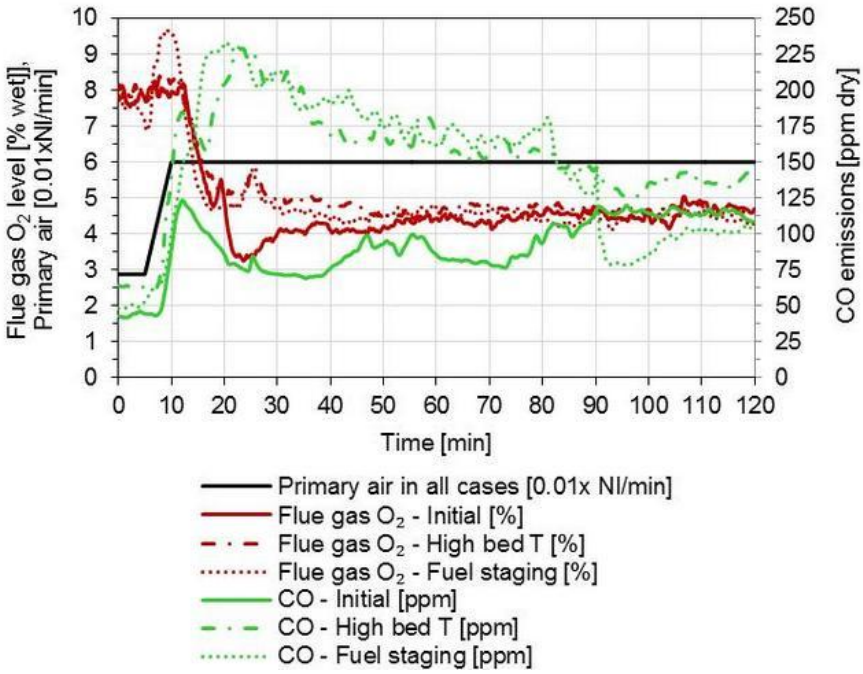

Figure 35. Responses on flue gas oxygen and CO emission levels with bituminous coal under varied combustion conditions during 7% of MCR/30s load increase.

Higher bed temperature level or fuel staging had neither remarkable effects on NO emission level (Figure 36). Some increase and peaking of NO was detected during the maximum load increase followed by slow decrease and stabilization. SO_2 emission levels increased clearly in all the tested conditions. The SO_2 changes were slow due to slow stabilization of limestone inventory in the hot loop.

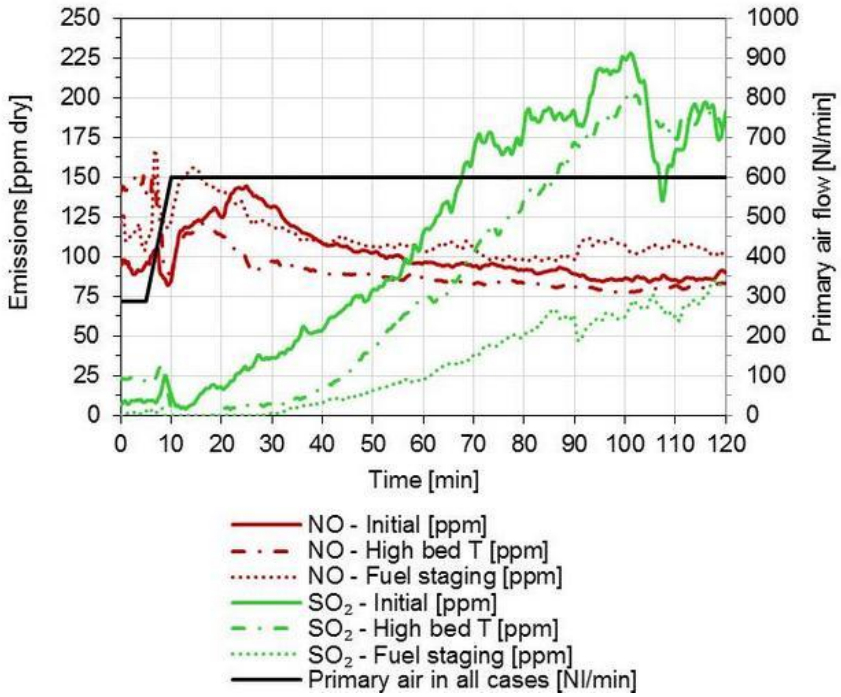

Figure 36. Responses on NO and SO_2 emission levels with bituminous coal under varied combustion conditions during 7% of MCR/30s load increase.

The lowest SO_2 emission level was measured in the fuel feed staging test, which was opposite to expectations and the reason remained unknown. One explanation could be the faster heating of solids circulation, and enhanced limestone calcination and sulphation reactions in the upper furnace, leading to improved sulphur capture in the bed and riser areas during the load increase.

4. Development of virtual CSP and CSP hybrid power plants

4.1 Dynamic simulation software Apros

Dynamic simulation software Apros® is a multifunctional tool for the dynamic modelling and simulation of different industrial processes including their automation and electrical systems (Apros 2016a). The software has been developed since 1986 by Fortum and VTT Technical Research Centre of Finland, and it is committed to continuous development. Currently, it is used in 26 countries for multiple applications, such as nuclear and combustion power plants, pulp and paper mills, general heating and cooling processes, smart cities and alternative power generation applications, such as fuel cells and solar power. Apros can be used for operation and maintenance (O&M), engineering, and research and development (R&D) purposes (Figure 37) in various industrial processes.

Related to the CSP hybrid technologies, Apros has been used to model conventional power plants (Lappalainen et al. 2012), and different CSP plants, such as a LFC plant with DSG (Hakkarainen et al. 2015a) and with molten salt (Hakkarainen et al. 2015b). Wisam et al. (2016) has used Apros to development of a full-scale dynamic model of an existing 50 MW_e Andasol II PTC power plant. Different supercritical CO_2 (sCO_2) concepts represent more innovative CSP technologies (Hakkarainen et al. 2016a), (Hakkarainen et al. 2016b). In the context of modelling and simulating CSP hybrids with Apros, Suojanen et al. (2016) presents both experimental results of combustion dynamics and modelling results of different hybrid configurations. Performance figures of different hybrid process configurations and dynamic interactions between the subsystems of hybrids have been compared in (Suojanen et al. 2017). Scherer et al. (2004) presents results of dynamic study of hybrid combining PTC solar field and fossil fuelled power plant. Henrion et al. (2013) studies the solar power plant steam generation system and particularly its behaviour during a start-up phase.

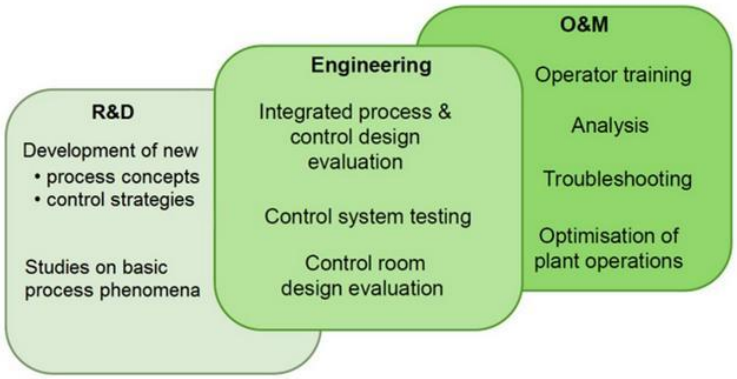

Figure 37. Applications of Apros software.

Thermal hydraulic solution method of Apros is based on non-linear partial differential equations for mass, energy and momentum conservation and correlations for friction and heat transfer (Hänninen et al. 2008). The one-dimensional partial differential equations are solved with finite volume solution method and discretized with respect to space and time into a staggered grid scheme. The non-linear terms are linearized. In the scheme, state variables, such as pressure, enthalpy and density of two phases are calculated in middle of sub-volumes i.e. nodes, and flow variables, such as gas and liquid velocities are calculated in the border of nodes i.e. branches. In the enthalpy solution, first order upwind scheme is applied. The enthalpy is averaged over the node volume. Implicit method is used for temporal discretization, in which linear equation groups for pressure, void fraction and enthalpy are solved one after the other. Based on the solved enthalpy and pressure, density of the node is updated.

The stand-alone and hybrid CSP power plant models developed in the COMBO-CFB project apply both homogenous (3-equation) and heterogeneous two-phase (6-equation) flow models (Apros 2016b). The 3-equation flow model applies one dimensional homogenous two phase flow solution, in which liquid and vapour have the same temperatures and velocities. The three conservation equations include correlations for wall heat transfer and wall friction for the mixture of vapour and liquid. It is a practical solution for modelling of combustion air, flue gas, and part of the steam cycle, in which only water or steam is expected to be present. The 6-equation flow model applies one dimensional heterogeneous two phase flow solution, in which liquid and vapour properties are calculated separately for the two phases. The six conservation equations include correlations for wall heat transfer and friction for liquid and vapour and interfacial heat transfer and friction between liquid and vapour. It is especially suitable for accurate simulation of two-phase flow in the evaporator of steam boiler, evaporator collectors of the solar field and condensing heat surfaces.

4.2 Defining solar field performance

The define the performance of the solar field, both optical and thermal behaviour needs to be taken into account. Regardless the CSP technology, the thermal power of the solar field (P_{th}) is defined as in Eq. 7, in which A is the primary reflector aperture, η_{opt} is optical efficiency and P_{loss} is thermal loss.

$$P_{th}=A\cdot(DNI\cdot\eta_{opt}-P_{loss}) \tag{7}$$

Both parabolic trough and linear Fresnel are line-focusing technologies, and their optical efficiency (η_{opt}) can be described as in Eq. 8, in which η_0 is the peak optical efficiency, K_T and K_L are transversal and longitudinal incidence angle modifiers, respectively, Θ_T and Θ_L are transversal and longitudinal incidence angles, respectively, and f_{cl} is the cleanliness factor, which describes the reduction of the optical efficiency due to soiling of mirrors. The incidence angle modifier (IAM) describes the reduction of the optical efficiency, in the case of PTC due to the incidence angle, and in the case of LFC due to both the incidence angle and the transversal angle (Schenk et al. 2014). As a result, in the case of LFC, the IAM is a product of the transversal and the longitudinal components (Eq. 8), whereas only the longitudinal component is needed for PTC. IAMs are typically provided by the collector manufacturers as a function of incidence angle.

$$\eta_{opt}=\eta_0\cdot K_T(\Theta_T)\cdot K_L(\Theta_L)\cdot f_{cl} \tag{8}$$

In the case of central receiver technology, the heliostat field efficiency (i.e. the collector efficiency) (Eq. 9) is calculated by taking into account all the necessary losses including atmospheric losses, cosine loss, local atmospheric attenuation, reflectance, blocking and shading, and spill losses. The respective efficiencies in order are: atmospheric (η_{atm}), cosine (η_{cos}), attenuation (η_{att}), reflection (η_{refl}), mirror blocking (η_{block}), mirror shading (η_{shade}) and spill (η_{spill}) efficiency.

$$\eta_{tot,col}=\eta_{atm}\cdot\eta_{cos}\cdot\eta_{att}\cdot\eta_{refl}\cdot\eta_{block}\cdot\eta_{shade}\cdot\eta_{spill} \tag{9}$$

Thermal energy loss from the absorber tubes is typically calculated as a temperature dependent heat loss with manufacturer's specification. A general form of the temperature dependent heat loss (P_{loss}) is given in Eq. 10, in which u_0–u_3 are heat loss coefficients and ΔT is the temperature difference between absorber mean temperature and ambient temperature.

$$P_{loss}=u_0\cdot\Delta T+u_1\cdot\Delta T^2+u_2\cdot\Delta T^3+u_3\cdot\Delta T^4 \tag{10}$$

Based on the Equations 7−10, the thermal power of the solar field defined as in Eq. 11.

$$\eta_{th}=\frac{A\cdot(DNI\cdot\eta_{opt}-P_{loss})}{DNI\cdot A}=\frac{P_{th}}{DNI\cdot A} \tag{11}$$

In the case of Brayton cycle CSP plant (Chapters 5.3 and 5.4), the net power production of the CSP plant, P_{net}, is defined as the difference between the turbine power P_{tur} and the compressor power P_{comp} and the pump power P_p (Eq. 12). The efficiency indicator, plant net thermal efficiency, η_{net}, is defined as the ratio of the net power P_{net} and the solar field thermal power P_{th} (Eq. 13).

$$P_{net}=P_{tur}-P_{comp}-P_p \tag{12}$$

$$\eta_{net}=\frac{P_{net}}{P_{th}} \tag{13}$$

4.3 Defining CSP hybrid plant performance

The performance analysis of hybrid CSP power plant is based on the first law of thermodynamics. First law or energy efficiency η_I is used in the efficiency determination:

$$\eta_I = \frac{\text{energy output}}{\text{energy input}} \tag{14}$$

The energy output is the power output ($P_{turbine}$) of the hybrid system, and the energy input is either the thermal power ($Q_{th,boiler}$) or the fuel power ($Q_{fuel,\ boiler}$) of the steam boiler and thermal power ($Q_{th,solar}$) of the solar field. As a result, the thermal efficiency ($\eta_{thermal}$) is calculated by applying thermal powers as presented by Feng et al. (2016) and the net efficiency (η_{net}) is calculated by applying fuel power of the steam boiler and thermal power of the solar field as applied by Popov (2011):

$$\eta_{thermal} = \frac{P_{turbine}}{Q_{th,boiler} + Q_{th,solar}} \tag{15}$$

$$\eta_{net} = \frac{P_{turbine}}{Q_{fuel,boiler} + Q_{th,solar}} \tag{16}$$

Similarly to the efficiencies, the thermal and net solar shares ($x_{solar,th}$ and $x_{solar,net}$) can be calculated:

$$x_{solar,th} = \frac{Q_{th,solar}}{Q_{th,boiler} + Q_{th,solar}} \quad (17)$$

$$x_{solar,net} = \frac{Q_{th,solar}}{Q_{fuel,boiler} + Q_{th,solar}} \quad (18)$$

In addition, several other performance parameters are of interest during the simulations. These include:

1) Achieved CO_2 emission reductions and fuel savings,
2) Inlet steam mass flows of different turbine sections, as the turbine sections are expected to be in imbalance,
3) Live steam and reheated steam temperatures as well as injection mass flows of superheater and reheater in the CFB boiler, as the thermal balance between the heat surfaces is expected to change,
4) Condensing power and water fraction of expanded steam before the condenser, as the water consumption of condenser might increase due to imbalance of heat surfaces and turbines and the water fraction of expanded steam must stay under 12%, and
5) Flue gas temperature before stack, as the dew point of flue gas might be one limiting factor for the maximum solar share.

5. Virtual stand-alone CSP concepts

Several CSP technologies and concepts were modelled and analysed with Apros dynamic simulation software in the COMBO-CFB project. The CSP models include linear Fresnel collector (LFC) solar field with direct steam generation (Chapter 5.1), direct two-tank molten salt plant applying LFC technology (Chapter 5.2), direct-heated (Chapter 5.3) and indirect (Chapter 5.4) sCO_2 Brayton cycle with LFC solar field, and central receiver solar field model including combined calculation of optical and thermal behaviour (Chapter 5.5).

Dynamic simulation is needed to study the highly dynamic behaviour of solar fields exposed to varying irradiance conditions, test new control systems and operation strategies, and optimise the power plant design and production.

5.1 Direct steam generating linear Fresnel solar field

Linear Fresnel collector (LFC) technology has been in recent years under intensive development in terms of utilising it in high-temperature power cycles instead of low- or medium-temperature heat generation, and has proceeded to commercialisation phase by several companies, such as the German Novatec Solar (currently FRENELL GmbH) (Zhu et al. 2014), (International Energy Agency 2014). Linear Fresnel technology suffers from lower optical efficiency compared to the parabolic trough technology, but this disadvantage can be overcome by simpler structure leading to lower costs. The LFC technology has been considered as a technology with significant potential for future cost reductions. (Morin et al. 2012 a)

5.1.1 Modelling approach of the direct steam generating linear Fresnel solar field

The solar field studied in this Chapter applies linear Fresnel technology with direct steam generation (DSG). The collector design is similar to the Novatec Solar's SuperNova design. Technology has been successfully implemented in commercial scale in Puerto Errado 1 (1.4 MWel) in Spain, by adding a superheating unit into existing power plant. The plant represents the state-of-the-art in Fresnel technology by generating superheated steam at temperatures of 450−500 ºC, thus improving plant efficiency and economics. Applied superheated steam pressure in LFC

fields varies according to references from 80 to 90 bar (Selig & Mertins 2010), (Coco-Enríquez et al. 2013). The plant consists of evaporation section applying cavity receivers and superheating section applying vacuum receivers in order to minimise the heat losses. Both receiver types utilise secondary reflector. Vacuum receiver represents a standard Schott PTR70 vacuum receiver used in the currently operating parabolic trough power plants (Schott Solar). Both primary mirror fields and control systems of mirror tracking are identical. (Zhu et al. 2014), (Morin et al. 2011)

The solar field is run with recirculation operation mode, in which more feedwater is fed to the solar field than is evaporated. The mixture of water and steam enters the phase separator tank located between the evaporator and superheater sections (Figure 38), and water is recirculated back to the solar field inlet. The separator tank of the row represents a distributed field separator i.e. every collector row has its own separator. Saturated steam is led to the superheater section, where the steam is superheated to its design temperature. The pressure level of the feedwater is increased with a feedwater pump in order to take into account the pressure losses in the solar field and guarantee the desired fixed outlet pressure. The recirculation mass flow rate is kept constant over the day and thus, the feedwater temperature at the inlet of evaporator collectors varies according to irradiance level. As a result, the temperature is at its lowest during the maximum irradiance level.

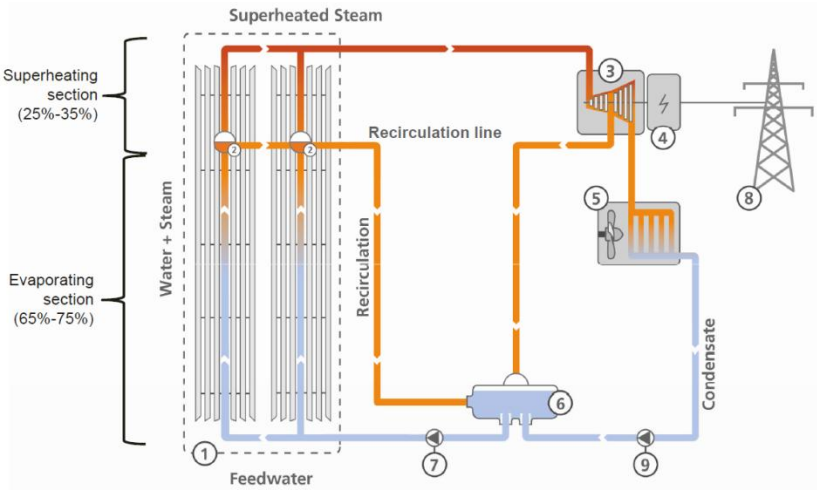

Figure 38. Simple diagram of power plant layout applying Novatec Solar's SuperNova technology; evaporation section based on Nova-1 technology and superheating section based on SuperNova technology (Novatec Solar 2013).

The field consists of control units each having a length of 44.8 m. One collector row can include from 5 to 22 control units connected in series, and several collector rows can be set in parallel to form a solar field. Table 4 shows the main dimensions and thermal performance values of a collector unit under nominal conditions

both for Nova-1 collector (non-vacuum) applied in evaporation section and for SuperNova collector (vacuum) applied in superheating section.

Table 4. Collector dimensions and thermal performance underdesign conditions for both non-vacuum and vacuum tube collectors (Novatec Solar), (Novatec Solar 2013), (Morin et al. 2012 b).

	non-vacuum	**vacuum**	**unit**
width	16.56	16.56	m
length	44.8	44.8	m
absorber tube height above primary reflector level	7.4	7.4	m
primary reflector aperture	513.6	513.6	m^2
receiver tube inner diameter	66	66	mm
receiver tube outer diameter	70	70	mm
receiver tube wall thickness	2	2	mm
ambient temperature	40	40	ºC
inflow temperature	100	300	ºC
outflow temperature	300	500	ºC
wind conditions	no wind	no wind	m/s
DNI	900	900	W/m^2
transversal angle	30	30	º
incidence angle	10	10	º
thermal output per control unit	276	270	kW
thermal output per primary reflector aperture	537	525	W/m^2

The solar field of this study is composed of 16 solar collectors in evaporation section (length 716.8 m) and 6 collectors in superheating section (length 268.8 m) having the total length of 985.6 m, superheating section representing 27% of this (Figure 39). This reference configuration can be easily modified according to user needs. The main objectives of the solar field control system are to guarantee sufficient cooling in the evaporator tubes and desired superheated steam pressure and temperature at the solar field outlet. Control system applies simple PI controllers.

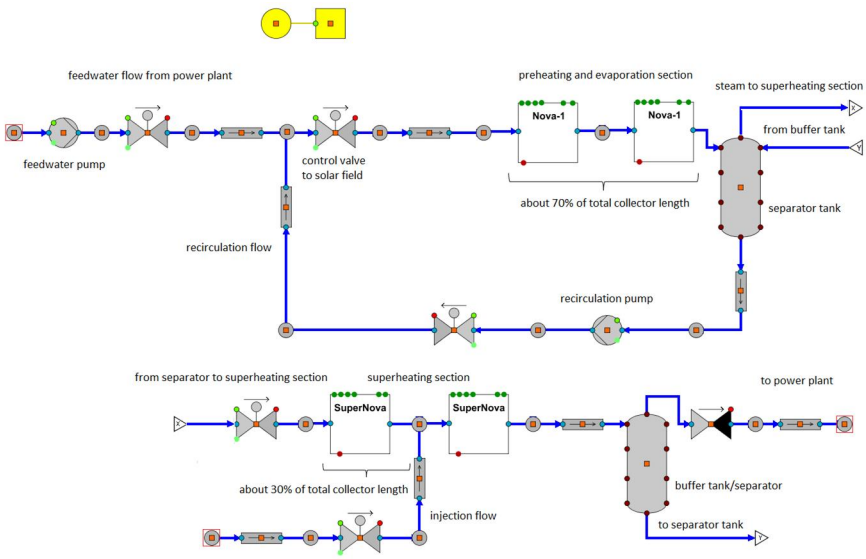

Figure 39. Simplified schematic Apros process diagram of one collector row.

5.1.2 Results of simulation cases

The LFC solar field with DSG was tested with example simulations in order to verify reasonable functionality of the model. Simulations were carried out at two different locations during two selected dates. Simulation dates were June 21st i.e. solstice and March 21st i.e. equinox. Simulation locations were selected to be representative plant locations; in this case the location of Puerto Errado 1 power plant in Spain (location 1), and the location of Pedro de Valdivia (location 2), under development being parabolic trough plant in Chile. In both locations collector rows are oriented in North-South direction. Simulations are performed under clear sky irradiance conditions. Information about simulation cases is shown in Table 5.

Table 5. Information about the simulation locations.

	Location 1	**Location 2**
site	Puerto Errado 1, Murcia, Spain	Pedro de Valdivia, Antofagasta, Chile
latitude (ºN)	38.278411	-22.7177778
longitude (ºE)	358.3997195	290.4138889
standard meridian longitude (ºE)	360	300
Turbidity Linke factor	March: 3 June: 4	March: 2 June: 1.5

Some of the results of four simulation cases i.e. June 21st and March 21st in Spain (location 1) and in Chile (location 2) are shown in Figure 40−Figure 42 in order to discover general behaviour of the solar field configured. Simulation result trends for one collector row obtained in case simulations at different locations during different dates show good consistence to generally known solar field behaviour and when compared to each other. Irradiation levels are revealed to have minor seasonal changes between simulated dates on June and March at the location 1 (Figure 40 a) compared to location 2 (Figure 40 b).

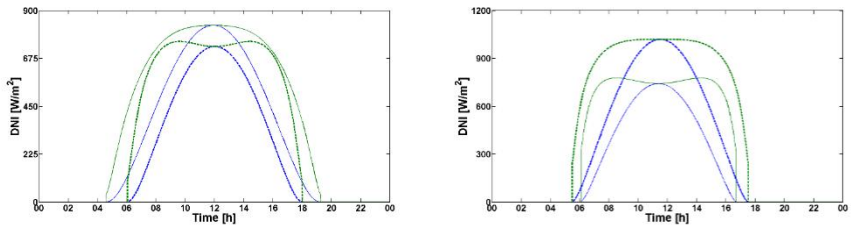

Figure 40. Direct horizontal irradiance (blue) and direct normal irradiance on tracking surface (green) on June 21st (solid line) and March 21st (dashed line) a) at location 1 and b) at location 2.

Thermal power trends of both evaporator and superheater (Figure 42) correspond to the DNI levels. Simulation results show that the studied solar field is able to produce superheated steam at desired stable conditions under different irradiation levels during clear sky conditions. Inlet and outlet temperatures of the superheater are shown in Figure 41. Superheater, and especially evaporator (not shown in figures), inlet conditions varies greatly, but the outlet conditions are kept stable. Stable maintained superheated steam conditions lead to a conclusion of a proper working control system. The complexity of the evaporator mass flow control according to varying field inlet temperature leads to fluctuation in evaporator thermal power (Figure 42). It must be noted that the simulations are done under clear sky conditions, and when taking into account fast transient changes caused by overcast conditions, more demands are set to the control system.

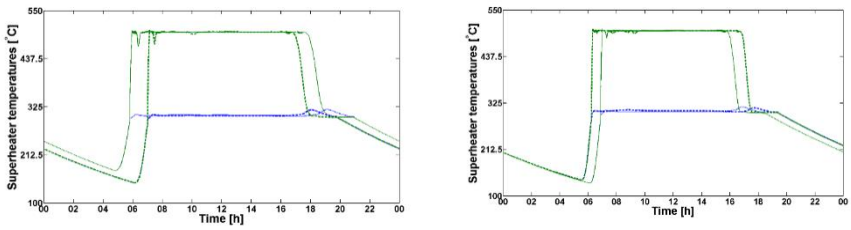

Figure 41. Temperature at the superheater inlet (blue) and outlet (green) on June 21st (solid line) and March 21st (dashed line) a) at location 1 and b) at location 2.

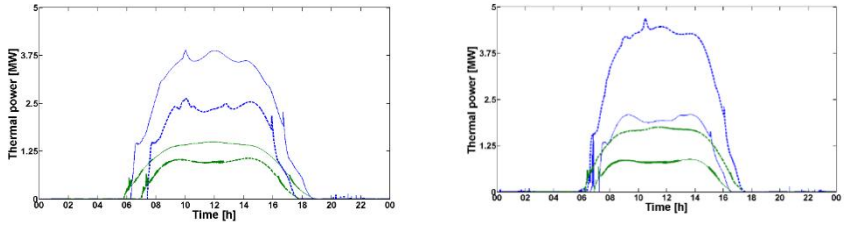

Figure 42. Thermal power of the evaporator (blue) and superheater (green) on June 21st (solid line) and March 21st (dashed line) a) at location 1 and b) at location 2.

5.1.3 Importance of irradiance forecast accuracy for production estimates

Solar is a variable source of energy and undergoes both slow changes due to time of the day and year, and rapid changes due to changing weather conditions i.e. changing overcast conditions. Solar field is exposed to transient irradiation conditions and to changes in the inlet water temperature and pressure. In the case of direct steam generation, which is usually applied in LFC solar fields, the amount of steam produced varies according to inlet water conditions and irradiation in order to maintain both outlet steam temperature and pressure stable. This sets challenges for the field control system. (Valenzuela et al. 2006) Irradiance forecasts with different forecast horizons are essential both from the point of view of plant controls and predicting the plant production.

Long forecast horizons enhance the development of beneficial plant operation strategies in different energy markets and the predictability of plant hourly operation. The importance of forecast accuracy for production estimations was studied in COMBO-CFB by Vaisala and VTT. Vaisala offers solar and weather measurement systems and produces solar irradiance forecasts up to 7-day forecast horizon. Hour ahead DNI forecasts are based on global numerical weather prediction model and site-specific MOS-correction. Vaisala's irradiance forecasts were integrated to Apros model of LFC solar field developed by VTT. This enabled to study the sensitivity of production estimates of CSP plant on irradiance forecast accuracy.

Apros was used both to demonstrate the actual production based on measured high resolution DNI data and to produce production estimates based on Vaisala's DNI forecasts. In addition, Apros generates theoretical clear sky DNI data. The solar field simulated was a 5.19 MW_{th} DSG linear Fresnel solar field. The solar field was places to geographical location of Boulder, Colorado (39.969 ºN, 105.118 ºW). DNI forecasts for target days (day N is either 14th June, 15th June or 16th June) were initialized at different times: at the same morning (N 5 am), one day before (N-1 8 pm and N-1 5 am) and two days before (N-2 8 pm). Forecasted DNI data with different initialization times, measured DNI data and clear sky data generated in Apros are show in Figure 43, and corresponding thermal power pro-

duction estimates simulated in Apros for each case are shown in Figure 44 for June 14th–16th.

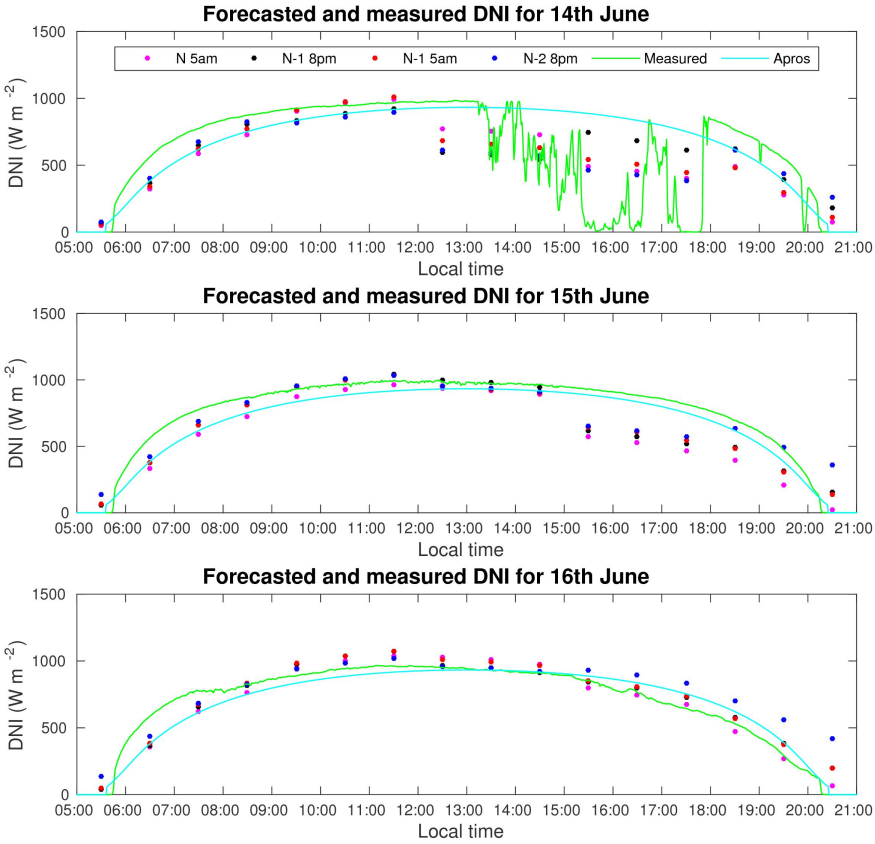

Figure 43. Forecasted DNI with different forecast initialization times, measured DNI and DNI generated in Apros for June 14th–16th.

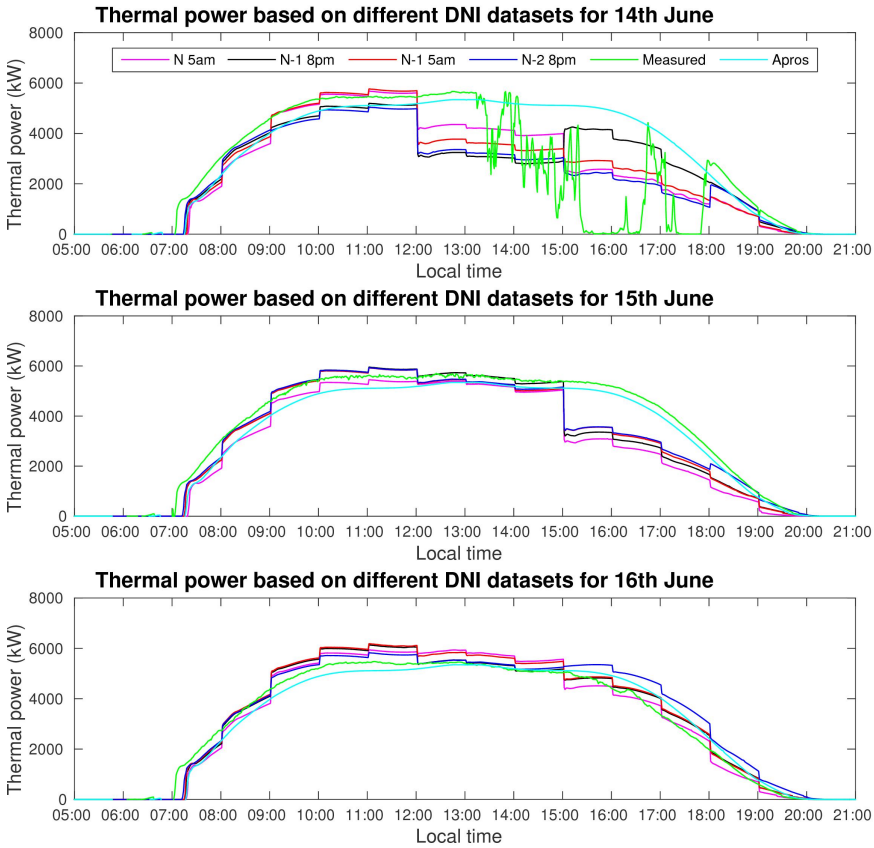

Figure 44. Simulated thermal power production for datasets shown Figure 43; thermal power based on DNI forecasted with different initialization times, thermal power based on measured DNI and thermal power based on clear sky DNI.

Figure 45 shows the hourly absolute forecast errors in thermal power production for each of the case in Figure 44. The results show that the hourly error can grow large if clouds are not forecasted right. If looking on the daily production estimate, it must be noted that an hour with high forecast error can cause a high error in daily production estimate, though the forecasts for other hours would be precise. On the other hand, daily errors may cancel out in daily errors. By simulating high number of days, the cloud effects and their impacts on hourly and daily DNI and production estimates could be classified under specific conditions (certain sites).

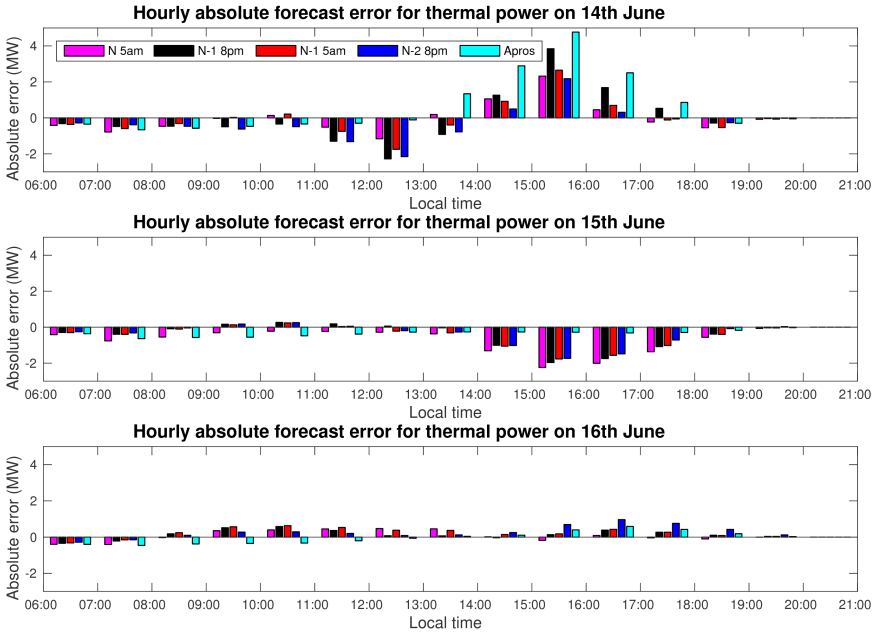

Figure 45. Hourly absolute forecast error for thermal power production for all the cases shown in Figure 44.

5.2 Molten salt solar field with two-tank thermal energy storage system

Superheated steam temperatures up to 480−520 ˚C are reported to be achieved in demonstrations of direct steam generating LFCs. Despite many advantages in DSG, it lacks cost effective and technically convenient solution for large-scale thermal energy storage (TES) integration. (Zhu et al. 2014) In recent years, studies on utilisation of molten salts both in LFC and PTC based solar fields with direct storage system have been made. The concept allows storing of energy for long time periods in the range of hours. The indirect molten salt storage system exploited in the currently operating PT plants with oil as HTF is already commercial technology, and the solar tower technology with direct molten salt (DMS) storage system is implemented in commercial scale in Gemasolar power plant (Relloso & García 2014). First DMS demonstration plants for line-focusing technologies are already constructed for testing, by Novatec Solar based on the LFC technology (Morin et al. 2015) and by Archimede Solar Energy based on the PTC technology (Maccari et al. 2015).

Nitrate salts have many favorable properties for solar applications: low corrosion rate with common piping materials, thermal stability in the upper temperature range of the steam Rankine cycle, good heat transfer properties, very low vapor pressure, wide availability, low environmental impact and they are relatively inex-

pensive (Grena & Tarquini 2011), (Kearney et al. 2003). The controllability of the solar field is easier in the case of liquid one-phase flow than in the case of two-phase flow in DSG (Valenzuela et al. 2006). The major challenge with molten salt is the high freezing point, about 120 ˚C and 220 ˚C for ternary and binary salts, respectively, vs. about 15 ˚C for synthetic oil. Consequently, freeze protection is required, such as preheating the piping with Joule and trace heating, salt recirculation, external burner and draining of the salt. (Morin et al. 2015), (Kearney et al. 2003) In the case of molten salt, LFC technology has some advantages with respect to PTC technology, such as fixed receiver, higher concentration factor and easier salt drainage, described more closely in (Morin et al. 2015), (Grena & Tarquini 2011). With respect to solar tower technology, control of heat flux onto receiver is easier to handle due to lower concentration ratio, which can be compensated by lower heat loss, risk of salt freezing is lower and auxiliary power for pumping is smaller (Morin et al. 2015).

According to Kearney et al. (2003), molten salt allows significant increase in the parabolic trough solar field outlet temperature, thus increasing the plant efficiency, compared to the current oil based PT solar fields (Kearney et al. 2003). Grena & Tarquini (2011) evaluates that the efficiency of specific molten salt Fresnel system is between 10% and 20% lower with respect to a PTC with molten salt. However, the reduction in costs can maintain the LFC technology competitive. (Grena & Tarquini 2011) The increased temperature rise in the molten salt solar field reduces the size of the TES for a given capacity. Other advantages of molten salts compared to currently used oils are the lower cost and environmental issues. (Kearney et al. 2003)

The study establishes a first qualification of using Apros for dynamic simulation of DMS Fresnel technology.

5.2.1 Modelling approach of the direct molten salt linear Fresnel solar field

The model development of the concept comprises modelling of several subsystems, namely linear Fresnel solar field, two-tank storage system, molten salt/water-steam heat exchanger, power block, control system, and fluid and material properties. The size and thermal power of the solar field are easily scalable in the model configured. Two-tank direct molten salt thermal energy storage system and steam generator (SG) are integrated into the solar field in order to produce constant power around the clock, and a simple control system in configured. Turbine and generator are excluded from the model. In this study, the size of the solar field is varied between two example simulation cases having different irradiation conditions, so that constant thermal power in the steam generator can be produced round the clock. Figure 46 shows a simplified process diagram of the solar field model in Apros.

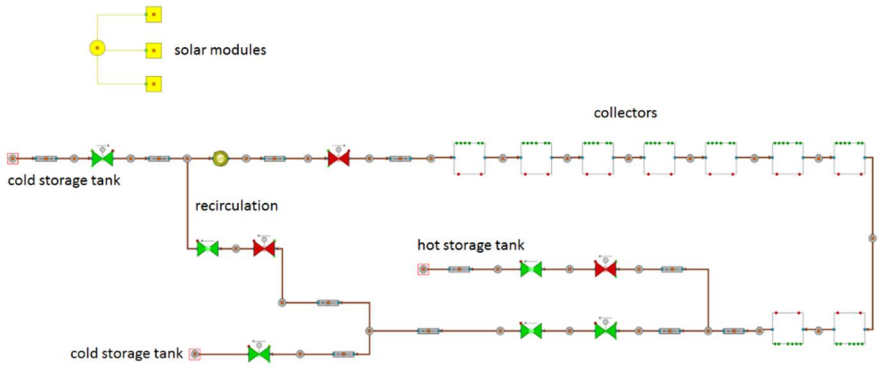

Figure 46. Simplified schematic process diagram of the solar field model in Apros. White squares represent LFCs, and green and red dots are input and output variables, respectively.

The heat transfer fluid used in the concept is a nitrate salt mixture having commercial name Hitec; its composition is described in Table 6. Hitec has a melting point of 142 ºC and upper temperature limit of 535 ºC. The salt mixture becomes thermally and chemically unstable at temperatures above 600 ºC. The main properties mentioned above are applied as presented in Boerema et al. (2012). (Boerema et al. 2012)

The CSP plant model configured includes two-tank direct molten salt thermal energy storage system having hot and cold storage tanks with nominal operating temperatures of 510 ˚C and 280 ˚C, respectively. The temperature difference of salt over storages is 230 ˚C, resulting in specific storage energy capacity of 74.4 kWh/tsalt. The temperature of the cold tank is expected to vary in the range of 270−290 ºC depending on daily operational conditions and control strategy, as the temperature of the hot tank is expected to vary in the range of 490−515 ºC.

The solar field includes a steam generator with 17 MW_{th} thermal power under nominal conditions. The nominal superheated steam temperature is 450 ºC and pressure 90 bar. The SG consists of three parts: preheater, evaporator and superheater. The thermal power of the evaporator is calculated with pinch point of 20 ºC. The nominal temperature in the hot tank is desired in order to allow the steam generator to work under its nominal conditions.

The operation strategy is to produce hot molten salt the amount that is needed for stable round the clock operation of SG, with target temperature of 510 ºC, under different irradiance conditions. The number of collector rows in the two simulation cases (Chapter 5.2.2) is set so that constant power with target temperatures can be achieved in the SG round the clock; any optimisation for year around operations with a certain SF is not done.

It is desired to achieve constant solar field outlet temperature in order to keep the temperature in the hot TES at its design point to ensure good steam generation efficiency. In this study clear sky conditions are applied, and the molten salt mass flow is controlled according to the level of irradiance.

An important issue in the SF operation is the night time freeze protection of molten salt. Due to relatively high temperature of cold TES tank, its thermal energy can be used for this by recirculating molten salt from cold tank in the solar field during times without irradiation, as proposed for example by Kearney et al. (2003). By using energy from cold tank instead from hot tank, temperature dependent heat losses can be minimised. Energy utilisation from storage tank is reduced by taking advantage of residual heat and thermal inertia in the SF after appropriate temperature level for the hot storage tank is not achieved anymore in the evening. When solar field is cooled to 280 ºC, recirculation control mode starts and continues until the start-up of the solar field next morning. The cold tank has to be heated up again in the morning to its design temperature, which consumes solar thermal energy collected in the beginning of SF operation (Kearney et al. 2003). During SF start-up, temperature in the hot tank might slightly drop before the field target outlet temperature is achieved.

5.2.2 Results of simulation cases

Simulation cases were performed with the coordinates of Aldiere, Granada, Spain (the location of Andasol 1 PT plant). The coordinates of the location are 37°13′ 50.83″ North and 3°4′ 14.08″ West. Simulations were done at two different dates having different levels of clear sky irradiance; June 21st representing summer solstice (referred as Case 1) and March 21st representing spring equinox (referred as Case 2) in the northern hemisphere. Simulations were carried out for full 24 hours i.e. full operational cycle of the solar field.

Simulations utilise monthly mean values both for Turbidity Linke (TL) factor and day time temperature. For June 21st TL factors for June and March are 3.4 and 2.4, respectively. Day time temperatures for June and March are 23.3 ºC and 12.5 ºC, respectively. (SoDa)

Main parameters of the CSP plant components in both simulation cases are shown in Table 6. In Case 1, solar field consists of 19 parallel collector rows, as in Case 2, the amount is 30. The amount of collector rows is evaluated so that the hot TES is able to provide molten salt at 510 ºC for the SG over 24 hours, with constant power of around 17.0 MW_{th}. The design point in both cases is fixed at the solar noon (solar time) of the date under consideration. Consequently, thermal power of the SF is 45.2 and 47.7 MW_{th} in the case 1 and 2, respectively, and the corresponding solar multiples are 2.7 and 2.8.

Table 6. Main parameters of the CSP plant components in both simulation cases.

Component		
Solar field		
number of collector rows	Jun 19 / Mar 30	-
collectors per row	9	-
collector row length	403.2	m
total reflector area	Jun 87,825.6 / Mar 138,672	m^2
receiver nominal mass flow	8.7	kg/s
nominal inlet temperature	280	ºC
nominal outlet temperature	510	ºC
heat transfer fluid	53% KNO_3+40% $NaNO_2$+7% $NaNO_3$	Hitec
collector row nominal thermal power	2.33	MW_{th}
Storage system		
hot TES temperature	510	ºC
cold TES temperature	280	ºC
molten salt inventory	6,000	t
tank volume	4,000	m^3
Steam generator		
steam outlet temperature	450	ºC
nominal thermal power	17.0	MW_{th}

In Figure 47−Figure 51, Case 1 i.e. June 21st is referred with solid line and Case 2 i.e. March 21st with dashed line. Irradiance trends of both simulation cases are shown in Figure 47 a. The difference in DNI on tracking surface at noon (solar time) between two cases is less than 100 W/m^2, but the effect on the performance of one collector row is relatively high. Shapes of the optical and thermal efficiency curves (Figure 47 b) indicate the effect of incidence angles and consequent IAMs on the irradiance received on the HTF. The optical efficiency is theoretically achievable efficiency and does not take into account mirror operations; the time delay from positive optical efficiency to start of power production in the morning is due to mirror focusing step by step after a certain irradiance level is achieved.

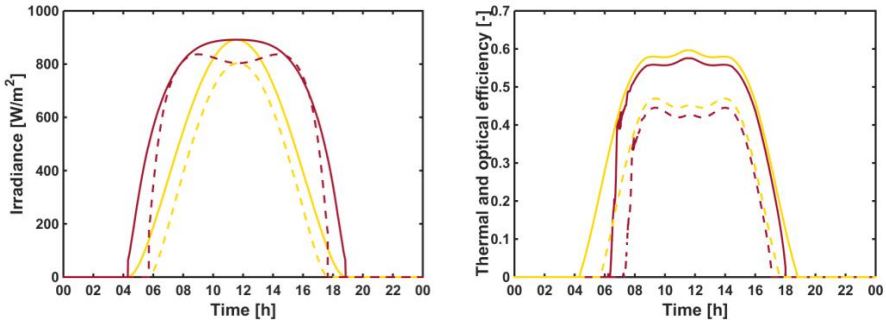

Figure 47. a) Direct horizontal irradiance (yellow) and direct normal irradiance on tracking surface (red); b) Solar field optical (yellow) and thermal (red) efficiency.

Figure 48 a shows the mass flow rate of HTF in a single collector row. The difference in mass flow rates relates straight to the irradiance levels. The molten salt outlet temperature is kept very stable (Figure 48 b). The start-up of the solar field causes challenges for the control system executed simply with PI controllers, especially with high irradiance gradients. That can be noticed as temperature peaks of some degrees in the outlet temperature and as fluctuating mass flow. The control problem can be better handled in the future work by taking more advantage of gradual timing of mirror focusing.

Temperature in the solar field does not fall below 180 ºC during the night (Figure 48 b). The SF inlet temperature is the same as the temperature of the cold storage tank, except in the evening during the recirculation operation mode.

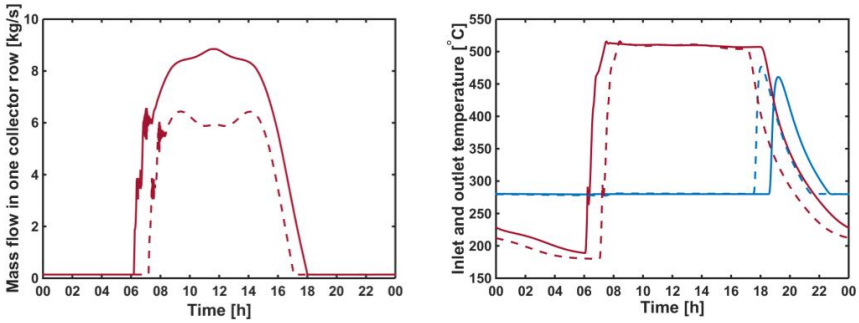

Figure 48. a) Molten salt mass flow in one collector row; b) Solar field daily inlet (blue) and outlet (red) temperatures.

Thermal power production of the entire solar field is slightly higher in Case 2 than in Case 1, 408.4 MWh vs. 403.3 MWh (Figure 49 a), as any precise equalisation of power production was not done.

Design thermal power of the steam generator was set to 17 MW_{th}. The actual thermal power and superheated steam temperature produced are shown in Figure 49 b. The primary control principle in the SG is to keep molten salt and superheated steam outlet temperatures constant, 280 ºC and 450 ºC respectively. Due to this control strategy (mass flow based temperature control), the achieved thermal power is slightly below the target power and has minor variation (Figure 49 b). Both the superheated steam and molten salt outlet temperature are kept rather constant, except variation of few degrees in steam temperature and even smaller variation in molten salt temperature during the start-up of the solar field. During the start-up in both simulation cases, the higher drop both in superheated steam temperature and production and in SG thermal power is due to temperature drop in the hot storage tank.

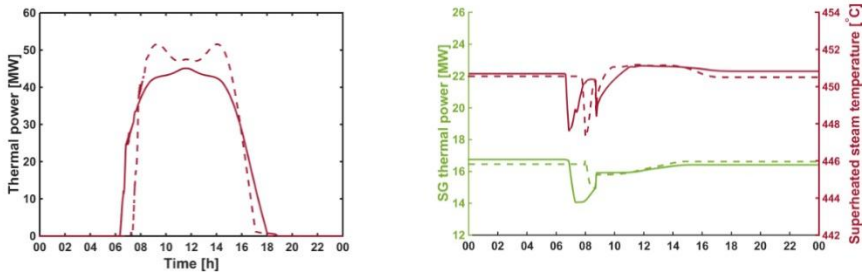

Figure 49. a) Solar field thermal power production; b) Thermal power of SG (green) and superheated steam temperature (red).

Daily variation in hot and cold salt inventories is shown in Figure 50. The salt content in the tanks was kept above the 10% minimum limit. In Case 2, the hot salt inventory achieves lower value than in Case 1, as the thermal power production in the SF starts later in Case 2.

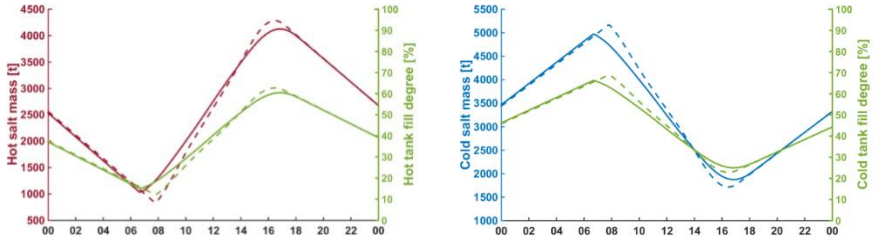

Figure 50. a) Daily variation in hot salt mass in the hot storage tank (red) and in tank fill degree (green); b) Daily variation in cold salt mass in the cold storage tank (blue) and in tank fill degree (green).

Variation in the storage tank temperatures is shown in Figure 51. The control strategy during the SF start-up explains the temperature drop in the hot TES in the morning. The cold TES temperature gradually decreases at night and the inventory is heated up in the beginning of the SF start-up. However, the daily variation in the cold tank temperature is small.

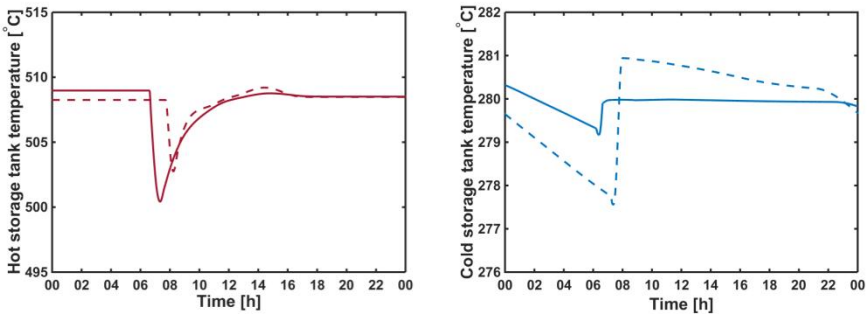

Figure 51. a) Daily temperature variation in hot storage tank; b) Daily temperature variation in cold storage tank.

5.3 Direct-heated supercritical carbon dioxide CSP concept

Parabolic trough solar field with thermal oil as HTF represents the most mature CSP technology, whereas water/steam and molten salts are other typical HTFs. However, new HTF options are searched in order to increase the efficiency of energy production and decrease energy generation costs. One promising option is supercritical carbon dioxide (sCO_2), which is currently a widely researched topic for different power conversion technologies (Ahn et al. 2015). In the case of CSP technology, sCO_2 could be used both as HTF in the solar field and working fluid in the power cycle. The topic has been studied for example at Sandia National Laboratories (Sandia National Laboratories 2015) and in NREL (NREL) within SunShot Initiative, but no commercial plant has been built. Supercritical CO_2 is an attractive HTF and working fluid option, and at least the following benefits can be achieved by using sCO_2 as the power cycle working fluid with respect to other fluids (Ahn et al. 2015), (Ma & Turchi 2011), (Sandia National Laboratories), (Singh et al. 2013):

- Inexpensive, abundant, non-toxic, non-combustible and non-explosive fluid
- High temperatures can be used
- Moderate critical pressure (7.38 MPa) and temperature (31.1˚C)
- Reduced compression work due to the fluid properties in the supercritical area (compressibility factor 0.2–0.5 near the critical point) and higher thermal efficiency
- Smaller component sizes relative to steam cycle, leading to reduced capital cost
- Faster start-ups and load changes due to lower thermal mass in the system
- Reduced water consumption in cooling process
- No pinch point in heat exchanger

The concept studied uses sCO_2 both as the HTF in the Linear Fresnel collector solar field and as the working fluid in the closed Brayton power cycle. The direct heating of sCO_2 in the solar field has been previously studied for example in (Singh et al. 2013), and in order to benchmark the results, the main cycle parameters were adapted from that reference. However, the model developed in the COMBO-CFB project takes the concept a step forward in terms of studying the dynamic behavior of the process under varying operational conditions. The off-design behavior of the sCO_2 Brayton cycle has been studied before e.g. by Dyreby et al. (2011), but not in the context of solar thermal application.

5.3.1 Modelling approach of the direct-heated sCO_2 CSP concept

The model development of the sCO_2 solar field directly connected to the Brayton cycle comprises modelling of several subsystems, namely linear Fresnel solar field, power block, control system, and fluid and material properties. The concept and its main components (a−f) are illustrated in Figure 52.

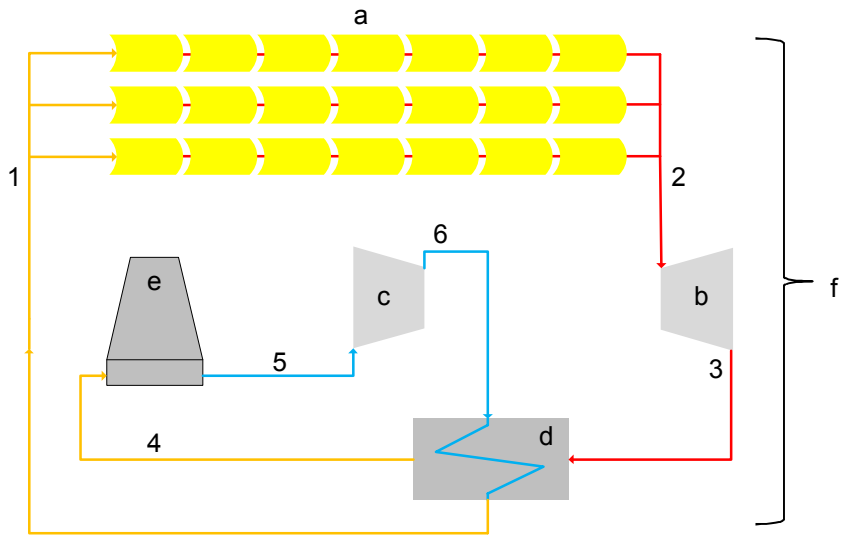

Figure 52. Schematic process diagram of the linear Fresnel solar field with the sCO_2 Brayton cycle (generator is excluded from the model); a is linear Fresnel solar field including 21 collectors aligned to three collector rows, b is one-stage sCO_2 turbine, c is compressor, d is recuperator, e is dry cooler and f is control system. Number 1−6 refer to Figure 53.

The design point of the system is set to 21st of June at 12:00 with the geographical position of Ouarzazate, Morocco (31.004 ˚N, 6.864 ˚W). Figure 53 shows the pressure, enthalpy and temperature of CO_2 at nominal conditions in process points (see Figure 52) and the critical point of CO_2.

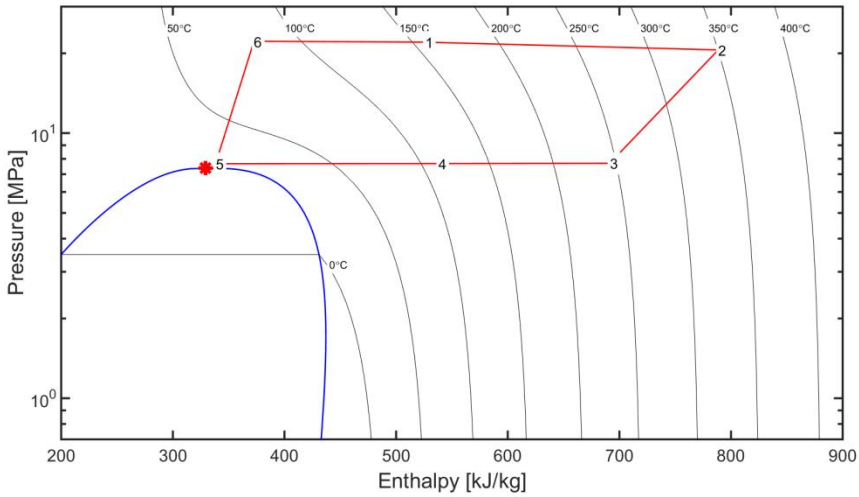

Figure 53. sCO_2 Brayton cycle at nominal conditions in pressure−enthalpy diagram with numbers 1−6 marking the points in the cycle (see Figure 52) and the red star marking the critical point.

The main design parameters of the system are shown in Table 7. Recuperator hot side refers to the side, in which the flow enters from the turbine, heats the cold side flow and leaves to the dry cooler. Cold side refers to the side, in which flow enters from the compressor, receives heat from the hot side and enters to the solar field.

Table 7. Main parameters of the subsystems of the sCO_2 CSP plant at the design point.

Component	Capacity [MW]	Mass flow [kg/s]	Inlet temperature [˚C]	Inlet pressure [MPa]	Outlet temperature [˚C]	Outlet pressure [MPa]
Solar field	5.37	20.90	160.0	22.50	350.0	21.10
Turbine	2.10	20.90	350.0	21.00	240.0	7.60
Compressor	0.96	20.90	32.0	7.50	90.0	22.70
Net power	1.13	-	-	-	-	-
Recuperator, cold side	2.93	20.90	90.0	22.70	160.0	22.60
Recuperator, hot side	2.93	20.90	240.0	7.60	120.0	7.55
Dry cooler, CO_2 side	4.12	20.90	120.0	7.55	32.0	7.50
Dry cooler, air side	4.12	242.80	20.0	2.50	36.5	1.00

The solar field consists of linear Fresnel collector modules, which use vacuum tube absorbers. The method and the model of collector module is described in (Hakkarainen & Tähtinen 2015a). Heat losses from the other piping than the absorber tubes are neglected in the studies. The solar field is dimensioned to consist of three parallel collector rows, each having seven LFCs, 44.8 m each, with a total length of over 313.6 m. The thermal power of the solar field is 5.37 MWth at the design point. The SF dimensions were selected to guarantee the system net power of over 1 MW (see Eq. 12) and reasonable fluid velocities in the piping network under design conditions, when the fluid is heated from 160 ˚C to 350 ˚C. Each collector row is equipped with control valve in the inlet side.

Turbine is dimensioned to operate at nominal inlet state of 21 MPa and 350 ˚C, and to expand the sCO_2 to an outlet pressure of 7.83 MPa. Nominal mass flow through the turbine is 20.9 kg/s. Isentropic expansion efficiency was set to 90% at the nominal state (Dostal 2004).

Since the gas compressibility factor decreases when approaching the critical point, the compressor work resembles more pumping than compression. The pump power consumption of Apros Pump component was checked to be in agreement with the results achieved by using the compressor performance model presented in (Sign et al. 2013) and (Dyreby et al. 2011). The compressor performance model is based on the modified head coefficient, flow coefficient and efficiency, and a performance map presented in (Dyreby et al. 2011).

Recuperator is used to increase the total power cycle efficiency and it was dimensioned to have a logarithmic mean temperature difference (LMTD) of 10 °C at the design point. LMTD of the dry cooler was designed to be 5 °C. The air fan of the cooling system was excluded from the modelling scope. Stainless steel was defined as the construction material for the parts where heat structures were modelled: pipes and heat exchangers.

The system is controlled with five main control loops using PI controllers, and separate sequences are applied for the plant start-up and shut down. The main controlled variable is the inlet temperature of the turbine, which is primarily controlled by the compressor's rotation speed. The set point is 350 ˚C throughout the day, whereas the turbine inlet pressure follows the load level. Additionally, the control valves placed at the inlet of the SF collector rows are manipulated to control the outlet temperature of each collector row separately and to guarantee sufficient pressure drop along the solar field. This control approach avoids unnecessary compressor work and throttling losses of the control valves at the solar field inlet, while the SF outlet temperature is kept constant. The sCO_2 temperature after the dry cooler is controlled by manipulating the cooling air mass flow by a control valve. The temperature is kept constant at 32 ˚C in order to maintain the fluid in the supercritical region during normal operations. Pressure stays above the critical pressure through the turbine design and due to the controlled temperature. However, during the night, the state of the CO_2 moves to subcritical region due to temperature decrease.

In the morning, the system start-up is done by starting the compressor and leading the CO_2 to the solar field. The compressor first runs by minimum speed of

40% in order to avoid fluctuations due to otherwise low mass flow rates at low irradiance level, and to avoid temperature over shooting in the SF outlet. The SF outlet temperature gradually increases to the target of 350 ˚C, and after a certain level of irradiance is achieved, the compressor is released from the forced minimum speed control. In the evening, the plant shut-down is done by switching the compressor to the minimum speed of 40% until the SF outlet temperature drops under a specified temperature limit, and the compressor is turned off. This approach allows a shut down process in a controlled manner.

5.3.2 1-day simulations at different dates and results

The plant behavior was compared at three different dates having different clear sky irradiance conditions: 21st of February, 21st of April and 21st of June. Table 8 shows the monthly average Turbidity Linke factors and ambient temperatures applied for each case.

Table 8. The monthly average Turbidity Linke factors and ambient temperatures for three different dates.

Date	Average TL factor [-]	Average ambient temperature [ºC]
21st February	3.0	10
21st April	4.0	17
21st June	5.0	25

The main simulation results are shown in Figure 54 presenting the net power production in three simulated cases (bottom) under the clear sky irradiance conditions (effective DNI) (top). The results show that the maximum level of the usable effective DNI (top) is practically equal in the cases of June and April. The average TL factor used for each month attenuates the DNI most in the case of June, and the least in the case of February. However, the energy yield (bottom) is the lowest in February, 4.79 MWh, due to shorter duration of day and larger incidence angles. In June, the peak power production is achieved at solar noon, whereas in April, the production around the noon is more flat. The daily energy yield was 10.09 MWh in the case of June, and 10.08 MWh in the case of April. The net thermal efficiency achieved at the design point (21st of June at 12:00) was 0.21.

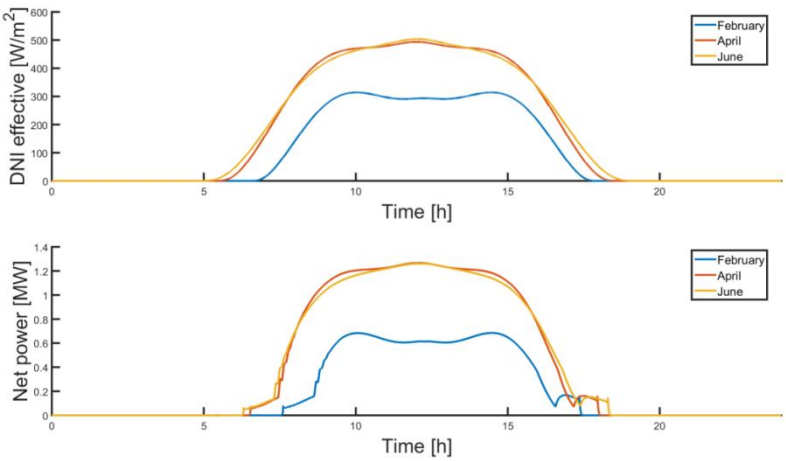

Figure 54. Net power production (bottom) during the days under different DNI (effective) conditions (top).

The control system applied gave satisfying performance with respect to the temperature set point of 350 ˚C as shown in Figure 55. Overshooting and temperature fluctuation can be observed only during the start-up sequence, when temperature temporarily exceeds 360 ˚C in each case (max temperature 363 ˚C in the case of April). After the minor fluctuation during the system start-up the temperature stays within ±2 ˚C of the set point during the normal day operation.

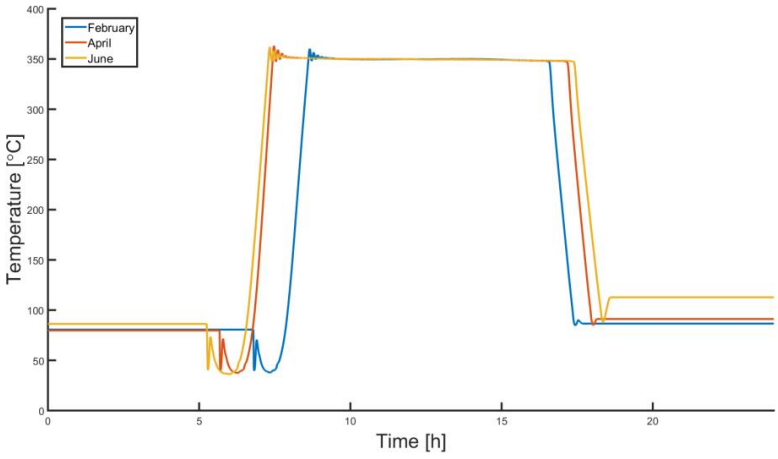

Figure 55. Solar field outlet temperature during the three simulated dates.

5.3.3 Simulation of irradiance disturbances and results

The system behaviour was studied under irradiance disturbances, which are typically caused by clouds. Meteorological clear sky conditions of 21st of June were assumed as initial state of the system. Four 1-day simulations were conducted, each undergoing a disturbance at different time of the day (Figure 56 shows all the disturbances at one figure for simplicity). Disturbances were caused by a step function, which first reduced the irradiance and then recovered it to the prevailing state of clear sky irradiance. The relative magnitude of the irradiance reduction was 20% of the prevailing DNI in each case, and the disturbance was caused for the whole solar field. The length of the disturbance was set to 10 min with a ramping time of 2 min. The disturbances were initiated at 09:00 (Cloud-9), 12:00 (Cloud-12), 15:00 (Cloud-15) and 17:00 (Cloud-17). The same control approach and control parameters as in 1-day simulations were used.

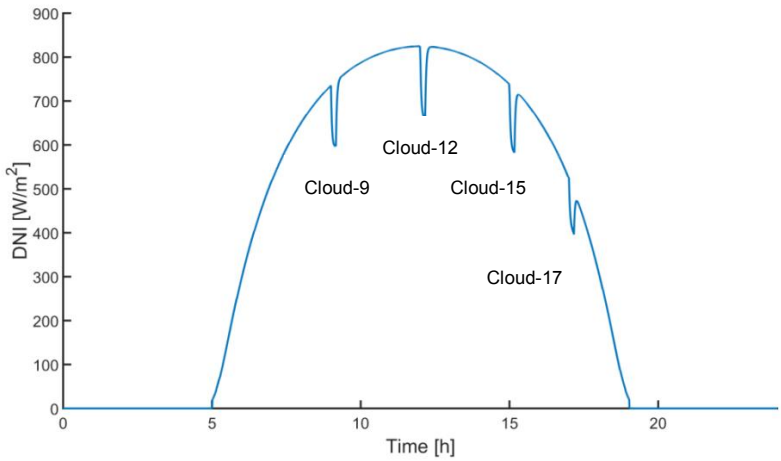

Figure 56. Four DNI disturbances of -20% performed for the whole solar field at different time instances.

Figure 57 shows example results of the four disturbances regarding turbine inlet and outlet temperature and pressure. In Cloud-9, Cloud-12 and Cloud-15, the turbine inlet temperature, i.e. the solar field outlet temperature, had very similar behaviour; it first dropped and then slightly fluctuated before returning to the target temperature after the disturbance. The maximum temperature deviation from the set point was 27 ˚C at the solar field outlet (above the set point in Cloud-9 and below in Cloud-12). However, it was noticed that the most fluctuation in the compressor rotational speed and consequently in the solar field outlet temperature appeared in the case of Cloud-15, in which the DNI level is decreasing. The turbine outlet temperature follows the trends of the inlet temperature. Due to the temperature drop and the mass flow control, also the pressure drops at the turbine inlet. The effect at the turbine outlet is minor. The figures also show the turbine inlet pressure change during the day as a function of the load, i.e. the prevailing

DNI level, and the outlet temperature change as a function of the turbine pressure ratio.

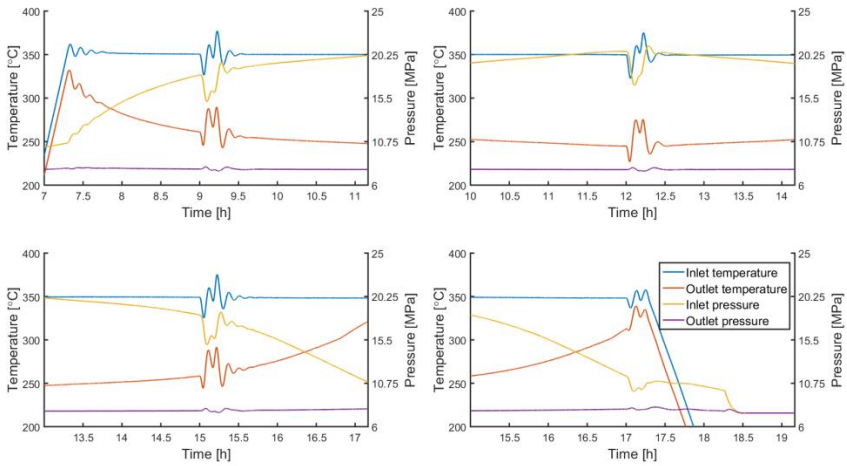

Figure 57. Turbine inlet and outlet temperature and pressure in four DNI disturbances: top left Cloud-9, top right Cloud-12, bottom left Cloud-15 and bottom right Cloud-17; in all figures, two hours before and after the disturbance initiation are shown.

In the case of Cloud-17, the DNI drop triggers the shut down sequence of the plant, since the DNI falls below a certain level. Thus, the compressor starts to run at the minimum load of 40% and the turbine inlet temperature does not recover to the target temperature of 350 ˚C. The temperature starts to fall, and the compressor shuts down. Thus, the plant is shut down a bit earlier than without the disturbance, but the difference is minor with respect to energy production.

The case simulations show that the one-phase flow of sCO_2 makes the temperature control easier than in the case of direct steam generation in the solar field. However, the results of disturbance cases reveal that the situations of sudden changes in the DNI, e.g. due to appearing clouds, require more attention on the control system in order to avoid harmful temperature gradients in the turbine. In the simulated disturbances, the maximum temperature gradient at the turbine inlet was in the range of 15 ˚C/min (Cloud-15). For detailed control system design and tuning, precise knowledge of the acceptable gradients to the turbine is needed. One challenge when using sCO_2 as working fluid is caused by operation near the critical point. If the temperature before compressor falls below this point, the compressor work might increase and there might be fluctuation in the compressor power due to rapidly changing fluid properties.

5.4 Comparison of line-focusing CSP concepts based on supercritical carbon dioxide

One option to improve the CSP plant efficiency and decrease the levelized cost of electricity from currently typically utilised parabolic trough solar field using thermal oil as HTF is to apply molten salt both as the HTF in the solar field and as the storage medium. Its use in line-focusing CSP applications has been demonstrated, for example, by Novatec Solar (currently FRENELL GmbH) in linear Fresnel solar field (FRENELL) and by Archimede Solar Energy in parabolic trough solar field (Maccari et al. 2015). When using molten salt as HTF, a storage system can be directly connected to the solar field. This approach decouples solar thermal energy production and power production and thus, provides dispatchable power generation. Other advantages of molten salts with respect to commonly used oils are (Kearney et al. 2003), (Boerema et al. 2012), (Morin et al. 2015):

- Temperature can be raised up to 585 ºC, thus increasing the Rankine cycle efficiency.
- Thermal energy storage (TES) size for a given capacity can be decreased.
- Higher concentration ratio of linear Fresnel collectors compared to parabolic trough collectors leads to lower heat loss for a given capacity.

Since the use of sCO_2 as working fluid has several advantages, but lacks the possibility for dispatchable power generation, a novel concept combining the benefits of sCO_2 and molten salt is studied. This concept combines the dispatchable nature of molten salt solar as HTF and storage medium and high efficiency of sCO_2 as the working fluid. Similar concept, which integrates molten salt storage system to solar field and power block both using sCO_2 is presented in (Ma & Turchi 2011).

This chapter presents the modelling approach of the novel concept, and its behaviour is compared with the direct-heated sCO_2 CSP concepts presented in Chapter 5.3. The two concepts are referred as:

1) Concept 1: sCO2 both as HTF and working fluid in closed Brayton cycle (direct-heated sCO2 CSP concept) (Chapter 5.3)
2) Concept 2: Similar power block to Concept 1, but molten salt as HTF and storage medium (indirect sCO2 CSP concept)

5.4.1 Modelling approach of the indirect sCO_2 CSP concept

The model development of the concept comprises modelling of several subsystems, namely linear Fresnel solar field, two-tank storage system, molten salt/sCO_2 heat exchanger, power block, control system, and fluid and material properties. The concept and its main components are illustrated in Figure 58. The solar field and two-tank storage system using molten salt are connected to the sCO_2 power cycle through an additional heat exchanger.

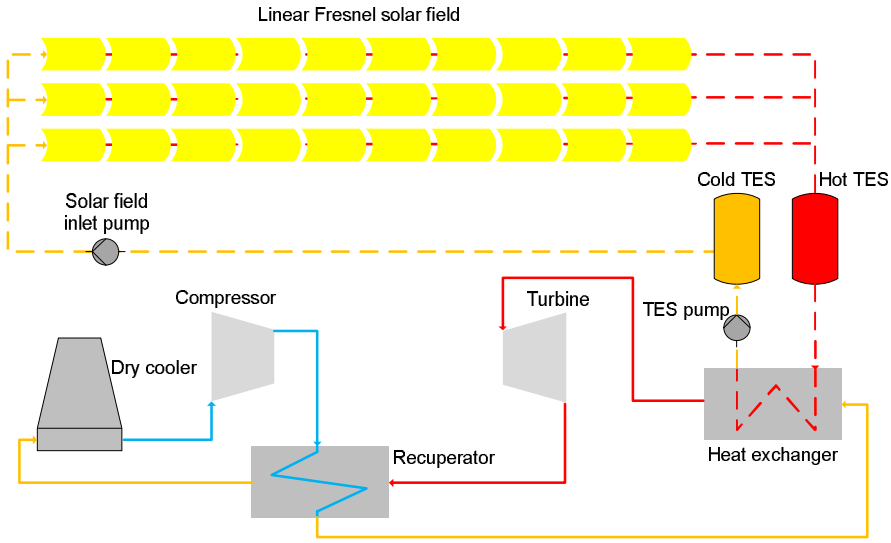

Figure 58. Schematic process diagram of indirect sCO_2 CSP concept, which uses molten salt as the HTF and storage medium, and sCO_2 Brayton cycle.

The concept is dimensioned so that comparable results to Concept 1 can be achieved. The dimensioning of the power block in both concepts aims at achieving equal net power of around 1 MW (see Eq. 12) under nominal conditions corresponding to 21st of June at 12:00 in Quarzazate, Morocco.

The solar field uses similar linear Fresnel collectors as in Concept 1. The number of collectors in one collector row was set to seven in Concept 1 and ten in Concept 2 in order to ensure reasonable mass flow rate in the collector rows. In Concept 1, three collector rows were set in parallel, whereas in Concept 2, the number was nine, respectively. The temperature control in the solar field is based on the pump rotation speed control. Control valves in the inlet of each collector row causes sufficient pressure drop for each row. The heat losses from the field piping to surroundings were modelled too.

Hot and cold TES are operated at 550˚C and 280˚C, respectively. Storage capacity is dimensioned so that continuous round-the-clock power production with nominal net output can be guaranteed. The freezing point of the used molten salt, Hitec, is 142˚C (Boerema et al. 2012), and freezing during the night is prevented by circulating salt from the cold TES through the solar field.

The inlet CO_2 parameters to turbine were set to 350 ˚C / 200 bar and outlet parameters to 250 ˚C / 78.3 bar at design point. After turbine, the waste heat is recovered to the CO_2 stream before its actual heating by solar energy. This recuperation is important for the cycle thermal efficiency, since the pressure ratio for sCO_2 Brayton cycle is low and the turbine outlet temperature high (Ahn et al. 2015). The fluid is cooled to its final temperature of 32 ˚C in a dry cooler before feeding to the compressor.

5.4.2 Results of the comparative simulation of two sCO_2 CSP concepts

The target concepts were simulated for one day, 21st of June (i.e. summer solstice) with the location of Quarzazate, Morocco (31.004 ˚N, 6.864 ˚W). The results of this first simulation case regarding overall system performance are shown in Figure 59 for Concept 1 and in Figure 60 for Concept 2. Figure 59 shows solar field thermal power (blue), net power (orange), turbine power (yellow), compressor power consumption calculated with Apros pump component (purple) and compressor power calculated as suggested in (Singh et al. 2011) (green). Figure 60 shows solar field thermal power (blue) and net power (orange) in the top figure, turbine power (blue), compressor power consumption (orange), and power consumption of molten salt pump (yellow) and heat exchanger pump (purple) in the mid figure, and heating power of the heat exchanger (blue) and cooling power of the air cooler (orange) in the bottom figure. Also solar field optical and thermal efficiency in Concept 1 under certain DNI (direct normal irradiance) conditions are shown in Figure 59.

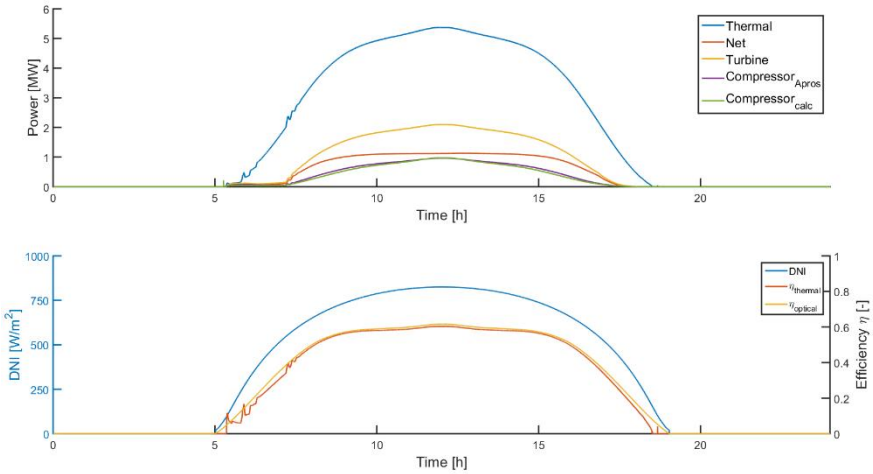

Figure 59. Power production and consumption of the subsystems of direct sCO_2 concept (top) and optical and thermal behaviour of the solar field (bottom).

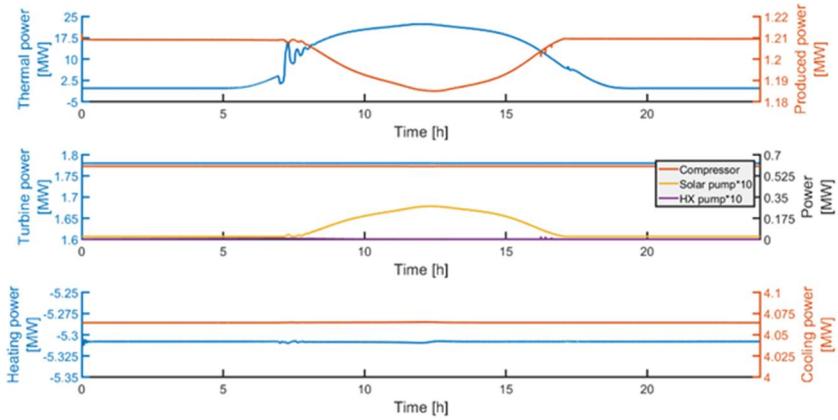

Figure 60. Power production and consumption of the subsystems of indirect sCO2 concept (top; solar field thermal power on the left axis) and optical and thermal behaviour of the solar field (bottom).

The overall results of Concept 1 show reasonable behaviour of the model and control system. The start-up procedure requires minor improvements to avoid temperature fluctuations. In the direct use of sCO_2 both as HTF and working fluid, the net power production follows the trend of the DNI level (Figure 59) and the production is directly dependent on DNI conditions. Studies on the effect of solar field temperature level on power cycle efficiency are needed in the future, in order to define the optimal temperature level and dimensioning of the solar field within the limits of the material properties.

The clear benefit of Concept 2 is the ability for continuous power production (Figure 60). However, this significantly increases the required solar field size with respect to Concept 1 and the related investment costs. From the investment point of view, reasonable dimensioning of the solar field and storage system is crucially important, and further attention must be paid to it. Compared to Concept 1, additional components needed in Concept 2 are the heat exchanger and the molten salt pump. The power demand of the compressor is constant throughout the day, but the demand of the molten salt pump follows the solar field load. Also the operation mode changes in Concept 2 require further consideration. For example, the pump dimensioning becomes important, when small mass flow rates are used during the night to prevent freezing of molten salt.

Compression work plays significant role in the net production achieved in the sCO_2 Brayton cycle. The Figure 59 shows the power consumption of compressor calculated by Apros Pump component and compressor performance model presented in (Singh et al. 2013), giving rather similar results. The comparative study of the two concepts shows that the solution combining the advantages of sCO_2 and molten salt fluids (Concept 2) is a promising approach in order to guarantee continuous power production from solar energy with high efficiency.

5.5 Central receiver solar field

An efficient computational model for solar central receiver systems, including heliostat field and the receiver system was developed in the COMBO-CFB project. The model can be used in conjunction with the dynamic process simulation program Apros. The presented model is composed of several individual component models, which can be considered separately from each other.

The presented solar power plant can be thought of consisting of three distinct components, which can be considered independent of each other: The collector, the receiver and the power conversion process. The collector and the receiver have been implemented as computational modules, which work along with Apros. Due to computational requirements, the collector model is implemented in high performance C-code running in separate process, whereas the receiver model is simple enough to run in real time within the Apros process. A fast discrete ray tracing approximation is used to model the heliostat field's optical behaviour. This model uses approximation to reduce computing time while maintaining good accuracy. The models are implemented as Apros components for convenient use within process simulations. Small section of a steam loop in Apros is presented as an example at this point.

5.5.1 Collector model

The chosen collector model is in large part based on a computational model described in (Noone et al. 2012). This model uses simplified ray tracing to produce good approximation of the result while reducing the computational requirements significantly. Regular Monte Carlo ray tracing is generally more accurate, but requires significantly more computational power due to larger number of rays that need to be traced. Selected model uses several approximations and assumptions to reduce the computational requirements enough to make the model efficient enough for use in cases where large number of simulations need to be run in varying operating conditions.

The implemented heliostat field model takes into consideration all the necessary losses including atmospheric losses, cosine loss, local atmospheric attenuation, reflectance, blocking and shading, and spill losses. Computationally it is more convenient to consider the losses by their respective efficiencies. The efficiencies are in order: atmospheric, cosine, attenuation, reflection, mirror blocking, mirror shading and spill efficiency. The heliostat field model computes only radiation flux at the receiver surface and only computes losses related to the field. Further heat losses happening at the receiver are handled by a receiver model running within the Apros simulation.

5.5.2 Receiver model

The receiver model is a fast correlation described in (Kim et al. 2015), which is based on CFD simulations of 72 different cases with varying wind conditions and receiver geometry. The model has been validated with multiple empirical data sets (Kim et al. 2015). It is able to model fully external receivers, i.e. planes or cylinders, as well as cavity receivers, which can be partial or full cavities.

The model takes as inputs receiver surface area A_{rec} (m^2), aperture area A_{ap} (m^2), receiver surface emissivity, wind velocity V (m/s), receiver temperature T_{rec} (°C) and ambient temperature T_{am} (°C). The type of receiver that the input is treated as, depends on the ratio between receiver surface area A_{rec} and receiver aperture area A_{ap}. This is the opening ratio *OR* described as the ratio of aperture area to receiver area.

While the model appears to be very widely applicable and accurate within a reasonable tolerance where validation data is available, situations may arise where the correlation cannot be applied. With this in mind, the receiver model has been implemented such that the user can easily implement new case specific correlations when the need arises. Such correlations could be derived from CFD models, as was described in (Kim et al. 2015), or from empirical data when available.

5.5.3 Apros model for the central receiver power plant

Part of the receiver model is implemented directly in Apros. The collector model is implemented as external code, which is run independently from Apros. The simulations running within Apros require much greater time resolution than what is practical with the ray traced collector model, so interpolation is used when computing values at each time instance. Depending on the number of computed ray tracing time steps, the user can choose between linear and polynomial interpolation. Linear interpolation is the simplest option and does not require additional user effort, but the results may be inaccurate between the interpolation points, as the path is not smoothed. Any residual noise resulting from the random sampling within the collector model is also preserved.

This polynomial interpolation is implemented as the solar collector component in Apros, and it only takes day and time as inputs. At the beginning of each simulation run, the component invokes the external ray tracing utility. If the model parameters have been changed, the utility then performs the given ray tracing case, and returns tabulated results. The component then fits the polynomial over the result data and creates a fast lookup cache that can be read during the simulation with practically no computational cost. If the model parameters were not changed since the previous run, old lookup table is reused. Figure 61 shows Apros diagram of the model including the solar field and receiver.

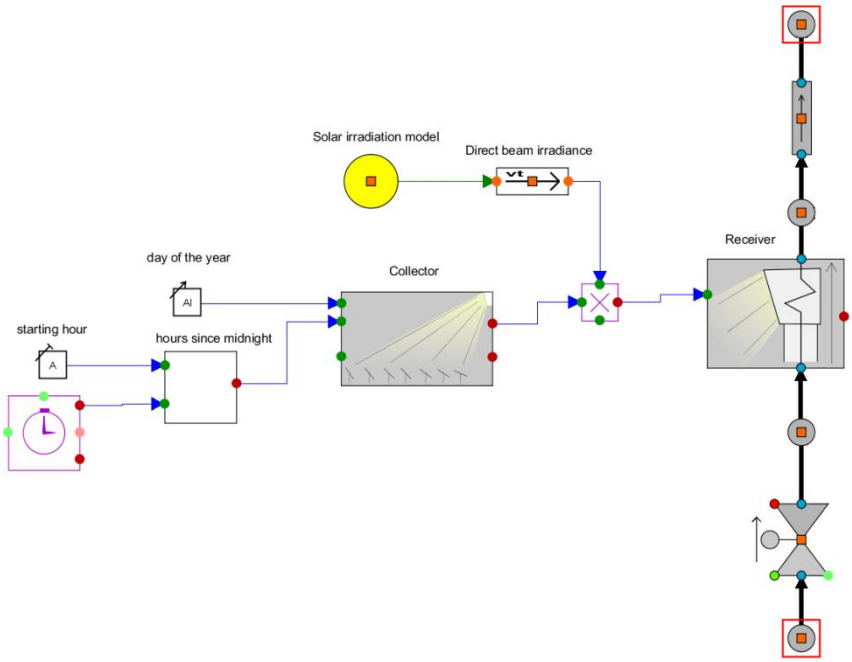

Figure 61. Apros diagram of the central receiver system. Collector acts as a wrapped for external computation. Receiver component contains another Apros model diagram, shown in Figure 62.

Since Apros can consider the incoming radiation as simple numerical data, in most cases the heat exchanger is represented by a pipe with a heating element. In Apros such component is called “heat pipe”. In Figure 62, this component is labeled “Heat exchanger”. The heating power of the heating element is continuously set to match the net irradiance at the solar tower receiver surface. This is done by passing power density value to the outer surface computation node of the heat pipe, which is represented by a cyan square labeled “Outer surface” in Figure 62. The appropriate power density is calculated by determining the effective heat transfer surface area of the heat pipe.

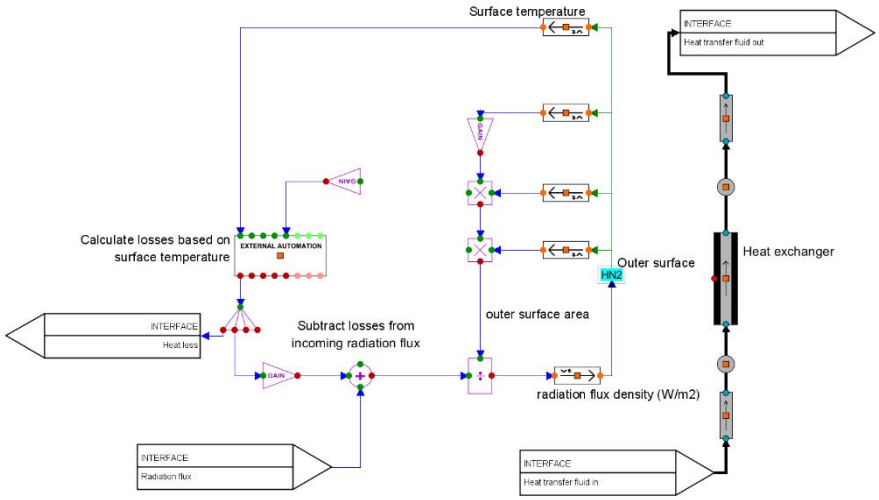

Figure 62. The receiver diagram in Apros.

Validating the entire central receiver model as a whole would require sufficiently complete set of experimental data with enough information about the field layout, operating conditions and incident radiation flux on the receiver. It proved challenging to find such comprehensive data set in literature, so each part of the model had to be verified independently from each other. The correctness of models for local atmospheric attenuation and receiver heat loss were verified with the data in the original papers. In the case of the collector model, a reasonably accurate way to verify correctness is to compare it with other similar program codes that are known to have high degree of physical accuracy. In this case the Soltrace code was used for comparison.

6. Virtual CSP hybrid concepts

A direct steam generating LFC solar field was integrated to a CFB steam power plant with different integration options (Chapter 6.1) to analyse and compare the benefits and challenges of integration. The LFC solar field with DSG was selected for hybridisation due to its cost reduction potential, low cleaning water and land use requirements and direct connectability of the two steam cycles (Peterseim et al. 2013). In addition, reference hybrid cases applying LFCs with DSG already exist. The studied concepts include:

1) Concept 1: Feedwater preheating by feeding solar steam to the bled off steam line (Chapter 6.2)
2) Concept 2: Feeding solar steam to the cold reheat line (Chapter 6.3)
3) Concept 3: Feeding solar steam to the high pressure turbine (Chapter 6.4).

The concepts were analysed to find the limiting factors for the maximum solar share, to study the effects of solar steam integration on the joint steam cycle and to define the main performance figures.

6.1 Subsystems of the hybrid concepts

The selected concepts represent both commercial concepts (Concept 1 and 2) and a concept foreseen to achieve maturity in the future (Concept 3) in the near future and in the longer time span. The feedwater preheating and cold reheat line process configurations, in which direct steam generating LFC solar field is integrated with a steam power plant (Peterseim et al. 2013), represent the commercial concepts. The configuration foreseen to be technically feasible in the future generates superheated solar steam in parallel with the steam boiler and integrates the solar steam to the joint HP turbine. The three configurations are depicted in Figure 63.

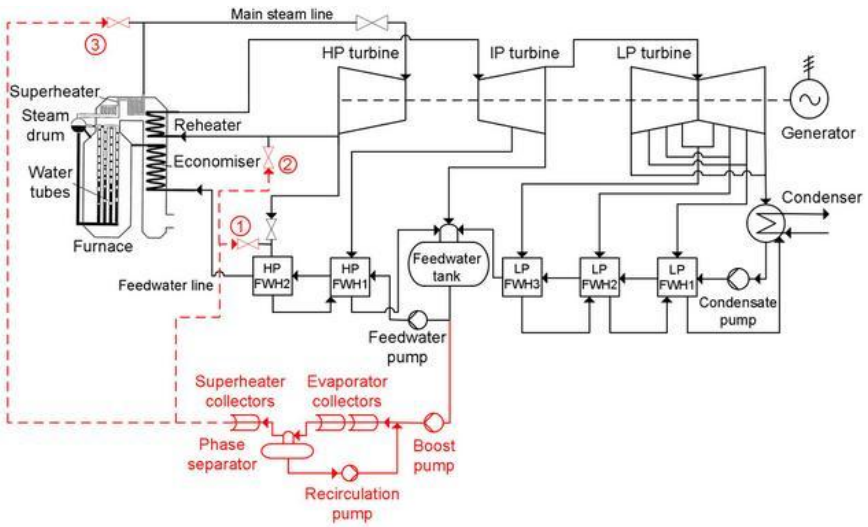

Figure 63. Three studied hybrid process configurations integrating the LFC solar field with DSG to the CFB steam power plant; 1) Feedwater preheating, 2) Cold reheat line, and 3) High pressure turbine.

According to Peterseim et al. (2014b), the solar field should generate steam parallel to the joint turbine rather than to the feedwater preheating or to the cold reheat line. As a consequence, the steam parameters of the LFC solar field should match with the live steam parameters of the steam boiler, which are around 540 °C and 160 bar for subcritical coal-fired units (Peterseim et al. 2013) and around 525 °C and 120 bar for biomass-fired units (Peterseim et al. 2014b). The LFC with DSG is capable of producing steam up to 520 °C (Zhu et al. 2014) and up to 106 bar (AREVA Solar 2011b). Thus, the solar field is suitable for parallel steam generation with biomass-fired units with lower live steam parameters than with coal-fired units. One of the state-of-the-art biomass boiler technologies is CFB boiler (Kettunen et al. 2014), which is the selected steam boiler technology for the hybrid configurations in the COMBO-CFB project.

6.1.1 Linear Fresnel solar field

The solar field model consists of LFC modules, which are presented more closely in Chapter 5.1. The solar field is oriented in North-South direction in the case studies. Geographical location of Ouarzazate, Morocco is used for the hybrid plant, and June 21st at 12.00 a.m. is used as the design point (Table 9).

Table 9. Site information of the hybrid system.

Location	Ouarzazate, Morocco
Latitude [°]	31.004
Longitude [°]	6.864
Average Linke Turbidity factor in June	5
Average direct normal irradiance (DNI) in June [W/m^2]	824.8
Average ambient temperature in June [°C]	26
Elevation from sea level [m]	1143

The number of collectors per row and the number of collector rows depend on the hybrid concept (Table 10). In the feedwater preheating (Concept 1) and cold reheat line (Concept 2) concepts, the collector row consists of 15 evaporator and 3 superheating collectors, as the design steam parameters are 40 bar and 360 °C. The maximum number of collector rows is 4 in Concept 1 and 15 in Concept 2. In high pressure turbine concept (Concept 3), the maximum number of collector rows is 10, and one collector row consists of 14 evaporator collectors and 7 superheating collectors. The steam parameters are the same as the live steam parameters of the steam boiler, 120 bar and 530 °C. One representative collector row of the solar field is modelled in detail for each concept, and the simulated outputs of the row are applied for the whole solar field accordingly.

Table 10. Main design parameters of the solar field in the Concepts 1−3.

Concept	Feedwater preheating (Concept 1)	Cold reheat line (Concept 2)	High pressure turbine (Concept 3)
Evaporator collectors per row	15	15	14
Superheating collectors per row	3	3	7
Total number of collectors per row	18	18	21
Maximum number of collector rows	4	15	10
Length of the solar field (m)	806.4	806.4	940.8
Steam pressure (bar)	40	40	120
Steam temperature (°C)	360	360	530
Steam mass flow per collector row (kg/s)	1.85	1.85	1.9
Feedwater inlet pressure (bar)	10.3	10.3	10.3
Feedwater inlet temperature (°C)	151.2	151.2	151.2

Feedwater for the solar field can be extracted from any point of the steam power plant's feedwater line. Depending on the feedwater pressure, an additional pump or pressure reduction station is needed at the inlet of the solar field to adapt the pressure to a suitable level. Larger solar share is achieved if feedwater is extracted at lower temperature and the feedwater preheating is conducted in the solar field instead of the feedwater preheaters. In all the concepts, feedwater to the solar field is extracted after the deaerator in order to maximize the solar share and to minimize the preheating section of the solar field. The solar field feedwater temperature and pressure are 151.2°C and 10.3 bar.

6.1.2 CFB power plant

The CFB power plant is a subcritical unit, which power cycle is a regenerative and reheated Rankine cycle. The steam boiler is a natural circulation boiler with steam drum, and the unit is a condensing power plant, which produces only electricity. The electrical power output, thermal power and fuel power of the unit are 120.0 MW_e, 315.1 MW_{th}, and 341.5 MW, respectively, on 100% load (Table 11). The design steam parameters are 120 bar/530 °C/530 °C and thermal and net efficiencies ($\eta_{thermal}$ and η_{net}) are 38.1% and 35.1%, respectively. The amount of combusted fuel is 23.2 kg/s and the CO_2 emissions 1,019 g/kWh on 100% load.

Table 11. Main design parameters of the steam power plant on 100% load without the solar field.

Design parameter	Value	Unit
Electrical power output	120.0	MW_e
Thermal power	315.1	MW_{th}
Fuel power	341.5	MW
Thermal efficiency ($\eta_{thermal}$)	38.1	%
Net efficiency (η_{net})	35.1	%
Fuel supply	23.2	kg/s
CO_2 emissions	1,019	g/kWh
Live steam pressure	120	bar
Live steam temperature	530	°C
Live steam mass flow	103.3	kg/s
Reheated steam temperature	530.0	°C
Reheated steam pressure	32.6	bar
Reheated steam mass flow	101.7	kg/s
Steam mass flow to the highest pressure FWH	7.0	kg/s
Condenser pressure	0.15	bar
Temperature of feedwater before economiser	237.1	°C
Approach temperature difference between economiser and steam drum	13.3	°C
Mass fraction of steam at the end of evaporator	0.15	-
Oxygen level in flue gas	3.5	%
Furnace pressure	1.01	bar
Final temperature of flue gas before stack	163.2	°C

The turbine island consists of one HP, two IP and four LP turbine sections, condenser and feedwater preheating system (Figure 64). The nominal inlet mass flow and pressure levels of the turbines are designed according to 110% load of steam boiler without the solar field. The isentropic efficiencies of the turbine sections decrease linearly from HP turbine section to the last LP turbine section from 95% to 83%. The feedwater preheating consists of three low pressure feedwater preheaters (LP FWH), a deaerator and two high pressure feedwater preheaters (HP FWH). The bled off steam for the HP FWH2 is extracted after the HP turbine. In the FWHs, the feedwater is preheated approximately from 45 °C to 240 °C.

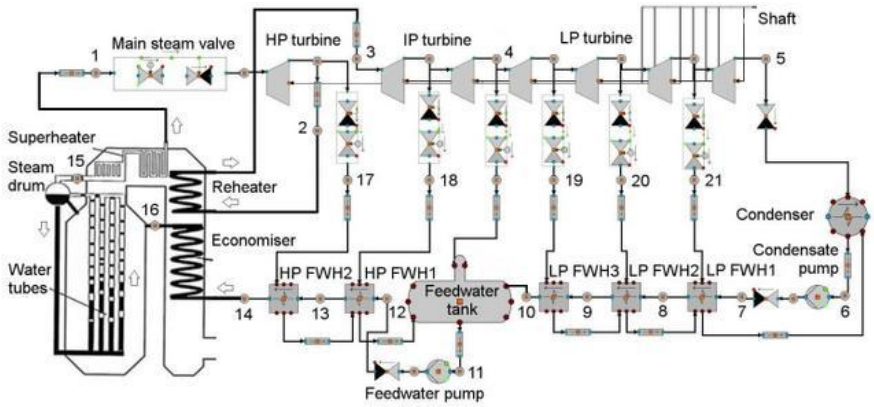

Figure 64. Schematic Apros process model diagram of the turbine island with state points shown in Table 15 (Appendix B).

The steam boiler model is divided into the flue gas side and water side of the boiler (Figure 65). The flue gas side consists of a CFB boiler module, fuel and combustion air supply systems and heat surfaces of the steam boiler, whereas the water-side consists of the steam drum and heat structures of the water wall in the furnace. Fuel is combusted in the boiler module with excess air, of which 70% is primary air and 30% secondary air. The heat of chemical reactions is transferred from the CFB module to heat pipe sections of the water tubes and the mass fraction of steam is designed to be 0.15 at the end of water tubes. The heat surfaces of the boiler include primary (SH 1), secondary (SH 2) and tertiary superheaters (SH 3), primary and secondary reheaters (RH 1 and RH 2), two economiser surfaces and two parallel air preheating surfaces (LUVO): one for primary air and one for secondary air. The superheaters include two injection flow lines and reheater one injection flow line, located between the heat surfaces. The spray water is extracted after the feedwater pump, and the total amount of spray water to the superheaters is 8.1 kg/s and to the reheaters 5.4 kg/s on 100% load (Table 11). The heat surfaces are designed to cool down the flue gas close to 160 °C, to achieve the design values of live steam and reheated steam temperatures still on 70% load of the steam boiler and to maintain the approach temperature difference between the economiser and the steam drum at 15 °C on 100% load.

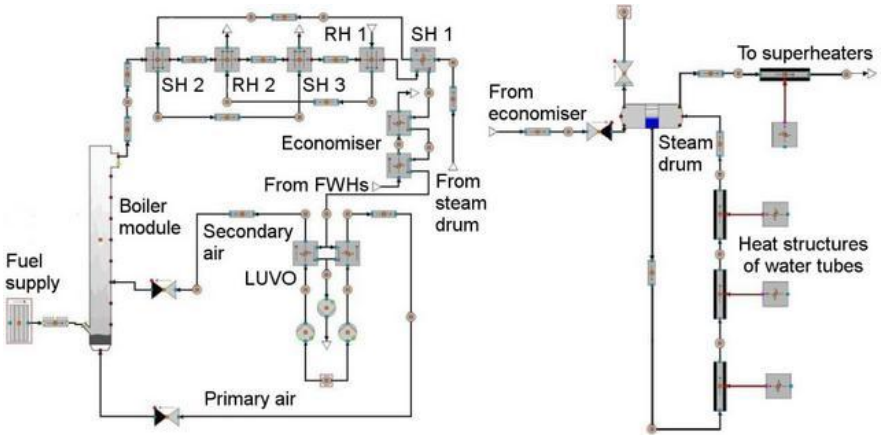

Figure 65. Schematic Apros process model diagrams of the flue gas side (left) and water side (right) of the steam boiler.

The main objectives of the control system are to produce desired power output of the boiler and the turbines and desired live steam pressure and live steam and reheated steam temperatures. The steam power plant is controlled with six main control loops using PI controllers. The control loops are:

1. Live steam pressure control, in which steam pressure before the main steam valve is controlled by adjusting the fuel supply.
2. Combustion air control, in which fuel and secondary air supplies are connected in cascade mode and oxygen content of the flue gas after the furnace is monitored. The fuel supply defines a set point for the air supply, which is adjusted according to oxygen content.
3. Power output control, in which electrical power output is controlled by adjusting the steam mass flow with the main steam valve placed before the HP turbine.
4. Live steam and reheated steam temperature controls, in which temperatures before and after the heat surfaces are measured, and spray water mass flow is adjusted accordingly.
5. Feedwater mass flow control, in which liquid level of the steam drum, and flow rate of feedwater and generated steam are monitored. The liquid level of the steam drum is kept constant by adjusting the feedwater pump speed.
6. HP FWH, LP FWH and condenser level controls, in which the liquid level inside the condensing heat surface is kept constant by adjusting the outlet flow rate with a control valve.

The operation strategy of the steam boiler is boiler follow mode, in which the live steam pressure before the main steam valve is kept constant at 120 bar by adjusting the fuel supply of the steam boiler. The electrical power output is controlled by adjusting the steam mass flow with the main steam valve before the HP turbine (Figure 66). When solar steam is integrated to the plant, the boiler and the turbines are operated on fuel saving mode. Thus, the more solar steam is added, the more the fuel supply is decreased. The electrical power output is kept constant at 120 MW_e.

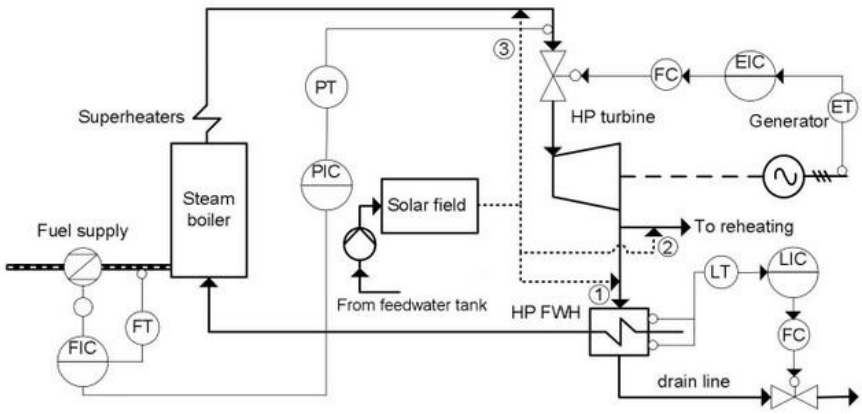

Figure 66. The main control loops of the Concepts 1–3 (ET = electric transmitter, EIC = electric indication and control, FC = flow control, FT = flow transmitter, FIC = flow indication and control, LT = level transmitter, LIC = level indication and control, PT = pressure transmitter, PIC = pressure indication and control).

During the solar field start-up and shutdown, solar steam is fed into the condenser if the steam is not superheated adequately. In feedwater preheating and cold reheat line concepts, the temperature limit is 280 °C, which is 30 °C over the saturation temperature. In high pressure turbine concept, the temperature limit is 450 °C, which is 130 °C over the saturation temperature.

6.2 Feedwater preheating concept

In the feedwater preheating concept (Concept 1), the HP FWH2 before economiser is fully replaced with solar steam. The superheated solar steam replaces bled off steam extracted after the HP turbine section, which is normally used for feedwater preheating. Thus, the saved bled off steam continues to expand in the IP and LP turbine sections generating more electricity. The design steam pressure and temperature of the solar field are 40 bar and 360 °C (Figure 67), which are achieved within the first 10 minutes of the solar field start-up. The steam parameters are kept constant during the daily operation. After the solar field shutdown, the solar steam pressure gradually decreases from 40 bar to 0.7 bar and the steam temperature from 360 °C to 45 °C.

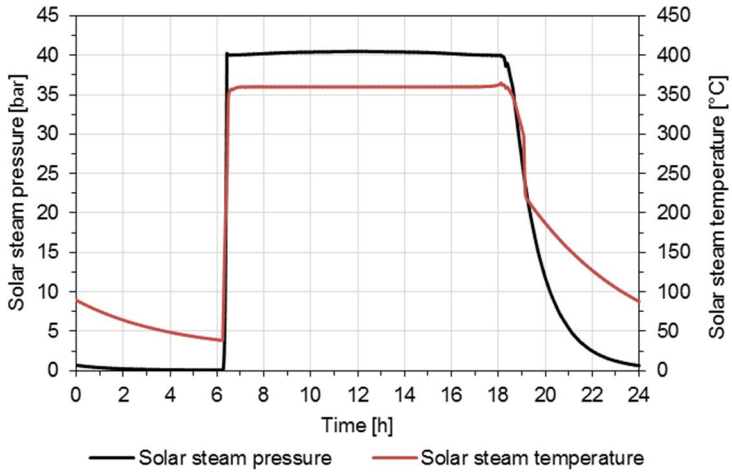

Figure 67. Solar steam pressure and temperature in Concept 1.

In Concept 1, the solar field consists of 4 collector rows, and the maximum steam mass flow to the HP FWH2 is 7.5 kg/s at noon on June 21st (Figure 68). During the start-up, some solar steam is fed to the condenser as long as the solar steam temperature is below 280 °C. As a result, the peak steam mass flow from the solar field to the condenser is 0.5 kg/s during the start-up.

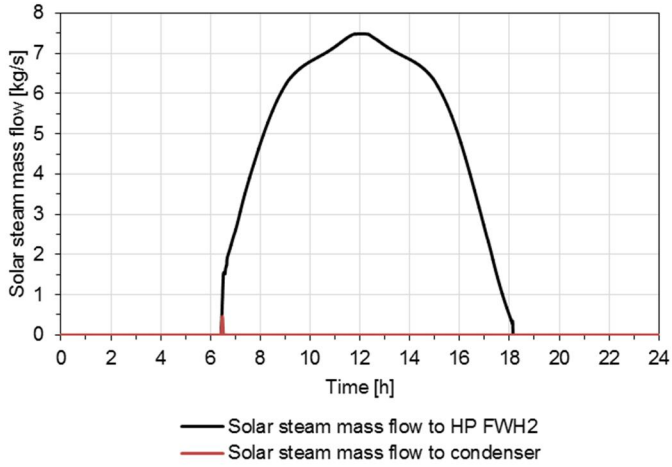

Figure 68. Solar steam mass flow to the HP FWH2 and to the condenser in Concept 1.

6.2.1 Interdependencies of subsystems

The subsystems of the hybrid power plant have multiple interdependencies. The more solar steam is fed to the system, the more operation of the shared components is affected. In Concept 1, the limiting factor for the maximum solar share is the condensing capacity of the HP FWH2. The more solar steam is fed, the less bled off steam is extracted after the HP turbine to the HP FWH2 (Figure 69). During the sunshine peak hours, the bled off steam is fully replaced by solar steam. If a fifth collector row would be added to the system, the total steam mass flow entering the HP FWH2 would exceed the condensing capacity of the HP FWH2, and lead to the dumping of excess solar energy.

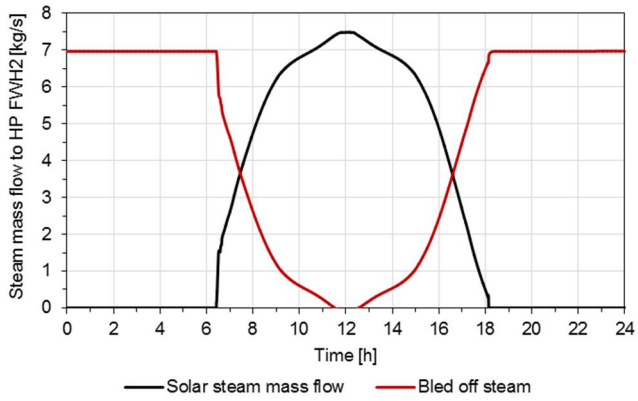

Figure 69. Condensing capacity of the replaced feedwater preheater (HP FWH2) is the limiting factor for the amount of integrated solar steam in Concept 1.

As a result of solar steam integration, the saved bled off steam increases steam mass flow to the reheating and to the IP turbine (Figure 70). Since more steam is expanded in the IP and LP turbine sections and electric power is kept constant, the steam mass flow to the HP turbine is decreased. With the maximum solar share, the steam mass flow to the IP turbine is increased by 2.5% from 101.6 kg/s to 104.1 kg/s, and the steam mass flow to the HP turbine is decreased by 3.1% from 103.3 kg/s to 100.1 kg/s. Thus, the different turbine sections are slightly imbalanced especially during the sunshine peak hours.

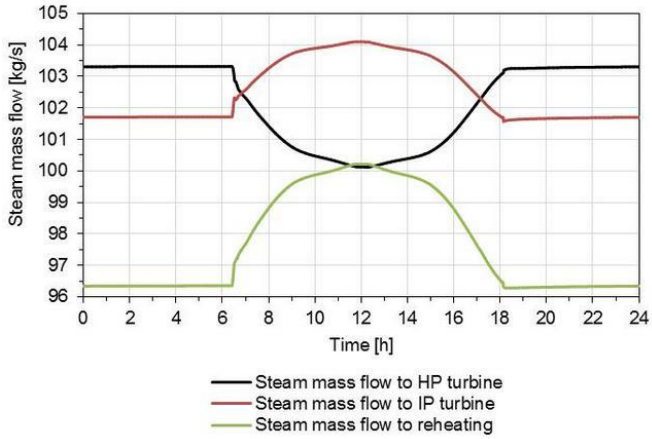

Figure 70. Effect of solar integration on steam mass flows to HP and IP turbine sections in Concept 1.

As the steam mass flow to the IP turbine increases, the discharge temperature and pressure of the HP turbine increases (Figure 71). As a consequence, the bled off steam temperature and pressure to HP FWH2 also increase. During the sunshine peak hours, the bled off steam temperature increases by 4.5 °C from 349.7 °C to 354.2 °C and the bled off steam pressure increases by 2.5 bar from 33.0 bar to 35.5 bar, which is the same as the discharge steam pressure. During the solar field start-up, temperature of the solar steam led to the HP FWH2 is between 280 °C and 360 °C and consequently, the bled off steam temperature decreases from 349.7 °C to 344.8 °C during the start-up.

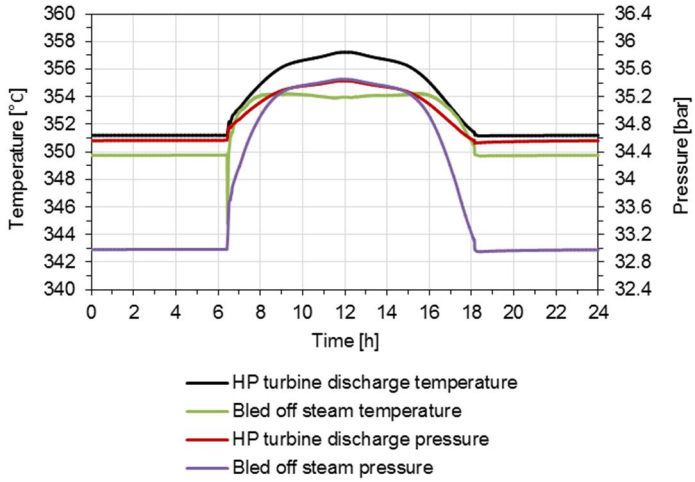

Figure 71. Effect of solar integration on the HP turbine discharge temperature and pressure and on the bled off steam temperature and pressure in Concept 1.

As the bled off steam parameters increase, the feedwater temperature before the economiser increases (Figure 72). Typically, the approach temperature difference is close to 15 °C, and the lower load of the steam boiler results in larger approach temperature difference between the economiser and the steam drum. The smaller the approach temperature difference is the less fuel is needed to evaporate the feedwater. Due to increased feedwater temperature before the economiser, the approach temperature difference is kept almost constant even though the steam boiler is operated on lower load. Thus, the solar integration improves the boiler efficiency.

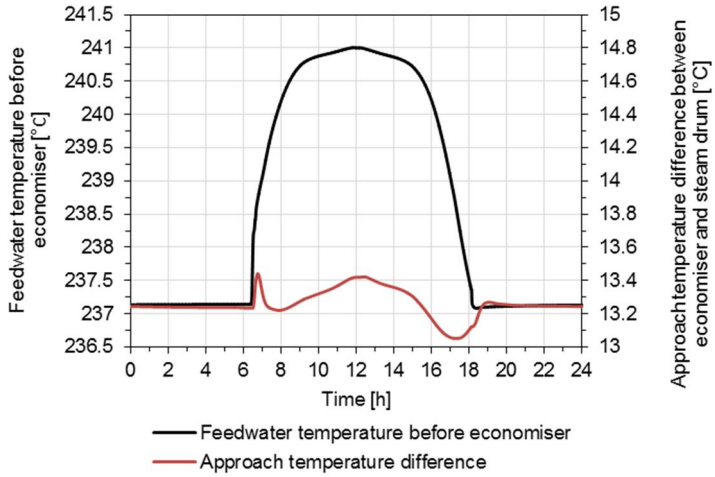

Figure 72. Effect of solar integration on feedwater temperature and approach temperature difference in Concept 1.

The increased feedwater temperature and the almost constant approach temperature difference affect the flue gas temperature after air preheating (Figure 73). Typically, the flue gas temperature decreases when the boiler load is decreased. However, the flue gas temperature after air preheating is kept almost constant due to the solar integration, even though the boiler load is decreased by 4.6% from 100% to 95.4%.

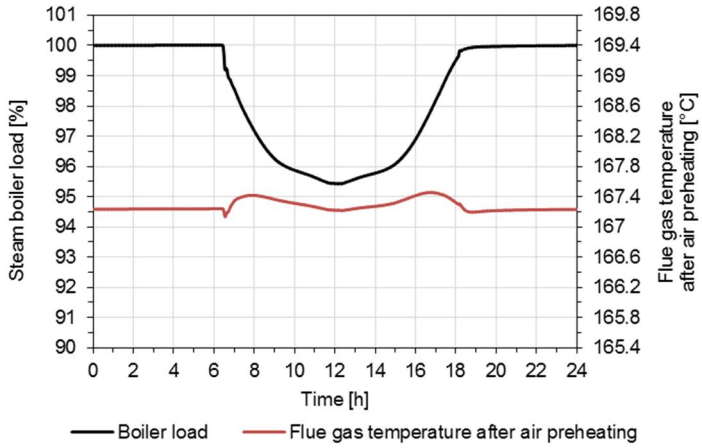

Figure 73. Effect of solar integration on boiler load and on flue gas temperature after air preheating in Concept 1.

The solar integration affects also the operation of steam boiler's heat surfaces. The injection flows of superheater and reheater are decreased, as the steam boiler is operated on lower load (Figure 74). The required reheating power increases due to the increased steam mass flow to the reheating. Thus, the reheater injection mass flow decreases relatively more than the superheater injection flow and the heat surfaces are in imbalance. The superheater injection flow decreases by 18.9% from 8.1 kg/s to 6.6 kg/s and the reheater injection flow decreases by 27.7% from 5.4 kg/s to 3.9 kg/s, as the peak load of the solar field is achieved. The steam temperatures are kept constant at 530 °C during the start-up and shutdown of the solar field.

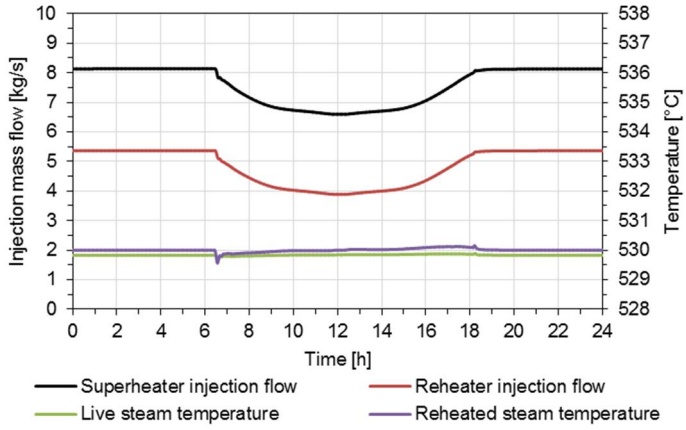

Figure 74. Effect of solar integration on live steam and reheated steam temperatures in Concept 1.

The increased steam mass flow to the IP turbine section results in increased water fraction of the exhaust steam and increased condensing power (Figure 75). With the maximum solar share, the condensing power increases by 2.4% from 185.0 MW_{th} to 189.4 MW_{th}. During the solar field start-up, solar steam is fed to the condenser instead of the bled off steam line. Thus, the condensing power increases rapidly in the morning from 185.0 MW_{th} to 187.2 MW_{th}. Water consumption of the condenser increases according the increasing condensing power. For water scarce regions, the water consumption is one of the limiting factors while using wet-dry or wet cooling methods.

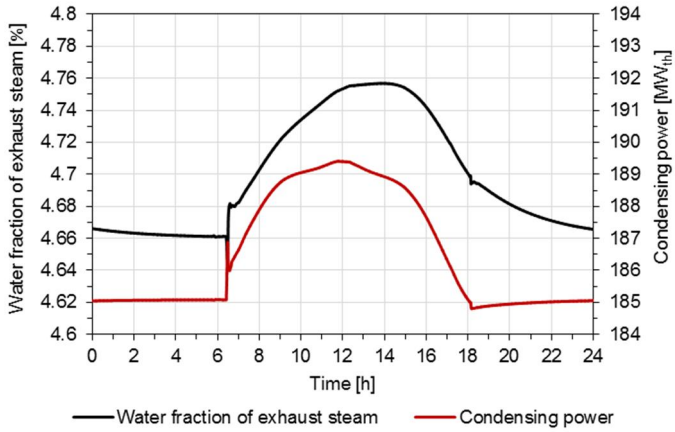

Figure 75. Effect of solar integration on the water fraction of exhaust steam and on the required condensing power in Concept 1.

To summarise, the main interdependencies of subsystems in Concept 1 include:

- Condensing capacity of the HP FWH2 (limiting factor for the solar share);
- Small imbalance of different turbine sections and heat surfaces;
- Increased feedwater temperature before the economiser and almost constant approach temperature difference;
- Increased condensing power and water consumption of the condenser.

6.2.2 Performance figures

In Concept 1, the maximum thermal power of the solar field is 16.8 MW_{th} at noon on June 21st at Ouarzazate Morocco (Figure 76). Despite of the solar integration, the power output of the hybrid system is kept constant at 120 MW_e when operated on the fuel saving mode. During the solar field start-up and shutdown, some minor variations occur in the power output of the hybrid.

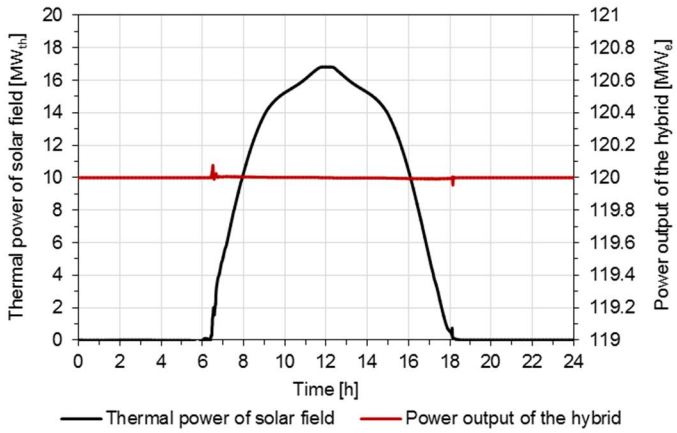

Figure 76. Effect of solar integration on the power output of the hybrid in Concept 1.

As the thermal power of the solar field increases, the fuel power and thermal power of the steam boiler decreases (Figure 77). With the maximum thermal power of the solar field, the fuel power is decreased by 4.6% from 341.5 MW to 326.0 MW and the thermal power of the steam boiler is decreased by 5.1% from 315.2 MW$_{th}$ to 299.2 MW$_{th}$. Thus, the thermal power decreases more than the fuel power. As a result, the total energy input (thermal + fuel) is 342.8 MW, which is 0.4% more than the initial fuel power of the steam boiler. The total thermal energy input (thermal + thermal) is 316.1 MW$_{th}$, which is 0.3% more than the initial thermal power of the steam boiler.

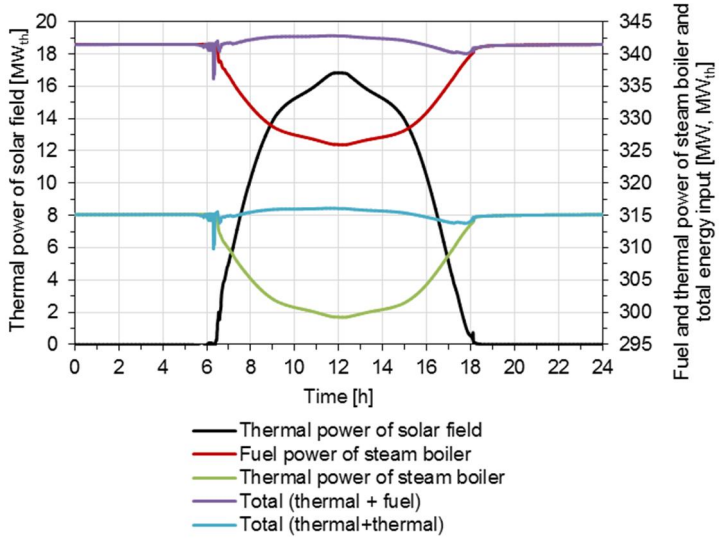

Figure 77. Effect of solar integration on the thermal power and fuel power of the steam boiler in Concept 1.

As the total energy input increases compared to the initial fuel power and thermal power of the steam boiler, and the power output of the hybrid is kept constant, the efficiencies of the hybrid system are decreased (Figure 78). With the maximum solar share, the thermal efficiency is decreased by 0.1 percentage points from 38.1% to 38.0%, and the net efficiency is decreased by 0.1 percentage points from 35.1% to 35.0%. The decreased efficiencies are caused by the increased steam mass flow through IP and LP turbine sections, which have lower isentropic efficiencies than the HP turbine section.

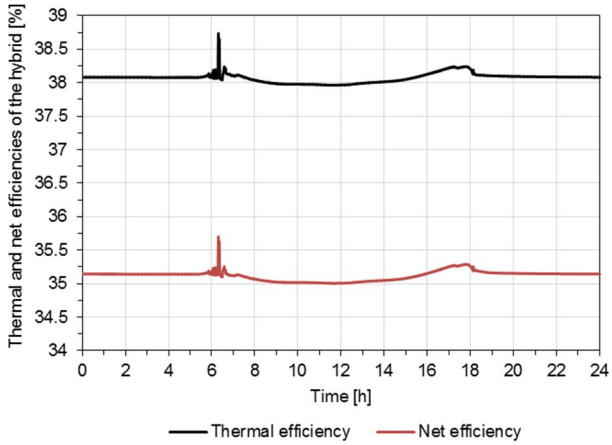

Figure 78. Thermal and net efficiencies of the hybrid system in Concept 1.

During the sunshine peak hours, the maximum thermal solar share is 5.3% and the maximum net solar share is 4.9% (Figure 79). However, the maximum achieved fuel and CO_2 emission savings are 4.6%. The achieved fuel and CO_2 emission savings are lower than the reached solar shares due to the decreased efficiencies of the hybrid system.

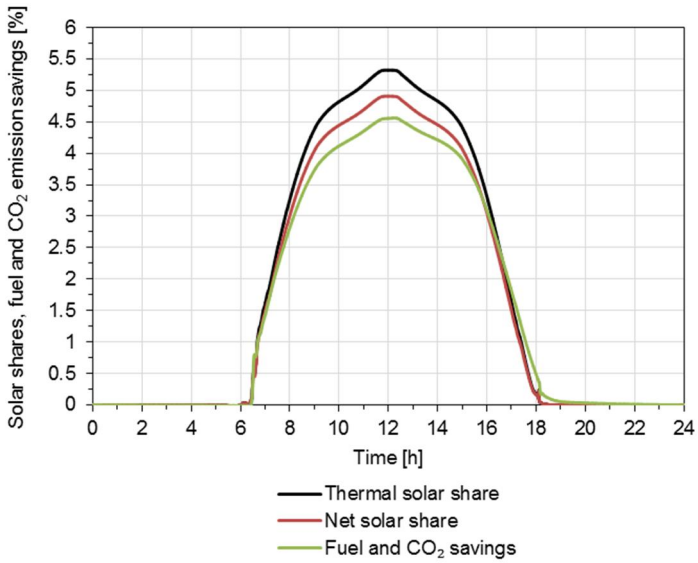

Figure 79. Maximum thermal and net solar shares and achieved fuel and CO_2 emission savings in Concept 1.

As a conclusion of the performance of Concept 1, the operation of the hybrid is steady during the start-up and shutdown of the solar field and during a clear day. However, the achieved fuel and CO_2 emission reductions of 4.6% are not enough compared to emission reduction targets (Figure 2). Higher savings could be achieved by optimising the efficiency of the hybrid according to the process configuration. Thus, the isentropic efficiency of IP and LP turbine sections should be higher than the HP turbine section's. In addition, higher savings can be achieved by replacing multiple feedwater preheaters by the solar field. However, the replacement of multiple feedwater preheaters is especially problematic for the design of the last LP turbine sections. Typically, the steam mass flow through turbine sections is decreased from the HP turbine section to the last LP turbine section due to extraction of bled off steams. The steam mass flow decreases less in the case of replacement of multiple bled off steam lines with solar steam. Thus, the load of the last LP turbine section would vary significantly over 24 hours.

6.2.3 Operation under transient solar irradiation conditions

A large step change test in irradiance from 100% to 30% was conducted to study the capability of the steam boiler to compensate rapid and large changes in irradiance. For the first 10 minutes, the hybrid is operated on steady-state with peak solar share (Figure 80). Then, a relative decrease in DNI of 50%/min from 824.8 W/m^2 to 247.3 W/m^2 is introduced for the whole solar field. The maximum gradient of fuel supply is limited to 7% of MCR/30s, which is the same load change rate than in the pilot-scale CFB combustion tests (Chapter 3.2). The max-

imum amount of fuel supply is set to 110% of the nominal supply. After the step change, the solar steam mass flow decreases by 5.5 kg/s from 7.4 kg/s to 1.9 kg/s within 5 minutes.

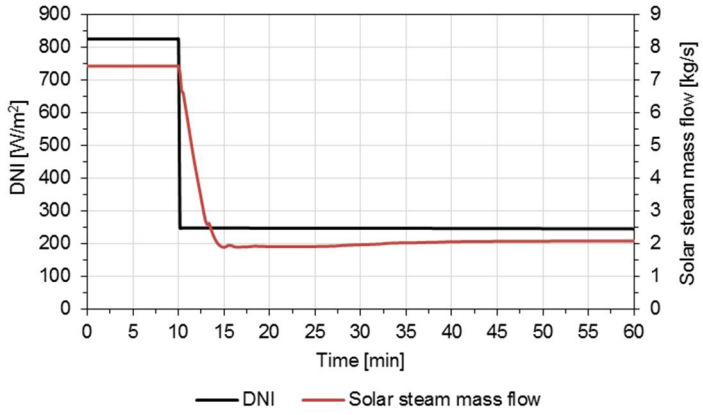

Figure 80. Effect of 70% DNI step change on solar steam mass flow in Concept 1.

As the solar steam mass flow decreases, the bled off steam mass flow after the HP turbine increases from 0 kg/s to 5.2 kg/s within 7 minutes after the step change (Figure 81). As more bled off steam is extracted to the HP FWH2, the steam mass flows to the IP turbine and to the reheating decreases. Consequently, the steam mass flow to the HP turbine is increased from 100.1 kg/s to 102.4 kg/s to maintain the electric power, since less steam is expanded in the IP and LP turbine sections.

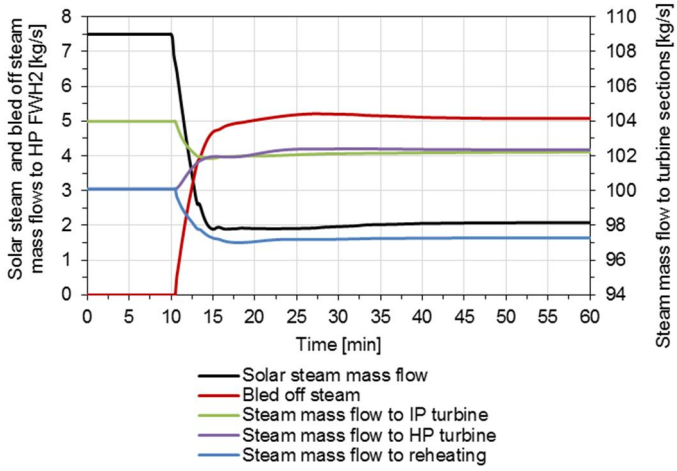

Figure 81. Effect of decreasing solar steam mass flow on other steam mass flows in Concept 1.

Due to the step change and increased boiler load, the live steam and reheated steam temperatures would increase if the injection mass flows are not increased. The live steam temperature increases from 530.0 °C to 530.6 °C within 8 minutes, as the superheater injection mass flow is increased from 6.6 kg/s to 7.9 kg/s (Figure 82). The reheated steam temperature increases from 530.0 °C to 531.8 °C within 6 minutes, as the reheater injection mass flow is increased from 3.9 kg/s to 5.0 kg/s. As a result, the maximum temperature gradient of the reheated steam is 0.3 °C/min, which is below the allowed maximum temperature gradient for turbines (approximately 5 °C/min).

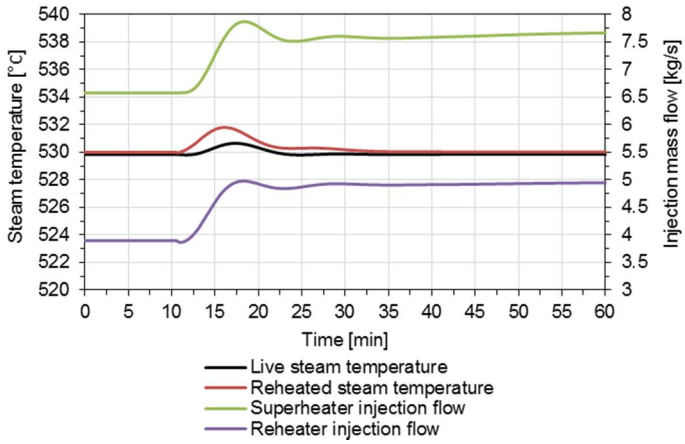

Figure 82. Effect of 70% step change on live steam and reheated steam temperatures in Concept 1.

Due to the step change and its effects on steam mass flows, the power output of the hybrid decreases by 0.35 MW_e from 120.0 MW_e to 119.65 MW_e in 2 minutes (Figure 83). Thus, the maximum power output gradient is 0.15% of MCR/min. As the power output decreases, more steam is fed to the HP turbine section and the steam boiler load is increased. Due to increased injection mass flows of the steam boiler, the power output and live steam mass flow slightly fluctuate before stabilisation.

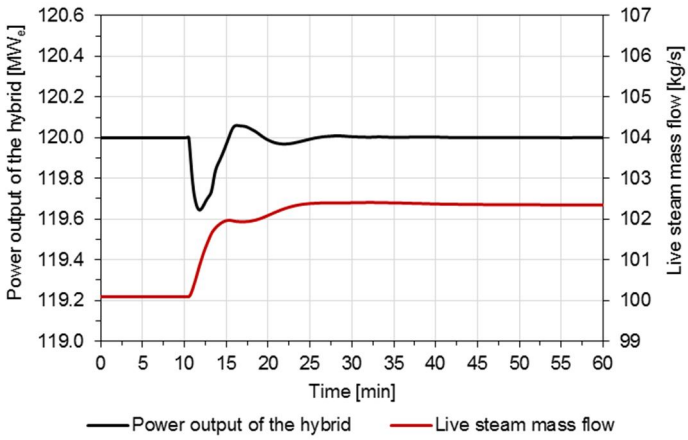

Figure 83. Effect of 70% step change on power output of the hybrid and on live steam mass flow in Concept 1.

The live steam mass flow is increased by opening the main steam valve before the HP turbine section. As a result, the live steam pressure before the main steam valve decreases from 120.0 bar to 119.34 bar within 5 minutes after the step change (Figure 84). To maintain constant live steam pressure the fuel mass flow is increased by 0.13 kg/min from 22.1 kg/s to 22.9 kg/s within 6 minutes after the step change.

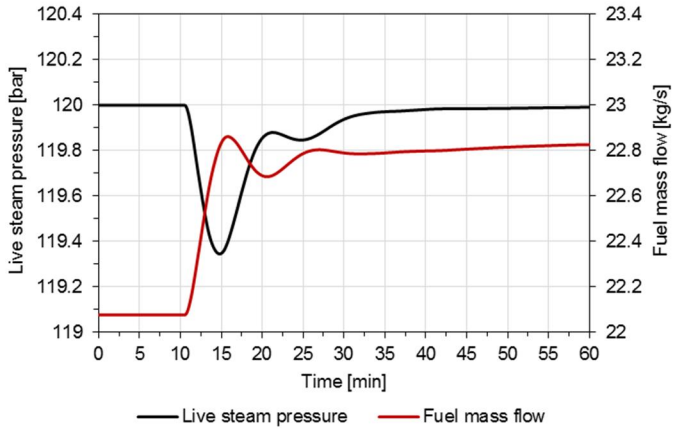

Figure 84. Effect of 70% step change on live steam pressure and fuel mass flow in Concept 1.

As a conclusion of the transient case in Concept 1, the effects of large step change are minor on the main operation parameters of the hybrid system. By developing the controls of the hybrid plant and integrating DNI forecasting into the model, the variations in solar steam production could be foreseen and compen-

sated better than with the simple PI controllers applied in the model. As a result of the study, the feedwater preheating concept can be considered as a technically feasible concept.

6.3 Cold reheat line concept

In the cold reheat line concept (Concept 2), the superheated solar steam is fed to the steam line after the HP turbine section. Thus, the solar steam enters the reheater of the steam boiler and expands in the IP and LP turbine sections generating more electricity. The design steam pressure and temperature of the solar field are the same as in Concept 1, 40 bar and 360 °C (Figure 85), which are achieved within the first 10 minutes of the solar field start-up. The steam parameters are kept constant during the daily operation. After the solar field shutdown, the solar steam pressure gradually decreases from 40 bar to 0.7 bar and the steam temperature from 360 °C to 45 °C.

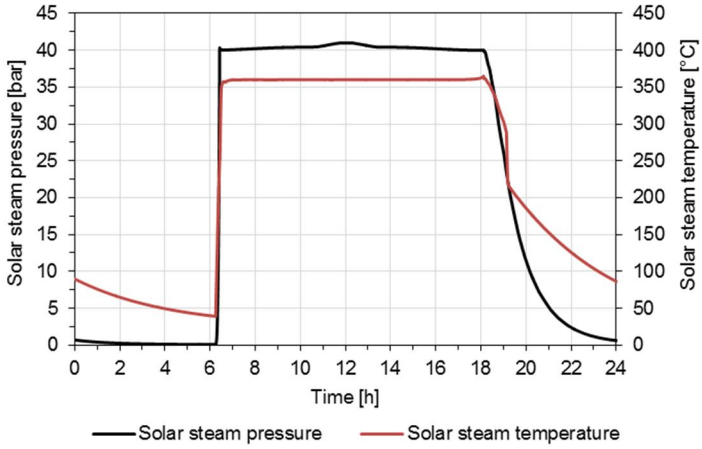

Figure 85. Solar steam temperature and pressure in Concept 2.

In Concept 2, the solar field consists of 15 collector rows, and the maximum solar steam mass flow to the cold reheat line is 28.1 kg/s at noon on June 21st (Figure 86). During the start-up of the solar field, some solar steam is fed to the condenser as long as the solar steam temperature is below 280 °C. As a result, the peak steam mass flow to the condenser is 1.9 kg/s during the start-up.

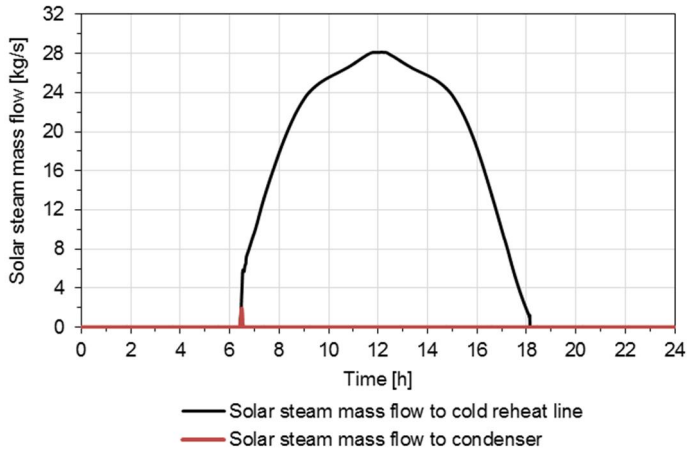

Figure 86. Solar steam mass flow to the cold reheat line and to the condenser in Concept 2.

6.3.1 Interdependencies of subsystems

The interdependencies of subsystems are rather similarly to those in Concept 1, since in both concepts, the solar steam is fed to the process after the HP turbine section and the steam mass flow to the IP turbine increases. The more solar steam is produced, the more steam mass flow to the IP turbine increases (Figure 87). In Concept 2, the limiting factor of the maximum solar share is the rated capacity of the IP turbine section, which is 110% of the nominal inlet steam mass flow. With the maximum solar share, the steam mass flow to the IP turbine is increased by 9.8% from 101.6 kg/s to 111.6 kg/s. If 16th collector row would be added to the solar field, the IP turbine section would be overloaded.

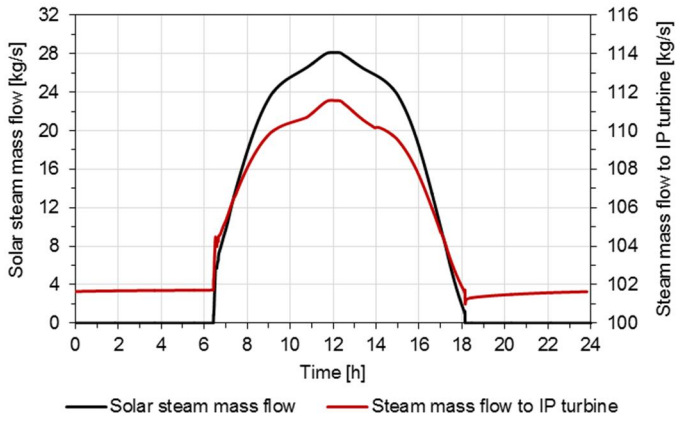

Figure 87. The rated capacity of the IP turbine section is the limiting factor for the amount of integrated solar steam in Concept 2.

Steam mass flow to the reheating increases due to solar integration, and consequently, also steam mass flow to the IP turbine increases (Figure 88). During the sunshine peak hours, the steam mass flow to the reheating equals the steam mass flow to IP turbine, as the reheater injection mass flow is decreased to zero. As more steam is expanded in the IP and LP turbine sections, the steam mass flow to the HP turbine is decreased. With the maximum solar share, the steam mass flow to the IP turbine is increased by 9.8%, whereas the steam mass flow to the HP turbine is decreased by 12.9% from 103.3 kg/s to 90.0 kg/s. Thus, the different turbine sections are more imbalanced than in Concept 1.

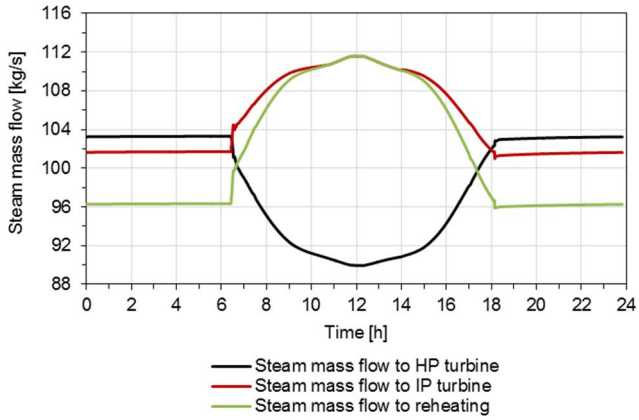

Figure 88. Effect of solar steam integration on steam mass flows to HP and IP turbine sections in Concept 2.

Similarly to Concept 1, the discharge temperature and pressure of the HP turbine and bled off steam temperature and pressure to the HP FWH2 increase (Figure 89). During the sunshine peak hours, the discharge temperature increases by 19.5 °C from 351.2 °C to 370.7 °C and the discharge pressure increases by 3.5 bar from 34.5 bar to 38 bar. As a result, the discharge temperature is higher than the design steam temperature of the solar field i.e. 360 °C. Thus, the solar steam actually cools down the steam entering the reheaters. The effect of increased discharge pressure can be seen in the solar steam pressure, which is slightly higher than the design pressure of 40 bar during the sunshine peak hours (Figure 85). As a result, the increase in discharge steam parameters in Concept 2 should be taken into account in the design of the solar field.

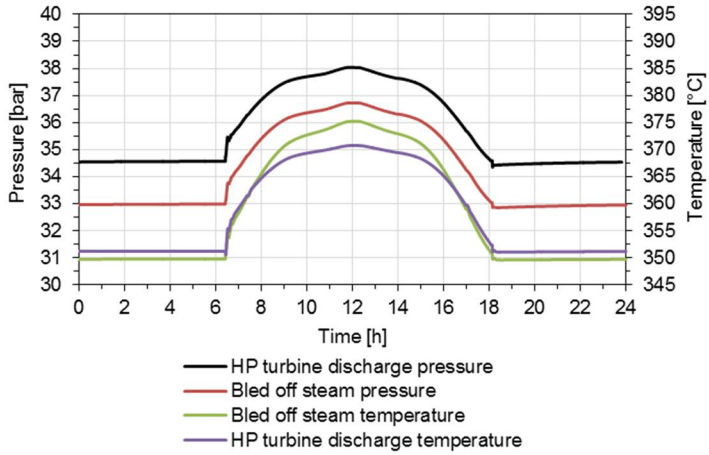

Figure 89. Effect of solar integration on discharge temperature and pressure and on bled off steam temperature and pressure in Concept 2.

As the bled off steam parameters increase, the feedwater temperature before the economiser increases by 6.6 °C from 237.1 °C to 243.8 °C (Figure 90). Due to the lower load of the steam boiler, the approach temperature difference increases by 3.6 °C from 13.4 °C to 17.0 °C. However, the approach temperature difference would be 23.4 °C if the steam boiler would be operated on the same load, but without solar thermal production. Thus, the solar integration significantly improves the boiler efficiency, as the approach temperature difference is 6.4 °C lower than without solar thermal production.

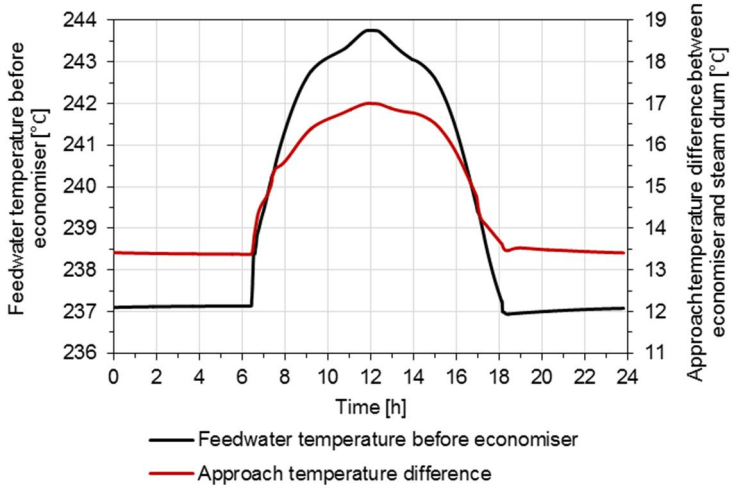

Figure 90. Effect of solar integration on feedwater temperature and approach temperature difference in Concept 2.

The changes in the feedwater temperature and approach temperature difference affect the flue gas temperature after air preheating in Concept 2 like in Concept 1. The flue gas temperature after the air preheating decreases only by 3.0 °C from 167.2 °C to 164.2 °C even though the boiler load is decreased by 16.8% from 100% to 83.2% due to the solar integration (Figure 91). Thus, the flue gas temperature is kept clearly above the dew point of flue gases even though the steam boiler load is decreased.

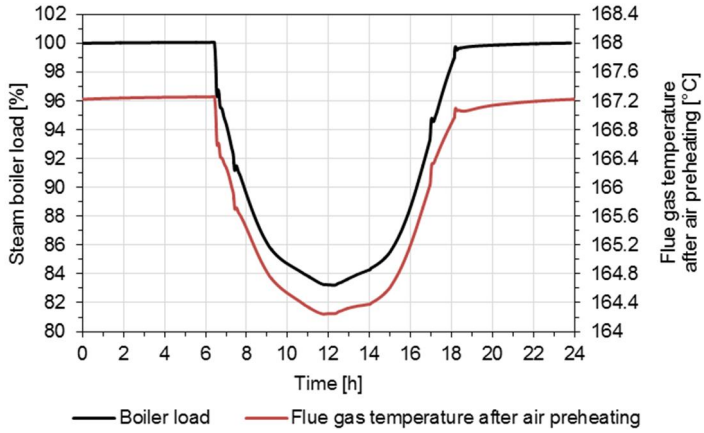

Figure 91. Effect of solar integration on boiler load and flue gas temperature after the air preheating in Concept 2.

Similarly to Concept 1, the heat surfaces of the steam boiler are imbalanced also in Concept 2. The injection flows of superheater and reheater decrease, as the steam boiler is operated on lower load (Figure 92). In addition, the required reheating power increases, as the solar integration increases steam mass flow to the reheating. During the sunshine peak hours, the superheater injection flow decreases by 64.0% from 8.1 kg/s to 2.9 kg/s, whereas the reheater injection flow decreases by 100% from 5.4 kg/s to zero. Thus, the heat surfaces are more imbalanced in Concept 2 than in Concept 1. Some variations in the steam temperatures occur especially during the start-up of the solar field, in which the live steam temperature decreases by 1 °C within 2 minutes, and the reheated steam temperature decreases by 2 °C within 2 minutes. However, the start-up variations are acceptable, as modern turbines resist temperature gradients up to 5 °C/min.

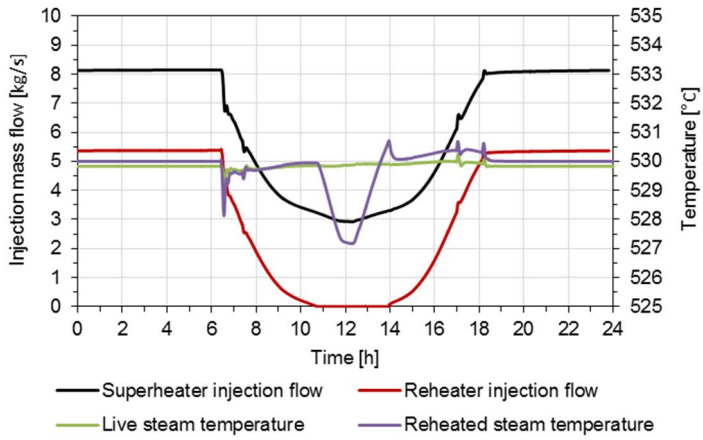

Figure 92. Effect of solar integration on live steam and reheated steam temperatures in Concept 2.

The increased steam mass flow to the IP turbine section results in increased water fraction of the exhaust steam and increased condensing power (Figure 93). In addition, as the reheated steam temperature decreases from 530 °C during the sunshine peak hours, the water fraction further increases. With the maximum solar share, the water fraction increases by 0.4 percentage points from 4.7% to 5.1% and the condensing power increases by 9.6% from 185.0 MW_{th} to 202.7 MW_{th}. During the solar field start-up, solar steam is fed to the condenser instead of the cold reheat line. Thus, the condensing power increases rapidly in the morning from 185.0 MW_{th} to 193.0 MW_{th}.

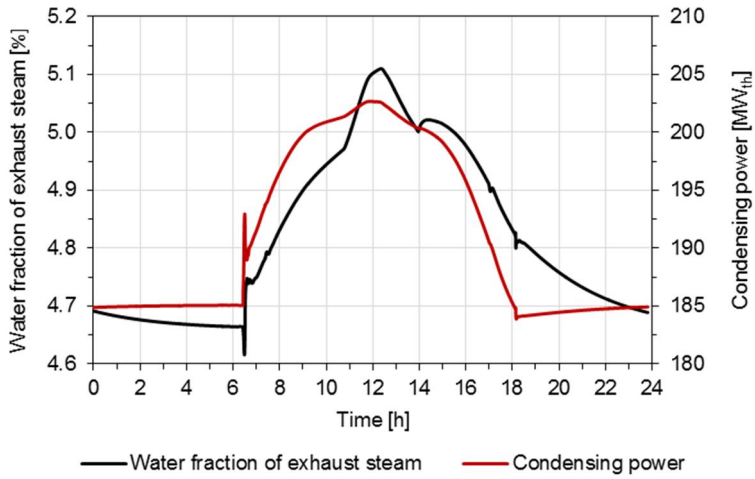

Figure 93. Effect of solar integration on the water fraction of exhaust steam and on the required condensing power in Concept 2.

To summarise, the main interdependencies of subsystems in Concept 2 include:

- The rated capacity of the IP turbine (limiting factor for the solar share);
- Increased imbalance of different turbine sections and heat transfer surfaces compared to Concept 1;
- Increased feedwater temperature before the economiser and significantly improved boiler efficiency;
- Decreased reheated steam temperature during the sunshine peak hours and its effects on the water fraction of the exhaust steam.

6.3.2 Performance figures

In Concept 2, the maximum thermal power of the solar field is 63.1 MW_{th} at noon on June 21st at Ouarzazate Morocco (Figure 94). Compared to Concept 1, the variations in power output are larger in Concept 2 during the start-up and shut-down of the solar field. During the start-up, the power output fluctuates few minutes from 119.9 MW_e to 120.3 MW_e until it stabilises to 120 MW_e. During the shutdown, the power output decreases to 119.7 MW_e, as the steam generation ends in the solar field.

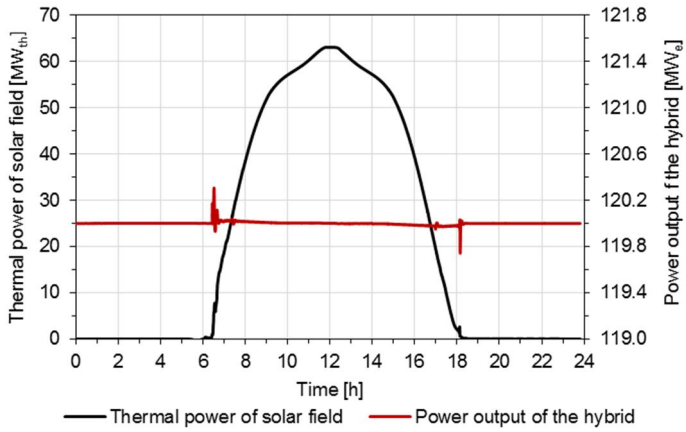

Figure 94. Effect of solar integration on the power output of the hybrid in Concept 2.

As the thermal power of the solar field increases, the fuel power and thermal power of the steam boiler decreases (Figure 95). With the maximum thermal power of the solar field, the fuel power is decreased by 16.7% from 341.5 MW to 284.4 MW and the thermal power of the steam boiler is decreased by 18.3% from 315.2 MW_{th} to 257.4 MW_{th}. Thus, the thermal power decreases more than the fuel power in Concept 2 like in Concept 1. As a result, the total energy input (thermal + fuel) is 347.6 MW, which is 1.83% more than the initial fuel power of the steam boiler. The

total thermal energy input (thermal + thermal) is 320.6 MW_{th}, which is 1.79% more than the initial thermal power of the steam boiler.

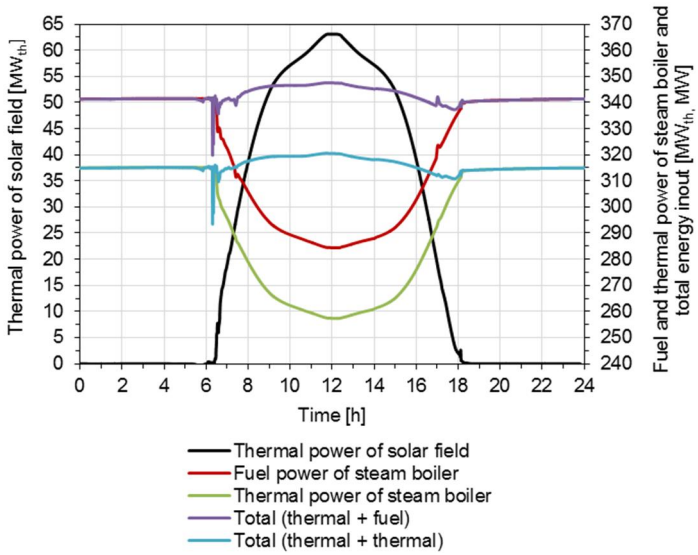

Figure 95. Effect of solar integration on thermal power and fuel power of the steam boiler in Concept 2.

Similarly to Concept 1, the efficiencies of the hybrid system are decreased in Concept 2 (Figure 96). With the maximum solar share, the thermal efficiency is decreased by 0.7 percentage points from 38.1% to 37.4%, whereas the net efficiency is decreased by 0.5 percentage points from 35.1% to 34.6%. The decreased efficiencies are due to the increased steam mass flow through the IP and LP turbine sections, which have lower isentropic efficiencies than the HP turbine section.

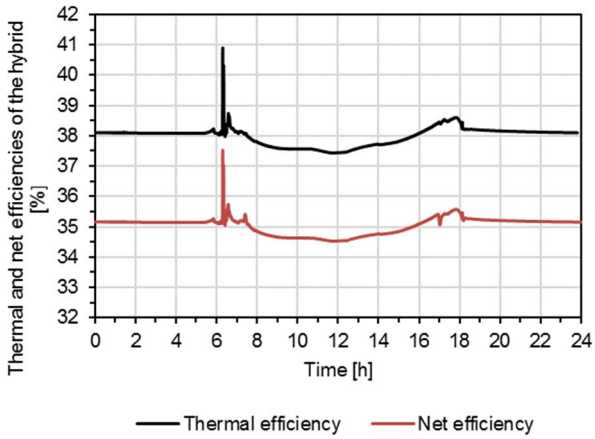

Figure 96. Thermal and net efficiencies of the hybrid system in Concept 2.

During the sunshine peak hours, the maximum thermal solar share is 19.7% and the maximum net solar share is 18.2% (Figure 97). However, the maximum achieved fuel and CO_2 emission savings are 16.8%. The achieved fuel and CO_2 emission savings are lower than the reached solar shares due to the decreased efficiencies of the hybrid system.

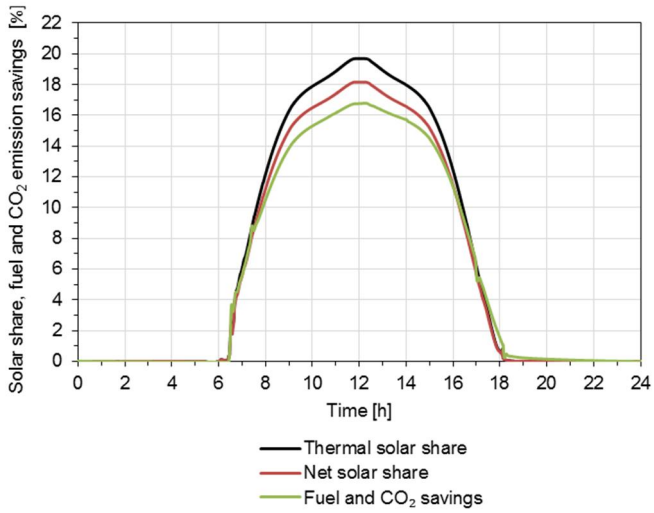

Figure 97. Maximum thermal and net solar shares and achieved fuel and CO_2 emission savings in Concept 2.

As a conclusion of the performance of Concept 2, the operation of the hybrid is quite steady during the start-up and shutdown of the solar field and during a clear day. However, the achieved fuel and CO_2 emission savings of 16.8% are still not enough compared to emission reduction target of 33% or higher (Figure 2). Higher savings could be reached by optimising the efficiency of the hybrid according to the process configuration. Thus, the isentropic efficiency of the IP and LP turbine sections should be higher than the HP turbine section's, which results in larger power output of the IP and LP turbine sections with the same steam mass flow.

6.3.3 Operation under transient solar irradiation conditions

A similar step change test was conducted to Concept 2 than to Concept 1 in order to study the capability of the steam boiler to compensate rapid and large changes in irradiance. Thus, the hybrid is operated on steady-state with peak solar share for the first 10 minutes (Figure 98). Then, a relative decrease in DNI of 50%/min from 824.8 W/m^2 to 247.3 W/m^2 is introduced for the whole solar field. The maximum gradient of fuel supply is 7% of MCR/30s, which is the same load change rate than in the pilot-scale CFB combustion tests (Chapter 3.2). In addition, the maximum amount of fuel supply is 110% of the nominal supply. After the step

change, the solar steam mass flow decreases by 21.2 kg/s from 28.2 kg/s to 7.0 kg/s within 4 minutes.

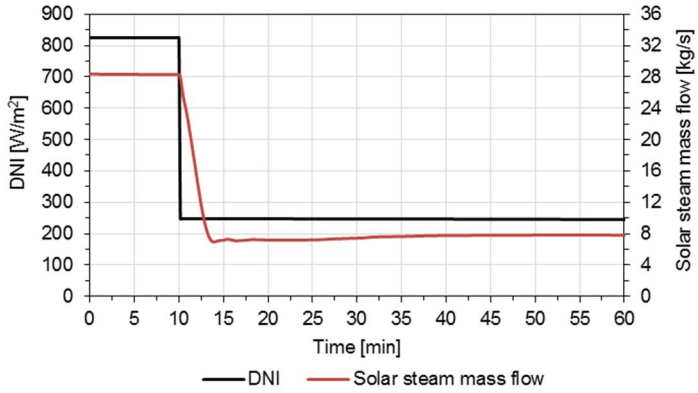

Figure 98. Effect of 70% DNI step change on solar steam mass flow in Concept 2.

As the solar steam mass flow to the cold reheat line decreases, the steam mass flows to the IP turbine and to the reheating decrease (Figure 99). The steam mass flow to the IP turbine is decreased by 9.9 kg/s from 111.5 kg/s to 101.6 kg/s within 4 minutes. After this, the steam mass flow stabilises to 104.0 kg/s, as the reheater injection mass flow increases due to the higher load of the steam boiler. As less steam is expanded in the IP and LP turbine sections, the steam mass flow to the HP turbine increases from 89.6 kg/s to 99.3 kg/s within 10 minutes after the step change.

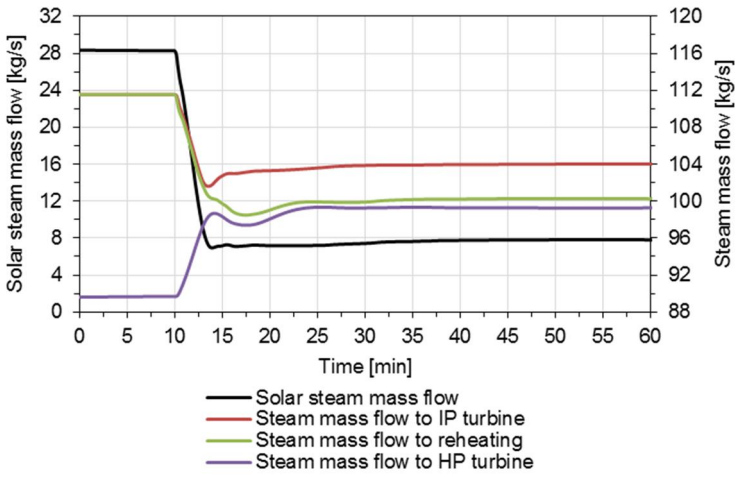

Figure 99. Effect of decreased solar steam mass flow to other steam mass flows in Concept 2.

Due to the step change, the live steam and reheated steam temperatures would increase if the injection mass flows are not increased. The live steam temperature increases from 530.0 °C to 534.4 °C within 8 minutes, though the superheater injection mass flow increases from 2.8 kg/s to 8.9 kg/s (Figure 100). The reheated steam temperature increases from 530.0 °C to 537.6 °C within 6 minutes, though the reheater injection mass flow increases from 0.0 kg/s to 4.7 kg/s. As a result, the maximum temperature gradient of the reheated steam is 1.3 °C/min, which is below the allowed maximum temperature gradient for turbines (approximately 5 °C/min).

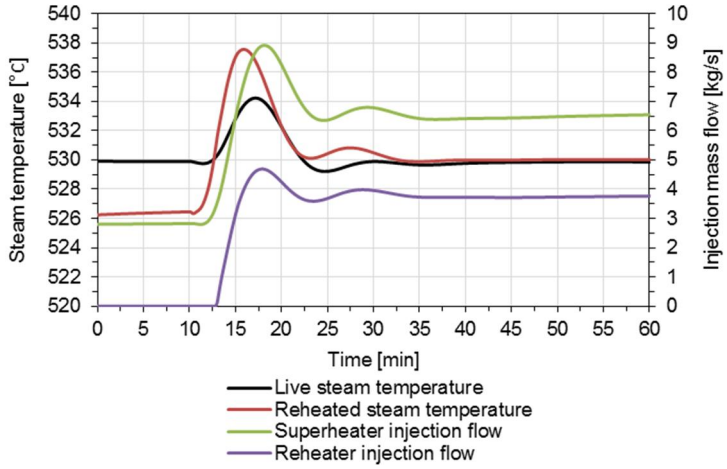

Figure 100. Effect of 70% step change on live steam and reheated steam temperatures in Concept 2.

Due to the step change and its effects on the steam mass flows, the power output of the hybrid decreases by 1.4 MW_e from 120.0 MW_e to 118.6 MW_e in 2.5 minutes (Figure 101). Thus, the power output gradient is 0.46% of MCR/min. Since the power output decreases, more steam is fed to the HP turbine section. The larger solar share in Concept 2 results in larger fluctuations of the power output and the live steam mass flow compared to Concept 1.

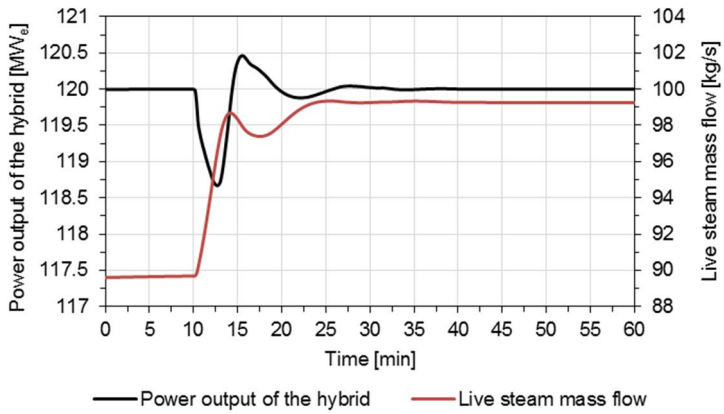

Figure 101. Effect of 70% step change on the power output of the hybrid and on the live steam mass flow in Concept 2.

As the power output decreases, the live steam mass flow is increased by opening the main steam valve before the HP turbine section. As a result, the live steam pressure before the main steam valve decreases by 3.3 bar from 120.0 bar to 116.7 bar within 4 minutes after the step change (Figure 102). The fuel mass flow increases by 0.66 kg/min from 19.2 kg/s to 22.9 kg/s within 6 minutes after the step change.

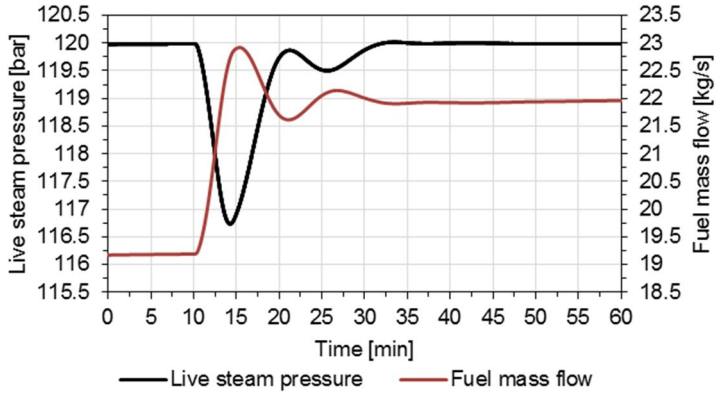

Figure 102. Effect of 70% step change on live steam pressure and on fuel mass flow in Concept 2.

As a conclusion of the transient case in Concept 2, the effects of large step change on the main operation parameters are similar but larger than in Concept 1. However, the effects are still compensable by developing the control system and adapting DNI forecasting. Thus, the cold reheat line concept seems to be technically feasible, but more challenging than the feedwater preheating concept.

6.4 High pressure turbine concept

In the high pressure turbine concept (Concept 3), the solar field generates steam parallel with the steam boiler to a joint HP turbine section. The superheated solar steam replaces part of the live steam mass flow expanding through all the turbine sections. Thus, the solar steam does not bypass the HP turbine section with the highest isentropic efficiency. The design steam pressure and temperature of the solar field are 530 °C and 120 bar (Figure 103), which are achieved within 10 minutes during the start-up of the solar field. The steam parameters are kept constant during the daily operation. After the shutdown of the solar field, the steam pressure gradually decreases from 120 bar to 0.7 bar and the steam temperature from 530 °C to 58 °C.

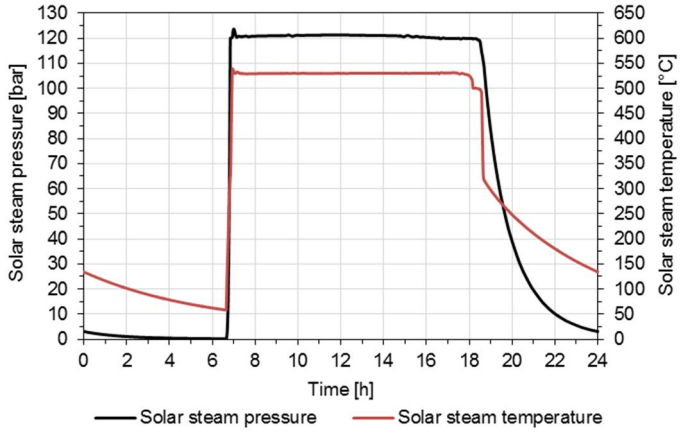

Figure 103. Solar steam pressure and temperature in Concept 3.

In Concept 3, the solar field consist of 10 collector rows, and the maximum steam mass flow to the joint HP turbine section is 39.0 kg/s at noon on June 21st (Figure 104). During the start-up of the solar field, the solar steam is fed to the condenser as long as the solar steam temperature is less than 450 °C. The peak steam mass flow to the condenser is 6.9 kg/s during the start-up.

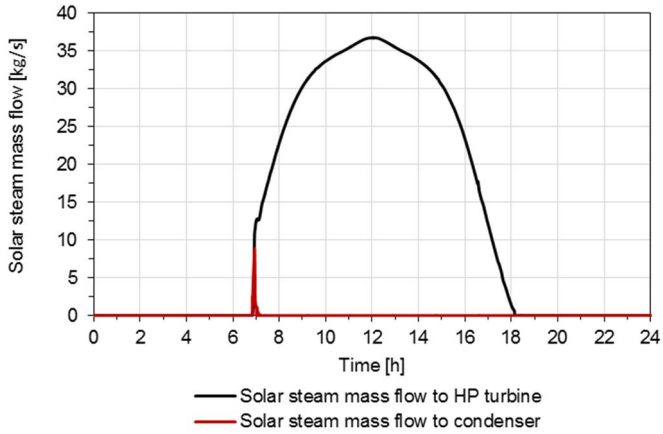

Figure 104. Solar steam mass flow to the HP turbine and to the condenser in Concept 3.

6.4.1 Interdependencies of subsystems

The interdependencies of subsystems are differently affected in Concept 3 than in other concepts, as the solar steam does not bypass the HP turbine with the highest isentropic efficiency in Concept 3 like in Concepts 1 and 2. In Concept 3, the limiting factor for the maximum solar share is the rated capacity of the HP turbine section (110% of the nominal inlet steam mass flow). The more solar steam is fed to the turbine, the more live steam mass flow increases although the hybrid is operated on fuel saving mode (Figure 105). If 11th collector row would be added to the system, the HP turbine would be overloaded during the sunshine peak hours if any solar energy were not dumped in the solar field.

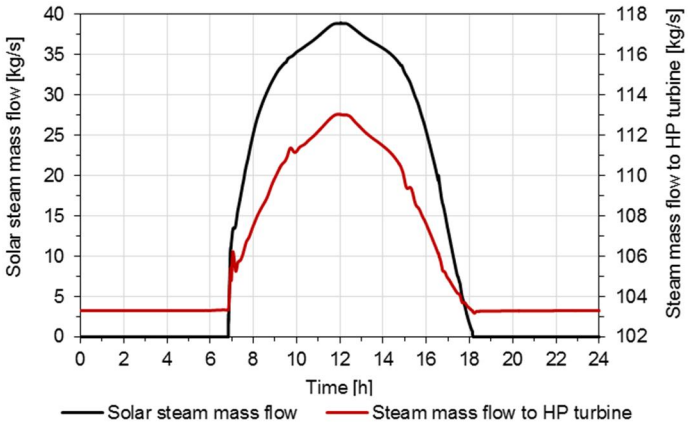

Figure 105. Solar steam mass flow and steam mass flow to the HP turbine in Concept 3.

As the live steam mass flow increases, the steam mass flow to the IP turbine decreases in the morning (Figure 106), which is a result of the increased reheater load with respect to the steam boiler load and decreased reheater injection flow. However, the steam mass flow to the IP turbine starts to increase after the reheater injection mass flow has decreased to zero. Thus, the lower quality of the reheated steam is compensated by higher steam mass flow in order to keep the power output of the hybrid constant. During the sunshine peak hours, the steam mass flow to the HP turbine increases by 9.4% from 103.3 kg/s to 113.1 kg/s and the steam mass flow to the IP turbine increases by 5.8% from 101.7 kg/s to 107.6 kg/s, Thus, the different turbine sections are more balanced in Concept 3 compared to Concepts 1 and 2.

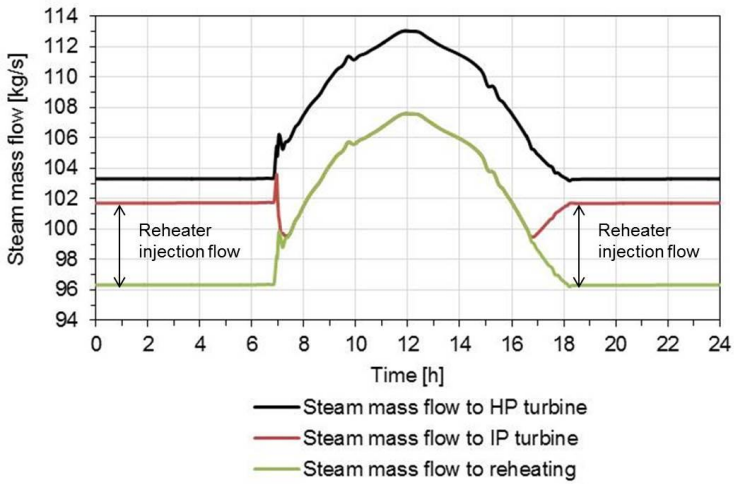

Figure 106. Effect of solar integration on steam mass flows to the HP and IP turbine sections in Concept 3.

Compared to Concepts 1 and 2, the discharge temperature and pressure of the HP turbine first decreases in the morning in Concept 3 (Figure 107), since the steam mass flow to the HP turbine increases and the steam mass flow to the IP turbine decreases. In addition, the discharge temperature further decreases, as the live steam temperature decreases from its design value of 530 °C. However, the discharge pressure starts to increase, as the steam mass flow to the IP turbine section starts to increase. During the sunshine peak hours, the discharge temperature is decreased by 17.3 °C from 351.2 °C to 333.9 °C, whereas the discharge pressure is increased by 0.7 bar from 34.5 bar to 35.2 bar. During the solar field start-up, the discharge temperature is decreased from 351.2 °C to 343.2 °C, as the solar steam temperature is between 450 °C and 530 °C. In addition, the discharge pressure is increased from 34.5 bar to 35.2 bar due to the steam mass flow peak to the condenser.

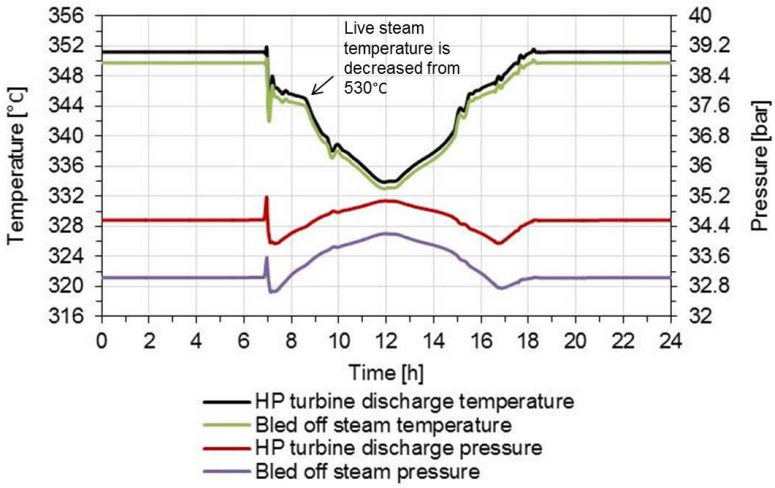

Figure 107. Effect of solar integration on the HP turbine discharge pressure and temperature and on the bled off steam temperature and pressure in Concept 3.

Like in Concepts 1 and 2, the bled off steam temperature and pressure to HP FWH2 follow the discharge steam parameters in Concept 3. During the sunshine peak hours, the bled off steam temperature is decreased by 16.8 °C from 349.8 °C to 333.0 °C and the bled off steam pressure is increased by 1.2 bar from 33.0 bar to 34.2 bar. During the solar field start-up, the bled off steam temperature decreases from 349.7 °C to 342.1 °C, as the solar steam temperature is between 450 °C and 530 °C. In addition, the bled off steam pressure increases from 33.0 bar to 33.5 bar due to the steam mass flow peak to the condenser.

The feedwater temperature before the economiser increases even though the bled off steam temperature decreases and the bled off steam pressure slightly increases. The feedwater temperature before the economiser increases by 2.9 °C from 237.1 °C to 240.0 °C (Figure 108). The increased feedwater temperature is caused by the higher load of turbines with respect to the steam boiler load, which results in higher bled off steam parameters compared to the decreased feedwater mass flow through HP FWHs. Due to the lower load of the steam boiler, the approach temperature difference increases by 17.2 °C from 13.4 °C to 30.6 °C. However, the approach temperature difference would be 36.9 °C without the solar integration, while the steam boiler is operated on the same load. Thus, the solar integration significantly improves the boiler efficiency, as the approach temperature difference is 6.3 °C lower than with the same load level without solar thermal production. However, the improvements in the approach temperature difference are nearly the same in Concept 3 than in Concept 2 even though larger solar steam mass flow is fed to the system in Concept 3 compared to Concept 2. As a result, Concept 3 improves the boiler efficiency relatively less than Concept 2.

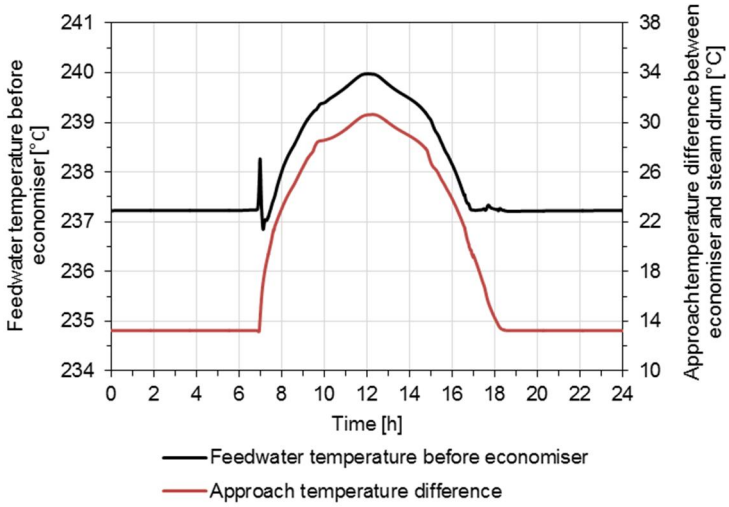

Figure 108. Effect of solar integration on feedwater temperature and approach temperature difference in Concept 3.

In Concept 3, the flue gas temperature after air preheating decreases by 12.1 °C from 167.2 °C to 155.1 °C, as the boiler load decreases by 33.6% from 100% to 66.4% due to the solar integration (Figure 109). Compared to Concept 2, the flue gas temperature decreases four times more in Concept 3, while the steam boiler load decreases only two times more. Thus, the control of the flue gas temperature is more challenging in Concept 3 than in Concept 2, as the temperature must be kept above the dew point of flue gases.

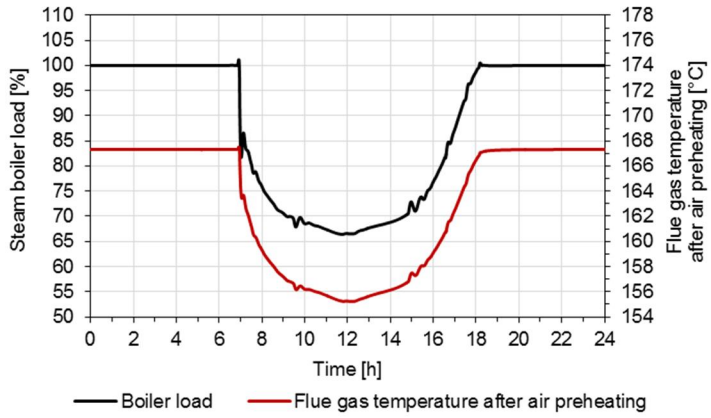

Figure 109. Effect of solar integration on boiler load and flue gas temperature after air preheating in Concept 3.

In Concept 3, the heat surfaces are imbalanced like in Concepts 1 and 2. However, the imbalance in Concept 3 is due to the increased reheating load in respect of

the steam boiler load. In Concepts 1 and 2, the imbalance is mainly due to the increased steam mass flow through reheating, as the solar steam is fed directly to the reheating. Due to the solar integration in Concept 3, both the superheater and reheater injection mass flows decrease to zero and the steam temperatures start to decrease (Figure 110). The reheated steam temperature starts to decrease shortly after the solar field start-up, whereas the live steam temperature starts to decrease after the solar steam mass flow has increased to 28.9 kg/s and the steam boiler load has decreased to 73.3% load. During the sunshine peak hours, the live steam temperature decreases by 14.2 °C from 530.0 °C to 515.8 °C, and the reheated steam temperature decreases by 68.2 °C from 530.0 °C to 461.8 °C. The decreased steam temperatures result in decreased efficiency of the steam cycle. Some variations of the steam temperatures occur especially during the start-up of the solar field, in which the live steam temperature decreases by 4.3 °C within 4.5 minutes, and the reheated steam temperature decreases by 7.5 °C within 7 minutes. However, the start-up temperature variations are acceptable, as modern turbines resist temperature gradients up to 5 °C/min.

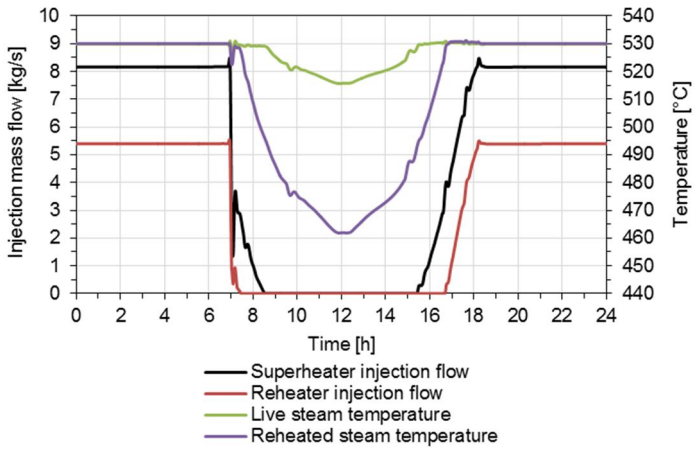

Figure 110. Effect of solar integration on the live steam and reheated steam temperatures in Concept 3.

The decreased steam temperatures result in increased water fraction of the exhaust steam in Concept 3 like in Concept 2. However, the water fraction increases more in Concept 3 than in Concepts 1 and 2. During the sunshine peak hours, the water fraction increases from 4.7% to 6.9 % (Figure 111). However, the water fraction is kept under 12%, which is typically the maximum water fraction of the exhaust steam in order to prevent condensation to the turbine blades. As the turbines are more in balance in Concept 3 than in Concept 2, the condensing power increases only by 3.8% from 185.0 MW_{th} to 192.0 MW_{th} during the sunshine peak hours, whereas in Concept 2, the condensing power increases by 9.6%. However, during the solar field start-up, the condensing power increases rapidly from 185.0 MWth to 215.8 MW_{th} in Concept 3. As a result, the water consumption of conden-

ser is lower in Concept 3 than in Concept 2, but the start-up of the solar field is more difficult to handle in Concept 3.

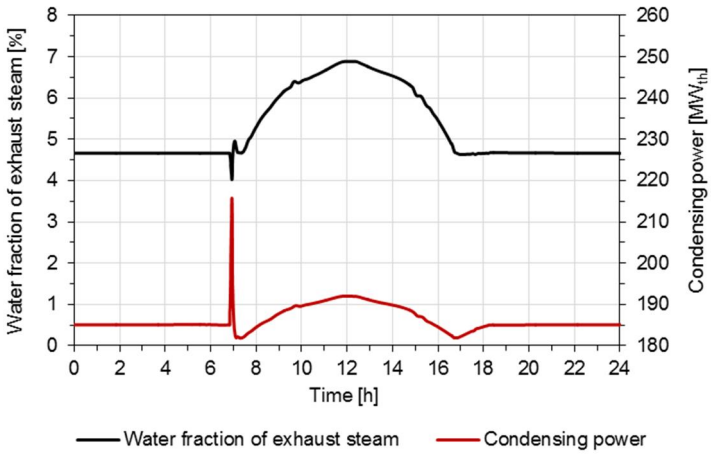

Figure 111. Effect of solar integration on the water fraction of exhaust steam and on the required condensing power in Concept 3.

To summarise, the main interdependencies of subsystems in Concept 3 include:

- The rated capacity of the HP turbine (limiting factor for the solar share);
- Smaller imbalance of turbine sections compared to Concept 2;
- Increased feedwater temperature before the economiser, but relatively smaller boiler efficiency improvement compared to Concept 2;
- More challenging control of the flue gas temperature at the end of flue gas duct compared to Concept 2
- Decreased live steam and reheated steam temperatures, which lowers the steam cycle efficiency and increases the water fraction of the exhaust steam;
- Lower required condensing power compared to Concept 2.

6.4.2 Performance figures

In Concept 3, the maximum thermal power of the solar field is 106.5 MW_{th} at noon on June 21st at Ouarzazate Morocco (Figure 112). Compared to other concepts, the variations of the power output are larger in Concept 3 during the start-up of the solar field. The power output fluctuates 10 minutes from 119.7 MW_e up to 121.3 MW_e until it stabilises to 120 MW_e. During the day and the shutdown, the power output of the hybrid is kept constant.

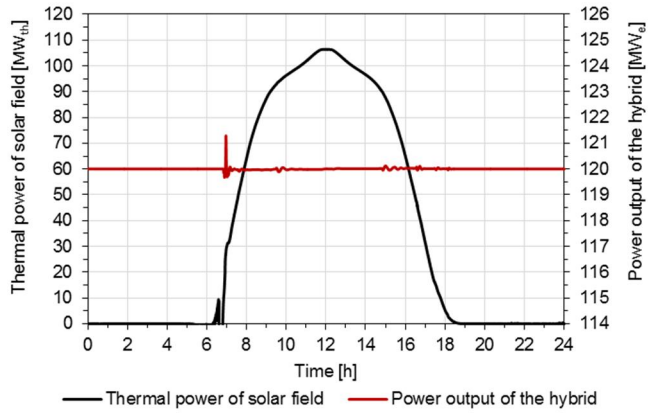

Figure 112. Effect of solar integration on the power output of the hybrid in Concept 3.

As the thermal power of the solar field increases, the fuel power and thermal power of the steam boiler decreases (Figure 113). With the maximum thermal power of the solar field, the fuel power is decreased by 33.4% from 341.5 MW to 227.4 MW and the thermal power of the steam boiler is decreased by 34.8% from 315.2 MW_{th} to 205.4 MW_{th}. Similarly to other concepts, thermal power decreased more than the fuel power. During the sunshine peak hours, the total energy input (thermal + fuel) is 333.9 MW, which is 2.22% less than the initial fuel power of the steam boiler. The total thermal energy input (thermal + thermal) is 311.9 MW_{th}, which is 1.1% less than the initial thermal power of the steam boiler. However, during the solar field start-up and shutdown even lower total energy inputs are achieved, as the live steam temperature is not decreased from its design value of 530 °C.

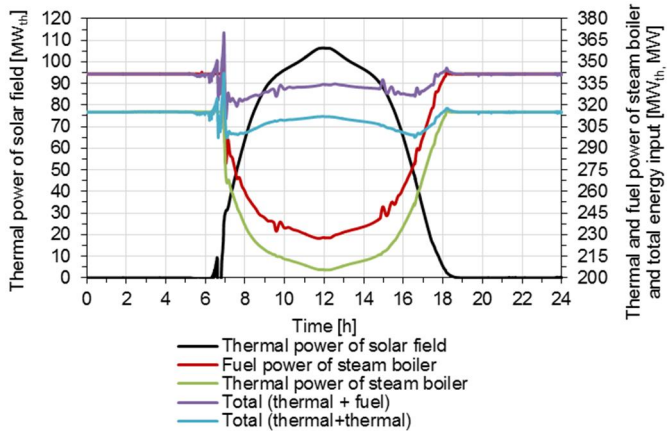

Figure 113. Effect of solar integration on the thermal power and fuel power of the steam boiler in Concept 3.

In Concept 3, the efficiencies of the hybrid system increase in particular during the solar field start-up and shutdown (Figure 114). The increased efficiencies are due to the increased steam mass flow through the HP turbine section, which has the highest isentropic efficiency of the turbine sections. As the live steam and reheated steam temperatures decrease, the efficiencies decrease as well. However, the thermal efficiency is 38.5% at noon, which is 0.4 percentage points higher than the initial thermal efficiency. The net efficiency is 35.9% at noon, which is 0.8 percentage points higher than the initial net efficiency. Thus, the efficiencies are improved during the day even though the steam temperatures decrease. Even higher efficiencies could be reached if the design live steam and reheated steam temperatures could be maintained.

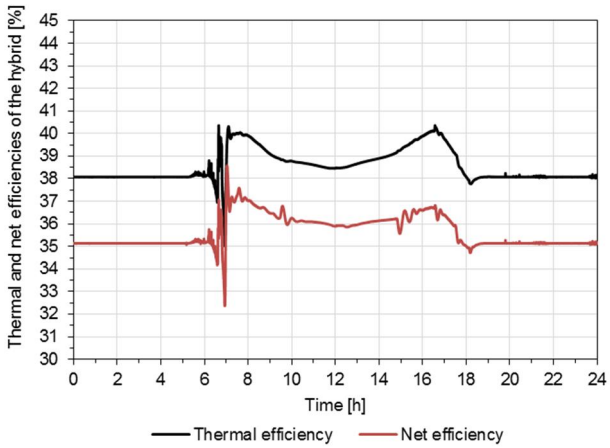

Figure 114. Thermal and net efficiencies of the hybrid system in Concept 3.

During the sunshine peak hours, the maximum thermal solar share is 34.1% and the maximum net solar share is 31.9% (Figure 115). The maximum achieved fuel and CO_2 emission savings are 33.6%. Thus, the achieved fuel and CO_2 emission savings are higher than the maximum net solar share but lower than the maximum thermal solar share. The reason for this is the improved overall efficiency of the turbines, which results in higher fuel savings. On the contrary, the higher reheating load in respect of the steam boiler load increases the thermal power of the steam boiler with respect to the fuel power. Thus, the total energy input (thermal + thermal) is relatively more than the total energy input (fuel + thermal), and the achieved savings are less than the maximum thermal solar share.

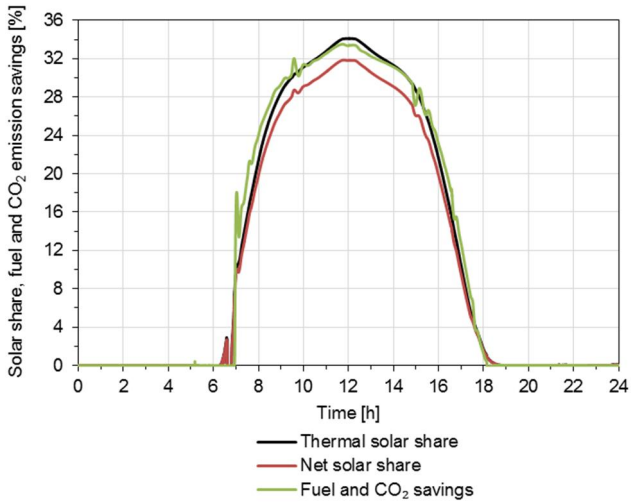

Figure 115. Maximum thermal and net solar shares and achieved fuel and CO_2 emission savings in Concept 3.

As a conclusion of the performance of Concept 3, the operation of the hybrid is quite steady during the start-up and shutdown of the solar field and during a clear day. The achieved fuel and CO_2 emission savings are 33.6%, which slightly exceeds the emission reduction target of 33% (Figure 2). However, these emission reductions are achieved only during the peak solar irradiation conditions and thus the average annual emission reductions are lower than 33.6%. Higher savings could be reached by integrating an energy storage to the system and by designing the heat surfaces of the steam boiler to better maintain the design steam temperatures, while integrating a larger solar field to the system.

6.4.3 Operation under transient solar irradiation conditions

Like in Concepts 1 and 2, a large step change test was conducted to study the capability of the steam boiler to compensate rapid and large changes in irradiance. Thus, the hybrid is operated on steady-state with peak solar share for the first 10 minutes (Figure 116). Then, a relative decrease in DNI of 50%/min from 824.8 W/m^2 to 247.3 W/m^2 is introduced for the whole solar field. The maximum gradient of fuel supply is 7% of MCR/30s, which is the same load change rate as in the pilot-scale CFB combustion tests (Chapter 3.2). The maximum amount of fuel supply is 110% of the nominal supply. After the step change, the solar steam mass flow decreases from 39.1 kg/s to 0.01 kg/s within 4 minutes and then stabilised to 8.8 kg/s.

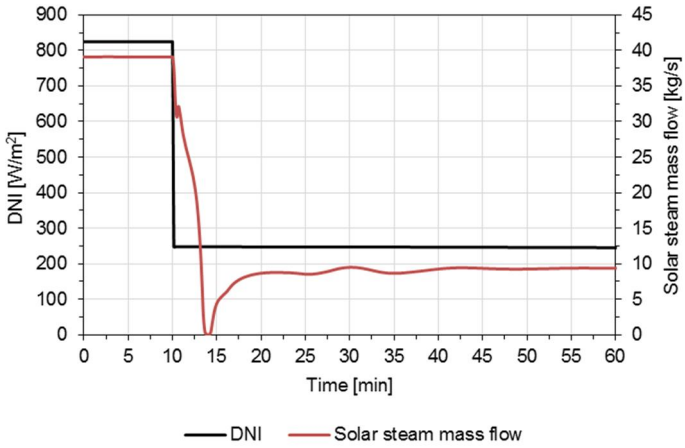

Figure 116. Effect of 70% DNI step change on the solar steam mass flow in Concept 3.

The reason for the rapid decrease in solar steam mass flow is the effect of the step change on solar steam pressure (Figure 117). The solar steam pressure decreases from 121.3 bar to 115.1 bar before the solar steam mass flow decreases to almost zero. Thus, the steam pressure control valve at the outlet of the solar field closes almost fully in order to prevent the pressure decrease in the solar field.

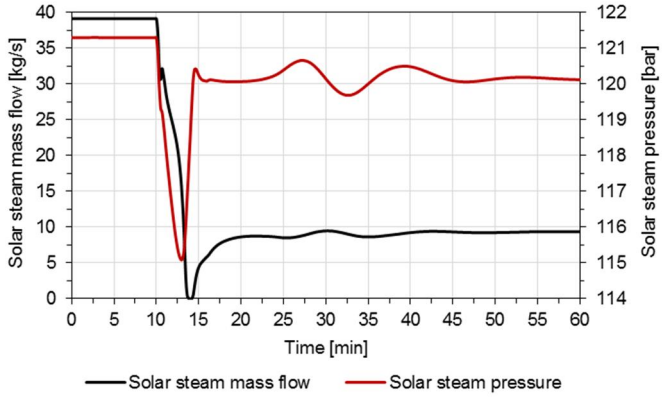

Figure 117. Effect of 70% step change on the solar steam pressure in Concept 3.

As the solar steam mass flow to the HP turbine section decreases, also the steam mass flows to the IP turbine and to the reheating decreases (Figure 118). The steam mass flow to the HP turbine decreases by 13.3 kg/s from 113.0 kg/s to 99.7 kg/s within 7 minutes. The steam mass flow to the IP turbine decreases by 13.2 kg/s from 107.6 kg/s to 94.4 kg/s within 7 minutes after the step change, and the steam mass flow to the reheating decreases by 13.8 kg/s from 107.6 kg/s to 93.8 kg/s within 8 minutes after the step change. Then, the steam mass flows to the HP

turbine, to the IP turbine and to the reheating stabilise to 104.5 kg/s, 100.3 kg/s and 97.9 kg/s, respectively, as the steam boiler load and injection mass flows increase.

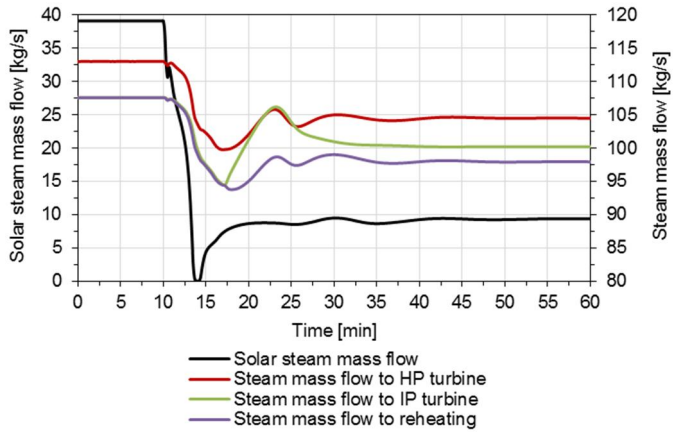

Figure 118. Effect of decreasing solar steam mass flow to other steam mass flows in Concept 3.

In Concept 3, the control of steam temperatures is more challenging than in Concepts 1 and 2. Due to the step change, the live steam temperature first decreases from 515.5 °C to 498.0 °C within 3 minutes after the step change (Figure 119). Then, as the steam boiler load increases, the live steam temperature increases from 498.0 °C to 541.8 °C within the next 8 minutes. Thus, the maximum live steam temperature gradient is 5.8 °C/min, which is over the acceptable gradient of 5 °C/min. The situation is challenging also with the reheated steam temperature, which increases by 79.8 °C from 461.2 °C to 541.0 °C within 10 minutes after the step change. Thus, the maximum temperature gradient is 8 °C/min, which is clearly over the acceptable gradient of 5 °C/min.

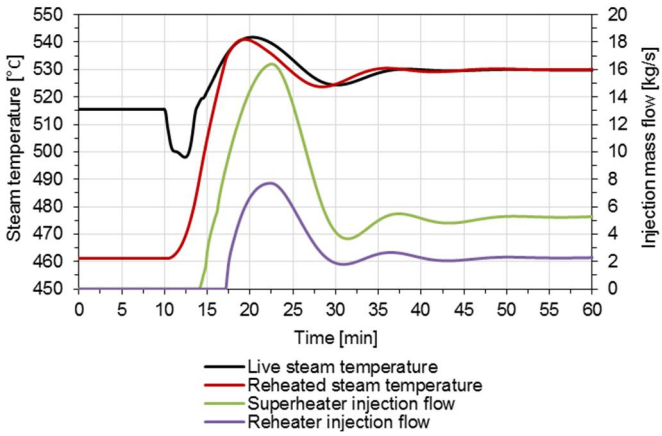

Figure 119. Effect of 70% step change on the live steam and reheated steam temperatures in Concept 3.

Similarly to the steam temperatures, the control of the power output is more challenging in Concept 3 than in Concepts 1 and 2. Due to the step change and its effects on steam mass flows (Figure 120), the power output of the hybrid first decreases by 6.4 MW_e from 120.0 MW_e to 113.6 MW_e in 5 minutes. Then, the power output increases by 12.7 MW_e from 113.6 MW_e to 126.3 MW_e in 8 minutes until the power output stabilises to 120 MW_e in 17 minutes after the step change. Thus, the maximum power output gradient is 1.3% of MCR/min. As a result, the larger solar share in Concept 3 results in larger fluctuations in the power output compared to Concepts 1 and 2. In addition, the stabilisation time of the power output is rather long after the step change. The solar steam mass flow can fluctuate quite rapidly due to the intermittency of solar irradiation, which could result in further problems with the power output control.

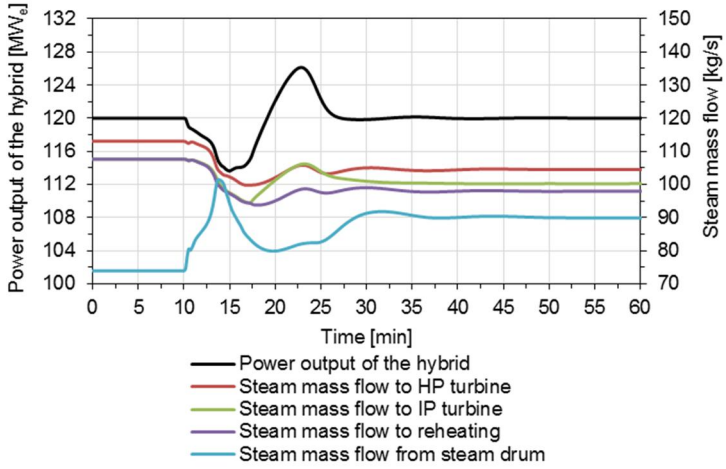

Figure 120. Effect of step change on the power output of the hybrid and on the steam mass flows in Concept 3.

As the power output decreases, the live steam mass flow is increased by opening the main steam valve before the HP turbine section. As a result, the live steam pressure before the main steam valve decreases by 17.4 bar from 120.0 bar to 102.6 bar within 7 minutes after the step change. Consequently, the fuel mass flow increases from 15.4 kg/s to the maximum fuel mass flow of 25.1 kg/s (110% of the nominal mass flow) within 4 minutes after the step change (Figure 121). Compared to the stabilisation time of the power output, the stabilisation time of fuel supply is even longer, as it takes approximately 30 min after the step change. As a conclusion, even though the fuel mass flow increases with its maximum gradient (7% of MCR/30s) to its maximum value (110% of nominal mass flow), the steam boiler's capacity is not enough to compensate the effects of large step change in solar irradiation.

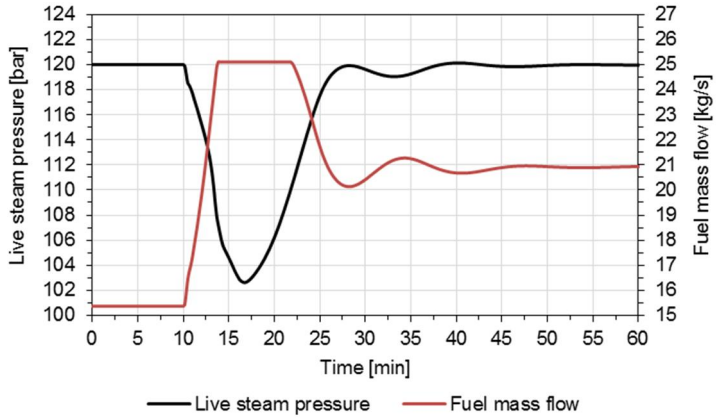

Figure 121. Effect of 70% step change on the live steam pressure and on the fuel mass flow in Concept 3.

As a conclusion of the transient case in Concept 3, the effects of large step change are major on the main operation parameters of the hybrid system. Thus, the control of steam temperatures, power output of the hybrid and live steam pressure are challenging to manage in the step change test. The situation is even more challenging during complex intermittent solar irradiation conditions. However, by developing the control of the hybrid and DNI forecasting, the variations in the solar steam production can be foreseen and compensated better than with the simple PI-controllers applied in the model. In addition, the load change capacity of the steam boiler needs to be improved. Thus, the high pressure turbine concept needs more research and development before it can be considered as technically feasible concept.

7. Conclusions and recommendations

Hybrid system combining concentrated solar power (CSP) and conventional solid fuel-fired power plant is a relevant technical solution to increase the amount of renewable energy in the energy system and to decrease related greenhouse gas emissions and fuel consumption. CSP technology utilizes solar irradiation, which is a clean, free and non-exhausting source of energy. Unlike PV and wind, CSP is considered as a dispatchable source of energy due to the possibility to easily decouple the solar energy collection and power generation by adding a thermal energy storage to the system (Figure 122). The value of dispatching power into peak demand periods is very country- and project-specific, an estimation of 11 to 47 €/MWh is given by IREANA (International Renewable Energy Agency 2012). The continuously growing share of intermittent renewable generation in the energy system is expected to increase the value.

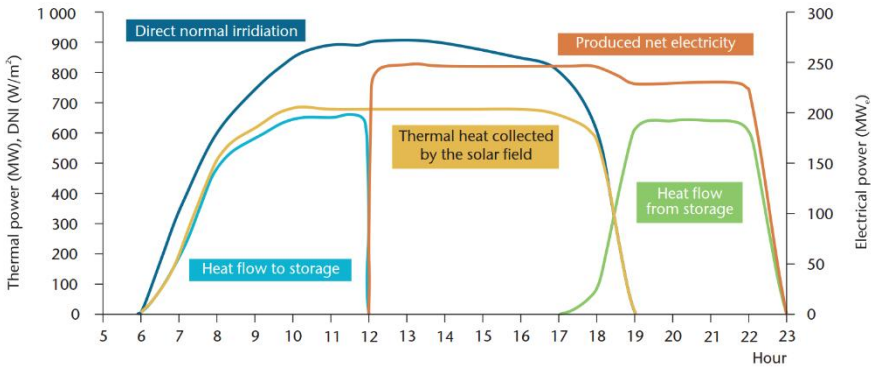

Notes: the graph shows on left scale the DNIR and the flows of thermal exchanges between solar field, storage and power block, and on the right scale electricity generation of a 250-MW (net) CSP plant with storage. Courtesy of ACS Cobra.

Figure 122. Decoupling of solar energy collection and power production (International Energy Agency 2014).

Besides energy storage technologies, dispatchability can be achieved by integrating the CSP field to the conventional power plant, when the solid fuel, i.e. coal or biomass, balances the intermittent solar thermal production. In the case of coal-fired power plant, major impacts of the integration are the reduced GHG emissions

and fuel consumption. Solar energy integration to the biomass-fired plant enhances the sustainable use of biomass resources, which is critical especially in the sun-rich, but typically arid regions. Thus, the technology integration improves the resource efficiency of the system. For water scarce regions, the water consumption is one of the limiting factors while using wet-dry or wet cooling methods. Hybridization supports the technology transfer to wider geographical locations. Hybridization provides also many other benefits, of which one is the cost reduction of CSP technology compared to stand-alone plants, provided by the shared equipment of two different power production technologies.

7.1 Overview of the COMBO-CFB research

The project “Combination of Concentrated Solar Power (CSP) with Circulating Fluidized Bed (CFB) power plants” (COMBO-CFB) aimed at developing innovative, flexible and high-efficient hybrid concept, in which solar thermal energy is integrated with a steam power plant. The novel hybrid concept was required to be flexible in operation while utilizing the joint infrastructure and balancing the distributed intermittent production. The development of the concept COMBO-CFB project included both theoretical and experimental research and dynamic modelling and simulation.

The research focused on the capacity building in the field of CSP and hybrid technologies and technical feasibility of the hybrid concepts, including the benefits provided by different concepts, challenges and possible future improvements. Relevant measures to evaluate the feasibility of hybrid concepts were determined in the course of the project. The research and development included data gathering and analyses of various CFB boiler and solar field designs and weather forecasting for the needs of the concept modelling and virtual demonstration. The effects of CSP integration on combustion dynamics were analyzed with test sets for a pilot-scale CFB boiler, in which the combustion phenomena and emission formation were studied during rapid load changes typical for a hybrid CSP plant. Multiple CSP technologies and hybrid concepts were virtually demonstrated through dynamic modelling and simulation. This allowed analyzing the interactions between the solar field and the steam boiler, developing control strategies and analyzing the effects of different hybridization schemes. The analysis of different concepts provided new knowledge on the dimensioning and operation of hybrid power plants in terms of the highly dynamic nature of the hybrid power plant.

In the COMBO-CFB project, different stand-alone CSP solutions and different hybrid concepts were studied and modelled in detail. In addition, different thermochemical processes and applications were reviewed. In terms of stand-alone CSP solutions, dynamic models were developed and analysis conducted for different parabolic trough, linear Fresnel and central receiver designs, namely:

- Direct steam generating linear Fresnel solar field (Chapter 5.1)
- Molten salt linear Fresnel solar field with two-tank thermal energy storage system (Chapter 5.2)
- Direct-heated supercritical carbon dioxide plant with Brayton cycle (Chapter 5.3)
- Indirect supercritical carbon dioxide plant with Brayton cycle (Chapter 5.4)
- Central receiver solar field (Chapter 5.5)

Detailed analysis and concept development was carried out for the following hybrid configurations:

1) Concept 1: Feedwater preheating configuration (Chapter 6.2)
2) Concept 2: Cold reheat line configuration (Chapter 6.3)
3) Concept 3: High pressure turbine configuration (Chapter 6.4)

7.2 Design considerations

Since the performance and interactions between different subsystems of the hybrid are very sensitive for the changes in solar steam production, dynamic analysis is utmost important in the design phase of the plant. The simulation results revealed the interactions and the restricting issues, which should be in particular taken care of while designing a hybrid plant. However, these issues might be different for hybrid plants with different technical specifications.

Maximum thermal and net solar shares, thermal and net efficiencies of the hybrid, and fuel and emission savings in three different concepts are summarized in Table 12 and Figure 123. The maximum solar share of a certain hybrid plant depends on the design and dimensioning of the subsystems. In Concept 1, larger solar share could be achieved by extracting the feedwater at lower temperature and conducting the feedwater preheating in the solar field instead of the feedwater preheaters. In Concept 2, redesigning of the heat transfer surfaces of the steam boiler could minimize the imbalances and allow increasing the solar share. Also an additional burner could be installed to boost the steam temperature. In Concept 3, higher solar share could be achieved by over-dimensioning the high pressure steam turbine. However, this would lead to efficiency penalty during the times without solar steam production.

In Concepts 1 and 2, both the thermal and net efficiency of the hybrid plant decreases from the initial values of 38.1% and 35.1%, respectively, due to the solar steam integration. This reduction is caused by the imbalance between the different turbine sections; increased steam mass flow through the intermediate and low pressure turbine sections with respect to high pressure turbine section decreases the efficiency, because they have lower isentropic efficiency than high pressure turbine section. The more solar steam is fed to the system, the more different heat surfaces of the steam boiler and turbine sections are imbalanced. Thus, the efficiency penalty is higher in Concept 2 than in Concept 1. In Concept

3, the efficiencies in turn increase, since the steam mass flow through the high pressure turbine section increases. Even higher efficiencies could be reached if the design live steam and reheated steam temperatures could be maintained throughout the day. The efficiency of subsystems should be optimized according to the selected process configuration, as the design details and interdependencies define the maximum fuel and CO_2 emission savings instead of the achieved solar share.

Table 12. Summary of achieved thermal and net solar shares, thermal and net efficiencies of the hybrid plant, and fuel and emission savings in three different hybrid configurations.

	Concept 1	Concept 2	Concept 3
Thermal solar share	5.3%	19.7%	34.1%
Net solar share	4.9%	18.2%	31.9%
Thermal efficiency	38.0%	37.4%	38.5%
Net efficiency	35.0%	34.6%	35.9%
Fuel and emission savings	4.6%	16.8%	33.6%

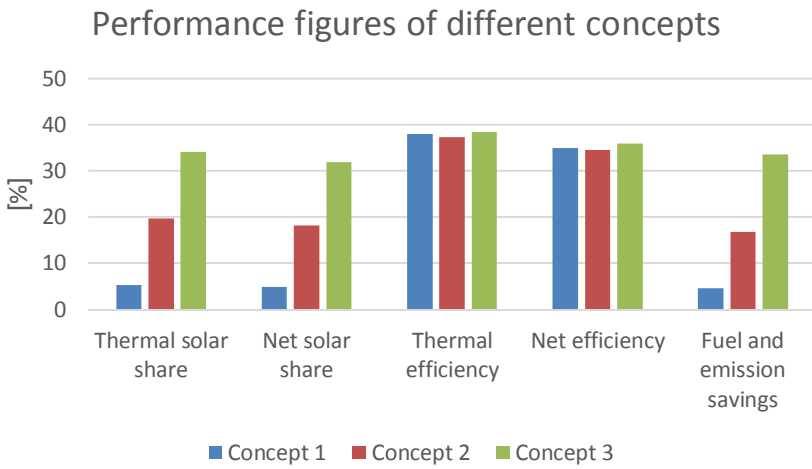

Figure 123. Main performance figures of different hybrid concepts.

7.3 Configuration considerations and recommendations

Different solar steam connection points to the power block and extraction points of feedwater to the solar field lead to varying hybrid configurations. In the case of feed water preheating configuration (Concept 1), the achievable solar share is rather low compared to expected investment costs, and consequently the option does not look like very attempting investment. However, this might be the only option in retrofit plants if only small changes in the power block are desired. If higher solar share is aimed in a retrofit plant, the design of the boiler heat transfer

surfaces and the plant operation become critical questions. Cold reheat line configuration (Concept 2) and high pressure turbine configuration (Concept 3) with significant solar shares are easier and more robust to adapt in greenfield hybrid plant than in retrofitted plant, as the plant can be designed for the solar integration from the beginning.

The results of hybrid case studies show that it is challenging to achieve very high solar shares and related emission reductions (Chapters 6.2.2, 6.3.2 and 6.4.2), e.g. at least 33% reduction compared to the reference coal-fired power plant required according to the emission performance standards. Only in the case of Concept 3, the emission reductions (33.6%) temporarily exceeded the target of the emission performance standards. However, this reduction is achieved only during the peak solar irradiation conditions, and the annual reduction is significantly lower. This is far from the over 40% reduction needed for the current average coal-fired power plants. However, the feasibility of the integration depends on the emission reduction targets. Also other factors, such as the fuel and CO_2 prices must be taken into account.

The concepts studied were operated with fuel saving mode, in which the power production is maintained the same, while the boiler capacity is reduced according to the solar steam production. In order to achieve higher solar share, the two operation modes, fuel saving mode and power boost mode, should be combined. This avoids overloading and over-dimensioning the plant components.

In the case of coal-fired power plant, fuel saving mode seems to be the most feasible option for the operation mode, since this reduces the fuel consumption and emissions. However, significant reductions in the existing plants are challenging to achieve. Power boost mode or the combination of the two operation modes is foreseen to be feasible option in biomass-fired power plants, in which the availability of affordable biomass resources might be the restricting issue for reliable production in sun-rich regions.

Concepts 1 and 2 were able to compensate or could compensate with minor control system development the changes in solar thermal production in transient irradiance cases (Chapters 6.2.3, 6.3.3 and 6.4.3). The DNI step change of 70% with 50%/min speed was challenging to manage in Concept 3. Several cloud passages in a short time period can create even more challenging situations for the hybrid operation and controls. However, there are some development steps, which could make the concept technically feasible. By applying more advanced controls, e.g. model predictive control (MPC), and by integrating DNI forecasting to the system the variations in the solar steam production could be compensated better than in the current model, which applies simple PI controllers.

The results make the thermal energy storage integration to the plant a viable option. This would allow more stable operation of the boiler, since the natural diurnal variability in the solar steam production could be levelized over the day and the sudden changes in irradiation could be compensated. The storage integration would simplify the design of the heat transfer surfaces, different turbine sections and other components, since solar energy could be utilized more evenly and radical part load situations could be avoided. This also allows operating the plant in

the most optimal operational range and with constantly higher solar share. The challenge in the storage integration is that techno-economically feasible storage options for direct steam generating solar fields are still under development phase. One option is to apply for example molten salt both as the heat transfer fluid and directly as a storage medium.

Acknowledgements

This work was carried out in the COMBO-CFB (Combination of Concentrated Solar Power with Circulating Fluidized Bed Power Plants) research project (40066/14) coordinated by VTT Technical Research Centre of Finland Ltd. with funding from the Finnish Funding Agency for Technology and Innovation, Tekes.

References

Agrafiotis, C., von Storch, H., Roeb, M. & Sattler, C. 2014. Solar thermal reforming of methane feedstocks for hydrogen and syngas production – A review. Renewable and Sustainable Energy Reviews 29(2014), 656–682.

Agrafiotis, C., Roeb, M. & Sattler, C. 2015. A review on solar thermal syngas production via redox pair-based water/carbon dioxide splitting thermochemical cycles. Renewable and Sustainable Energy Reviews 42(2015), 254–285.

Ahn, Y., Bae, S.J., Kim, M., Cho, S.K., Baik, S., Lee, J.I. & Cha, J.E. 2015. Review of supercritical CO_2 power cycle technology and current status of research and development. Nuclear Engineering and Technology 47(2015), 647–661.

Alguacil, M., Prieto, C., Rodriquez, A. & Lohr, J. 2014. Direct steam generation in parabolic trough collectors. Energy Procedia 49(2014), 21–29.

Al-Maliki, W.A.K., Alobaid, F., Kez, V. & Epple, B. Modelling and dynamic simulation of a parabolic trough power plant. Journal of Process Control 39(2016), 123−138.

Amin, A.M., Croiset, E. & Epling, W. 2011. Review of methane catalytic cracking for hydrogen production. International Journal of Hydrogen Energy 36(2011), 2904–2935.

Apros. 2016a. Process Simulation Software. Nuclear and Thermal Power Plant Applications. Available at (cited 30.08.2016): http://www.apros.fi/en

Apros. 2016b. Apros® Datasheet Thermal Hydraulicss Modelling. Available at (cited 30.08.2016): http://www.apros.fi/filebank/209-Apros_Datasheet_Thermal_Hydraulics_Modelling.pdf

Arena. 2016. Kogan Creek Solar Boost project. Available at (cited 03.10.2016): http://arena.gov.au/project/kogan-creek-solar-boost-project/

AREVA Solar. 2010. Liddell Solar Thermal Station. Available at (cited 03.10.2016): http://www.areva.com/mediatheque/liblocal/docs/activites/energ-renouvelables/Areva_Liddell_flyer_HR.pdf

AREVA Solar. 2011a. Kogan Creek Solar Boost Project. Available at (cited 03.10.2016): http://www.areva.com/mediatheque/liblocal/docs/activites/energ-renouvelables/pdf-solar-kogan-creek-2011-va.pdf

AREVA Solar, 2011b. Kimberlina Solar Thermal Power Plant. Available at (cited 12.9.2016): http://www.areva.com/mediatheque/liblocal/docs/activites/energ-renouvelables/Areva_Kimberlina_flyer.pdf

AREVA Solar. 2012. Sundt Solar Boost Project. Available at (cited 03.10.2016): http://www.areva.com/arevasolar/liblocal/docs/TEP-Sundt_Solar_Boost_%20Project-Keyfact.pdf

Barlev, D., Vidu, R. & Stroeve P. Innovation in concentrated solar power. Solar Energy Materials & Solar Cells 95(2011), 2703–2725.

Birnbaum, J., Eck, M., Fichtner, M., Hirsch, T., Lehmann, D. & Zimmermann, G. 2010. A direct steam generation solar power plant with integrated thermal storage. Solar Energy Engineering 132(2010).

Birnbaum, J., Feldhoff, J.F., Fichtner, M., Hirsch, T., Jöcker, M., Pitz-Paal, R. & Zim-mermann, G. 2011. Steam temperature stability in a direct steam generation solar power plant. Solar Energy 85(2011), 660–668.

Boerema, N., Morrison, G., Taylor, R. & Rosengarten, G. 2012. Liquid sodium versus Hitec as a heat transfer fluid in solar thermal central receiver system. Solar Energy 86(2012), 2293–2305.

Böhmer, M., Langnickel, U. & Sanchez, M. 1991. Solar steam reforming of methane, Solar Energy Materials 24(1991), 441–448.

Canadian Environmental Protection Act. 2016. Reduction of Carbon Dioxide Emissions from Coal-fired Generation of Electricity Regulations, 58p. Available at (cited 02.08.2016): http://laws-lois.justice.gc.ca/PDF/SOR-2012-167.pdf

Coco-Enríquez, L., Muñoz-Antón, J. & Martínez-Val, J.M. 2013. Innovations on direct steam generation in linear Fresnel collectors. In proceedings of SolarPACES 2013 annual conference.

Conlon, W., Johnson, P. & Hanson, R. 2011. Superheated steam from CLFR solar steam generators. Proceedings of the ASME 2011 Power Conference, Denver, Colorado, USA, 12-14 July 2011, 301–307.

Cot, A., Ametller, A., Vall-Llovera, J., Aguiló, J. & Arqué, J.M. Termoborges Solar: A Thermosolar Hybrid Plant with Biomass. 2010. Proceedings of Third International Symposium on Energy from Biomass and Waste, Venice, Italy, 8-11 November 2010, 1–5.

CSP Today. 2016. Saudi Arabia's first ISCC plant to set record low CSP cost. February 2016. Available at (cited 03.10.2016):

http://analysis.newenergyupdate.com/csp-today/technology/saudi-arabias-first-iscc-plant-set-record-low-csp-cost

CSP World. 2015. CSP World Map. Available at (cited 03.10.2016): http://www.cspworld.org/cspworldmap

Da Costa Coelho. 2014. Study of a hybrid concentrating solar power for Portuquese conditions. PhD thesis, University of Porto 2014, 1–218.

Dostal, V. 2004. A supercritical carbon dioxide cycle for the next generation nuclear reactors. PhD thesis, Department of Nuclear Engineering, Massachusetts Institute of Technology, U.S.

Dyreby, J.J., Klein, S.A., Nellis, G.F. & Reindl, D.T. 2011. Modeling off-design operation of a supercritical carbon dioxide Brayton cycle. Supercritical CO_2 Power Cycle Symposium, Boulder, Colorado, U.S., May 24-25, 2011, 1−9.

Eck, M., Schmidt, H., Eickhoff, M. & Hirsch, T. 2007. Field Test of Water-Steam Separators for Direct Steam Generation in Parabolic Troughs. Journal of Solar Energy Engineering 130(2007), 1–9.

European Investment Bank. 2013. EIB Emission performance standard. Available at (cited 01.08.2016): http://www.eib.org/attachments/consultations/elp_methodology_emission_performance_standard_20130722_en.pdf

Feng, L., Chen, H., Zhou, Y., Zhang, S., Yang, T. & An, T. 2016. The development of a thermo-economic evaluation method for solar aided power generation. Energy Conversion and Management 116(2016), 112–119.

Fernández-García, A., Zarza, E., Valenzuela, L., Pérez, M. 2010. Parabolic-trough solar collectors and their applications. Renewable and Sustainable Energy Reviews 14(2010), 1695–1721.

FPL. 2016. Ten Year Power Plant Site Plan 2016−2025. April 2016. Available at (cited 03.10.2016): https://www.fpl.com/company/pdf/10-year-site-plan.pdf

FRENELL. Solar Power on Demand: Least Cost Opportunity for Sun-rich Countries. Available at (cited 15.2.2017): https://issuu.com/frenellgmbh/docs/frenell_white_paper_v1.0_may_2016_a?e=25146816/36095820

Gálvez, M.E., Loutzenhiser, P.G., Hischier, I. & Steinfeld, A. 2008. CO2 Splitting via Two-Step Solar Thermochemical Cycles with Zn/ZnO and FeO/Fe_3O_4

Redox Reactions: Thermodynamic Analysis, Energy & Fuels 22(2008), 3544–3550.

Grena, R. & Tarquini, P. 2011. Solar linear Fresnel collector using molten nitrates as heat transfer fluid. Energy 36(2011), 1048−1056.

Guerrero-Lemus, R.; Martínez-Duart, J.M. 2013. Concentrated Solar Power. Renewable Energies and CO_2. Lecture Notes in Energy 3. Springer-Verlag London 2013.

Gupta, M.K. & Kaushik, S.C. 2009. Exergetic utilization of solar energy for feed water preheating in a conventional thermal power plant. International Journal of Energy Research 33(2009), 593–604.

Hakkarainen, E. & Tähtinen, M. 2015a. Dynamic model development of Linear Fresnel Solar Field. ASME 2015 9th International Conference on Energy Sustainability, ASME 2015 Power & Energy, San Diego, USA, June 28 − July 2, 2015, 1−11.

Hakkarainen, E. & Tähtinen. M. 2015b. Dynamic modelling and simulation of linear Fresnel solar field model based on molten salt heat transfer fluid. SolarPACES 2015, Cape Town, South Africa, October 13-16, 2015, 1−8.

Hakkarainen, E., Sihvonen, T. & Lappalainen, J. 2016a. Dynamic simulation of two concentrated solar power concepts with supercritical CO_2 Brayton cycle. 1st European Seminar on Supercritical CO2 Power Systems, Vienna, Austria, September 29 − 30, 2016, 1−5.

Hakkarainen, E., Sihvonen, T. & Lappalainen J. 2016b. Dynamic modelling and simulation of CSP plant based on supercritical carbon dioxide closed Brayton cycle. SolarPACES 2016, Abu Dhabi, United Arab Emirates, October 11-14, 2016, 1−9.

HeliosCSP, 2011. Iran – Yazd integrated solar combined cycle power station. Available at (cited 03.10.2016): http://helioscsp.com/iran-yazd-integrated-solar-combined-cycle-power-station/

Henrion, T., Ponweiser, K., Band, D. & Telgen, T. Dynamic simulation of a solar power plant steam generation system. Simulation Modelling Practice and Theory 33(2013), 2−17.

Hirsch, T., Feldhoff, J., Hennecke, K. & Pitz-Paal, R. 2014. Advancements in the Field of Direct Steam Generation in Linear Solar Concentrators – A Review. Heat Transfer Engineering 35(2014), 258–271.

Hong-juan, H., Zhen-yue, Y., Yong-ping, Y., Si, C., Na, L. & Junjie, W. 2013. Performance evaluation of solar aided feedwater heating of coal-fired power

generation (SAFHCPG) system under different operating conditions. Applied Energy 112(2013), 710–718.

Hu, E., Yang, Y, Nishimura, A., Yilmaz, F. & Kouzani, A. 2010. Solar thermal aided power generation. Applied Energy 87(2010), 2881–2885.

Hänninen M. & Ylijoki, J. 2008. The one-dimensional separate two-phase flow model of APROS, VTT Research notes (2008), 1–61.

Ibrik, K., Al-Meer, M. & Ozalp, N. 2012. Catalytic Solar Thermochemical Processing for Enhance Heat Transfer and Emission-free Production of Hydrogen. Chemical Engineering Transactions 29(2012), 499–504.

International Energy Agency (IEA). 2014. Technology Roadmap – Solar Thermal Electricity. 2014 Edition. France. 52 p. Available at (cited 4.10.2016): http://www.iea.org/publications/freepublications/publication/TechnologyRoadmapSolarThermalElectricity_2014edition.pdf

International Energy Agency (IEA). 2015. World Energy Outlook 2015. France: International Energy Agency. 580 p. + app. 104 p.

International Renewable Energy Agency (IRENA). June 2012. Renewable Energy Technologies: Cost Analysis Series − Concentrating Solar Power. Volume 1: Power Sector. Issue 2/5. Available in: http://www.irena.org/documentdownloads/publications/re_technologies_cost_analysis-csp.pdf

International Renewable Energy Agency (IRENA). January 2015. Biomass for Heat and Power, Technology Brief. Available in: http://www.irena.org/DocumentDownloads/Publications/IRENA-ETSAP_Tech_Brief_E05_Biomass%20for%20Heat%20and%20Power.pdf

Kalogirou, S.A. 2014. Solar Energy Engineering − Processes and Systems, 2nd ed., Elsevier, 762 p.

Kearney, D., Herrmann, U., Nava, P., Kelly, B., Mahoney, R., Pacheco, J., Cable, R., Potrovitza, N., Blake, D. & Price, H. 2003. Assessment of a Molten Salt Heat Transfer Fluid in a Parabolic Trough Solar Field. Journal of Solar Energy Engineering 125(2003), 1–7.

Kettunen, A., Kovacs, J., Nuortimo, K., Parkkonen, R. & Jäntti, T. 2014. The Latest CFB Technology Developments for Flexible Large Scale Utility Power Production, Foster Wheeler Energia Oy, Finland. Available at (cited 01.08.2016):

http://archive.amecfw.com/file.axd?pointerID=55a7ba518b0c1e0e04f12141&sid=635726523699110000

Kim, J., Kim, J.S & Stein, W. Simplified heat loss model for central tower solar receiver. Solar Energy 116(2015), 314–332.

Kodama, T., Kondoh, Y., Tamagawa, T., Funatoh, A., Shimizu, K.I. & Kitayama, Y. 2002. Fluidized bed coal gasification with CO_2 under direct irradiation with concentrated visible light, Energy and Fuels 16(2002), 1264–1270.

Kodama, T. & Gokon, N. 2007. Thermochemical cycles for high-temperature solar hydrogen production, Chemical Reviews 107(2007), 4048–4077.

Kovács, J., Kettunen, A., Ikonen, E., Hultgren, M. & Niva, L. 2015. Addressing the Challenge of Fast Load Change Requirements. 22nd International Conference of Fluidized Bed Conversion, Turku Finland, June 14-17, 1–11.

Laing, D., Bahl, C., Bauer, T., Lehmann, D. & Steinmann, W. 2011. Thermal energy storage for direct steam generation, Solar Energy 85(2011), 627–633.

Lappalainen, J., Blom, H. & Juslin, K. 2012. Dynamic process simulation as an engineering tool – A case of analysing a coal plant evaporator. VGB Powertech 1-2(2012), 62–68.

Ma, Z. & Turchi, C.S. 2011. Advanced Supercritical Carbon Dioxide Power Cycle Configurations for Use in Concentrating Solar Power Systems.

Maag, G., Zanganeh, G. & Steinfeld, A. 2009. Solar thermal cracking of methane in a particle-flow reactor for the co-production of hydrogen and carbon. International Journal of Hydrogen Energy, 34(2009), 7676–7685.

Maccari, A., Bissi, D., Casubolo, G., Guerrini, F., Lucatello, L., Luna, G., Rivaben, A., Savoldi, E., Tamano, S. & Zuanella, M. 2015. Archimede Solar Energy Molten Salt Parabolic Trough Demo Plant: A Step Ahead towards the New Frontiers pf CSP. Energy Procedia 69(2015), 1643–1651.

Meier A. & Steinfeld A. 2012. Solar Energy in Thermochemical Processing. In: Robert A. Meyers ed. Encyclopedia of Sustainability Science and Technology, Springer New York 2012, 9588–9619.

Morin, G., Mertins, M., Kirchberger, J. & Selig, M. 2011. SuperNova – Construction, control & performance of steam superheating linear Fresnel collector.

Morin, G., Dersch, J., Platzer, W., Eck, M. & Häberle, A. 2012 a. Comparison of Linear Fresnel and Parabolic Trough Collector power plants. Solar Energy 86(2012), 1–12

Morin, G., Kirchberger, J., Lemmertz, N. & Mertins, M. 2012 b. Operational results and simulation of a superheating Fresnel collector.

Morin, G., Karl, M., Mertins, M. & Selig, M. 2015. Molten Salt as a Heat Transfer Fluid in a Linear Fresnel Collector − Commercial Application backed by Demonstration. Energy Procedia 69(2015), 689–698.

Müller-Steinhagen, H. 2013. Concentrating solar thermal power. Philosophical Transactions of the Royal Society A 371(1996), 20110433.

Noone, C.J., Torrilhon, M. & Mitsos, A. Heliostat field optimization: A new computationally efficient model and biomimetic layout. Solar Energy 86(2012), 792–803.

Novatec Solar. Turnkey Solar Boiler, based on Fresnel Collector Technology, mass produced in industrial precision with performance guarantee.

Novatec Solar. 23.7.2013. SAM Linear Fresnel solar boiler model. Webinar.

Novatec Solar. 2016. Liddell in Australia. Available at (cited 01.08.2016): http://www.novatecsolar.com/80-1-Liddell.html

NREL. 2016. Concentrating Solar Power Projects. Available at (cited 02.08.2016): http://www.nrel.gov/csp/solarpaces/index.cfm

NREL. Project profile: 10-megawatt supercritical carbon dioxide turbine. Available at (cited 16.02.2017): http://energy.gov/eere/sunshot/project-profile-10-megawatt-supercritical-carbon-dioxide-turbine-csprd

Paska, J., Biczel, P. & Kłos, M. 2009. Hybrid power systems - An effective way of utilising primary energy sources. Renewable Energy 34(2009), 2414–2421.

Paxman, D., Trottier, S., Nikoo, M., Secanell, M. & Ordorica-Garcia, G. 2014. Initial experimental and theoretical investigation of solar molten media methane cracking for hydrogen production, Energy Procedia 49(2014), 2027–2036.

Perret, R. 2011. Thermochemical Cycle Selection and Investment Priority. Solar Thermochemical Hydrogen Production Research (STCH), SANDIA REPORT, SAND2011-3622, Unlimited Release, Printed May 2011.

Peterseim, J.H., White, S., Tadros, A. & Hellwig, U. 2013. Concentrated solar power hybrid plants, which technologies are best suited for hybridisation? Renewable Energy 57(2013), 520–532.

Peterseim, J.H., White, S., Tadros, A. & Hellwig, U. 2014a. Concentrating solar power hybrid plant – Enabling cost effective synergies. Renewable Energy 67(2014), 178–185.

Peterseim, J.H., Tadros, A., White, S., Hellwig, U., Landler, J. & Galang, K. 2014b. Solar tower-biomass hybrid plants - Maximizing plant performance, Energy Procedia 49(2014), 1197–1206.

Petrov, M., Popa, M. & Fransson, T. 2012. Solar augmentation of conventional steam plant: from system studies to reality. World Renewable Energy Forum, Denver, Colorado, USA, 1–8.

Popov D., An option for solar thermal repowering of fossil fuel fired power plants, Solar Energy 85(2011) 344–349.

Piatkowski, N., Wieckert, C. & Steinfeld, A. 2009. Experimental investigation of a packed-bed solar reactor for the steam-gasification of carbonaceous feedstocks, Fuel Processing Technology, 90(2009) 360–366.

Piatkowski, N., Wieckert, C., Weimerc, A.W. & Steinfeld, A. 2011. Solar-driven gasification of carbonaceous feedstock − a review, Energy & Environmental Science 4(2011), 73–82

Pierce, W., Gauché, P., Backström, T., Brent, A & Tadros, A. 2013. A comparison of solar aided power generation (SAPG) and stand-alone concentrating solar power (CSP): A South African case study. Applied Thermal Engineering 61(2013), 657–662.

Puig-Arnavat, M., Tora, E.A., Bruno, J.C. & Coronas, A. 2013. State of the art on reactor designs for solar gasification of carbonaceous feedstock, Solar Energy 97(2013), 67–84.

Raiko, R. & Saarenpää, I. 2013. Höyrytekniikka, Luentomoniste, Tampereen teknillinen yliopisto, Voimalaitos ja polttotekniikan laitos, 254 p.

Rayaprolu, K. 2009. Boilers for Power and Process, CRC Press, USA, 694 p.

Reliance Power Ltd. 2014 Media release: Reliance Power's 100 MW concentrated solar power (CSP) project at Dhursar, Rajastan commences generation. Available at (cited 04.10.2016): http://www.reliancepower.co.in/1100/100_MW_CSP_Plant-2014-11-11.pdf

Relloso, S. & García, E. 2014. Tower technology cost reduction approach after Gemasolar experience. SolarpACES 2014, Beijing, China, September 16–19, 2014.

Rodat, S., Abanades, S. & Flamant, G. 2009. High-temperature solar methane dissociation in a multitubular cavity-type reactor in the temperature range 1823–2073 K. Energy Fuels 23(2009), 2666–2674.

Romero-Alvarez, M. & Zarza, E. 2007. Concentrating solar thermal power. In: Kreith, F.Goswami, D.Y. (eds) Handbook of energy efficiency and renewable energy. CRC Press, Boca Raton.

Sandia National Laboratories. 21.10.2015. University of Wisconsin – Sandia Team Awarded SunShot CSP: APOLLO Funding. Available at (cited 16.02.2017): http://energy.sandia.gov/university-of-wisconsin-sandia-team-awarded-sunshot-csp-apollo-funding/

Sandia National Laboratories, Supercritical CO2-Brayton Cycle. Available at (cited 15.02.2017): http://energy.sandia.gov/energy/renewable-energy/supercritical-co2/

Schenk, H. & Eck, M. 2012. Yield Analysis for Parabolic Trough Solar Thermal Power Plants – A Basic Approach. Germany: DLR. 82 p.

Schenk, H., Hirsch, T., Feldhoff, J.F. & Wittmann, M. Energetic Comparison of Linear Fresnel and Parabolic Trough Collector Systems. Journal of Solar Energy Engineering 136(2014), 041015.

Scherer, V., Roth, K. & Eck, M. Process dynamics of fossil steam power plants induced by the integration of transient solar heat. 2004 New and Renewable Energy Technologies for Sustainable Development. World Scientific Publishing Co. Pte. Ltd.

Schott Solar. Schott PTR®70 Receivers. Available in: http://www.schott.com/d/csp/370a8801-3271-4b2a-a3e6-c0b5c78b01ae/1.0/schott_ptr70_4th_generation_brochure.pdf

Selig, M. & Mertins, M. 2010. From saturated to superheated direct solar steam generation – technical challenges and economical benefits.

Sharma, M., Parvareh, F. & Abbas, A. 2015. Highly integrated post-combustion carbon capture process in a coal-fired power plant with solar repowering. International Journal of Energy Research 39(2015), 1623–1635.

Siemens. 2011. Steam turbines for CSP plants, Siemens AG, Germany. Available at (cited 30.09.2016): http://www.energy.siemens.com/hq/pool/hq/power-generation/steam-turbines/downloads/steam-turbine-for-csp-plants-siemens.pdf

Simakov, D.S.A., Wright, M.M., Ahmed, S., Mokheimerd, E.M.A. & Román-Leshkov, Y. 2015. Solar thermal catalytic reforming of natural gas: a review on chemistry, catalysis and system design. Catalysis Science & Technology 5(2012), 1991–2016.

Singh, R., Miller, S.A., Rowlands, A.S. & Jacobs, P.A. 2013. Dynamic characteristics of a direct-heated supercritical carbon-dioxide Brayton cycle in a solar thermal power plant. Energy 50(2013), 194–204.

SoDa, Solar radiation data. Solar Energy Services for Professionals. Available in: http://www.soda-is.org/eng/services/service_invoke/gui.php?xml_descript=soda_tl.xml&Submit2=Month

SolarPACES. 2016. CSP Projects Around the World. Available at (cited 02.08.2016): http://www.solarpaces.org/csp-technology/csp-projects-around-the-world

Steinfeld, A. & Meier, A. 2004. Solar Fuels and Materials, Encyclopedia of Energy 5(2004), 623–637.

Suojanen, S., Hakkarainen, E., Kettunen, A., Kapela, J., Paldanius, J., Tuononen, M., Selek, I., Kovács, J. & Tähtinen, M. 2016. Integration of concetrated solar power (CSP) and circulating fluidized bed (CFB) power plants − Final results of the COMBO-CFB project. SolarPACES 2016, Abu Dhabi, United Arab Emirates, October 11-14, 2016, 1−8.

Suojanen, S., Hakkarainen, E., Tähtinen, M. & Sihvonen, T. 2017. Modeling and analysis of process configurations for hybrid concentrated solar power and conventional steam power plants. Energy Conversion and Management 134(2017), 327–339.

Suresh, M.V.J.J., Reddy, K.S. & Kumar, A.K. 2010. 4-E (Energy, Exergy, Environment, and Economic) analysis of solar thermal aided coal-fired power plants. Energy for Sustainable Development 14(2010), 267–279.

Teir, S. 2002. Modern boiler types and applications, Steam boiler technology, Energy Engineering and Environmental Protection Publications, Department of Mechanical Engineering, Helsinki University of Technology, Espoo, 15 p.

Trommer, D., Noembrinia, F., Fasciana, M., Rodriguez, D., Morales, A. Romero, M. & Steinfeld, A. 2005. Hydrogen production by steam-gasification of petroleum coke using concentrated solar power – I. Thermodynamic and kinetic analyses. International Journal of Hydrogen Energy 30(2005), 605–618.

Valenzuela, L., Zarza, E., Berenguel, M. & Camacho, E.F. 2006. Control scheme for direct steam generation in parabolic troughs under recirculation operation mode. Solar Energy 80(2006), 1−17.

Vignarooban, K., Xu, X., Arvay, A., Hsu, K. & Kannan, A.M. 2015. Heat transfer fluids for concentrating solar power systems – A review. Applied Energy 146(2015), 383–396.

Yan, Q., Yang, Y., Nishimura, A., Kouzani, A. & Hu, E. 2010. Multi-point and Multi-level Solar Integration into a Conventional Coal-fired Power Plant. Energy Fuels 24(2010), 3733–3738.

Yan, Q., Hu, E., Yang, Y. & Zhai, R. 2011. Evaluation of solar aided thermal power generation with various power plants. International Journal of Energy Research 35(2011), 909–922.

Zhu, G., Wendelin, T., Wagner, M. & Kutscher, C. 2014. History, current state, and future of linear Fresnel concentrating solar collectors. Solar Energy 103(2014), 639–652.

Appendix A: Characteristics of hybrid CSP plants

Table 13. Integrated solar combined cycle (ISCC) plants (Adapted from CSP World 2015).

CSP technology: Parabolic Trough					
Name	HTF	Solar [MW_e]	Combined cycle [MW_e]	Status	Country
Agua Prieta II ISCC	Thermal oil	14.0	464.0	Under Construction	Mexico
Aïn Beni Mathar ISCC	Thermal oil	20.0	450.0	Operational	Morocco
Al Abdaliyah Integrated Solar Combined Cycle (ISCC)	N/A	60.0	220.0	Development	Kuwait
Archimede	Molten salt	5.0	130.0	Operational	Italy
Duba 1 ISCC [1]	N/A	43.0 [1]	562.0 [2]	Under Construction	Saudi Arabia
Hassi R'mel ISCC	Thermal oil	25.0	125.0	Operational	Algeria
Kuraymat ISCC	Thermal oil	20.0	120.0 [1]	Operational	Egypt
Martin Next Generation Solar Energy Center	Thermal oil	75.0	1225.0 [3]	Operational	USA
Medicine Hat ISCC	N/A	1.0	66.0	Operational	Canada
Ningxia ISCC	N/A	92.0	N/A	Under Construction	China
Palmdale Hybrid Power Plant	Thermal oil	50.0	520.0	Planned	USA
Victorville 2 Hybrid Power Plant	N/A	50.0	513.0	Planned	USA
Yazd ISCC	N/A	17.0	450.0 [4]	Operational	Iran

[1] (NREL, 2016)

[2] (CSP Today, 2016)

[3] (FPL, 2016)

[4] (HeliosCSP, 2011)

CSP technology: Linear Fresnel					
Name	HTF	Solar [MW_e]	Combined cycle [MW_e]	Status	Country
Collinsville Hybrid CSP-gas project	N/A	30.0	N/A	Planned	Australia
CSP technology: Central Receiver					
Name	HTF	Solar [MW_e]	Combined cycle [MW_e]	Status	Country
El Borma ISCC	N/A	5.0	38.0	Planned	Tunisia

Table 14. Hybrid solid fuel-fired power plants (Adapted from CSP World 2015).

CSP technology: Parabolic Trough						
Name	HTF	Solar [MW_e]	Fuel	Solid fuel-fired [MW_e]	Status	Country
Cameo	Thermal oil	2.0	Coal	N/A	Decommissioned	USA
Termosolar Borges	Thermal oil	22.5	Biomass/gas	44.0 MW_{th} [1]	Operational	Spain

[1](NREL, 2016)

CSP technology: Linear Fresnel						
Name	HTF	Solar [MW_e]	Fuel	Solid fuel-fired [MW_e]	Status	Country
Liddell Power Station	Water	6.0	Coal	2000.0 [1]	Operational	Australia
Kogan Creek	Water	44.0	Coal	750.0 [2]	Withdrawn [3]	Australia
Sundt Solar Boost	Water [4]	5.0	Coal /gas [4]	156.0 [4]	Development	USA

[1](AREVA Solar, 2010)

[2](AREVA Solar, 2011a)

[3](Arena, 2016)

[4](AREVA Solar, 2012)

CSP technology: Central Receiver						
Name	HTF	Solar [MW_e]	Fuel	Solid fuel-fired [MW_e]	Status	Country
PTC50 Alvarado	N/A	50.0	Biomass	N/A	Development	Spain

Appendix B: State points of the Apros CFB steam power plant model

Table 15. State point information of the Apros steam cycle.

Point (Figure 64)	Pressure (bar)	Temperature (°C)	Mass flow (kg/s)
1	120.0	530.0	103.3
2	34.5	351.2	96.3
3	32.6	530.0	101.7
4	12.9	392.8	91.4
5	0.15	53.9	79.2
6	0.43	45.2	95.2
7	13.8	44.9	95.2
8	12.6	71.0	95.2
9	11.6	110.0	95.2
10	10.6	147.1	95.2
11	10.2	151.2	108.7
12	148.6	153.8	95.2
13	144.8	201.0	95.2
14	142.4	237.1	95.2
15	128.9	316.7	95.2
16	128.8	330.0	95.2
17	33.0	349.7	7.0
18	22.6	473.9	6.6
19	5.6	291.5	6.2
20	3.2	235.9	6.1
21	1.8	175.8	4.8

Series title and number

VTT Technology 296

Title	**Concentrated solar power and circulating fluidized bed power plant hybrids** Final results of the COMBO-CFB project
Author(s)	Elina Hakkarainen, Suvi Suojanen, Matti Tähtinen, Toni Pikkarainen, Antton Tapani, Teemu Sihvonen, Markus Hurskainen, Hannu Mikkonen, Jari Lappalainen & Heidi Saastamoinen
Abstract	Concentrated solar power (CSP) is a renewable energy technology, which is able to provide dispatchable power according to demand. Dispatchability is typically achieved by decoupling solar thermal collection and power production with a thermal energy storage system. However, storage solutions for direct steam generating CSP technologies are still in a development phase. Hybrid system, in which solar field is integrated to a conventional power plant, is another option to produce renewable load-following power. The main idea in a hybrid system is to compensate the variation in solar thermal production with the steam boiler. In addition to dispatchable nature of power production, hybrid system offers several other possible benefits with respect to stand-alone CSP plant, such as reduced fuel consumption and emissions, enhanced plant efficiency and reduced production costs. However, the highly dynamic nature of the process imposes some challenges for the design and operation of the system, in particular in the case of significant solar share. Dynamic analysis of the system is foreseen to be utmost important in the plant design phase in order to take into account all the dynamic interactions in the process, which could affect for example the balance of different boiler heat transfer surfaces and turbine sections. The project "Combination of Concentrated Solar Power (CSP) with Circulating Fluidized Bed (CFB) power plants" (COMBO-CFB) aimed at developing innovative, flexible and high-efficient hybrid concept, which is able to balance the distributed intermittent production. The concept development included both experimental work and dynamic modelling and simulation. The research focused on the capacity building in terms of different CSP technologies, hybrid concepts and thermochemical processes, and in technical feasibility of the hybrid concepts, including the benefits provided by different concepts, challenges and possible future improvements. Three different hybrid concepts were studied in detail, namely: 1) Feedwater preheating concept, 2) Cold reheat line concept, and 3) High pressure turbine concept.
ISBN, ISSN, URN	ISBN 978-951-38-8531-1 (URL: http://www.vttresearch.com/impact/publications) ISSN-L 2242-1211 ISSN 2242-122X (Online) http://urn.fi/URN:ISBN:978-951-38-8531-1
Date	April 2017
Language	English, Finnish abstract
Pages	156 p. + app. 3 p.
Name of the project	Combination of Concentrated Solar Power (CSP) with Circulating Fluidized Bed (CFB) power plants
Commissioned by	Tekes
Keywords	hybrid power plant, concentrated solar power, CSP, circulating fluidized bed boiler, power plant, renewable energy
Publisher	VTT Technical Research Centre of Finland Ltd P.O. Box 1000, FI-02044 VTT, Finland, Tel. 020 722 111

Julkaisun sarja ja numero

VTT Technology 296

Nimeke	**Keskittävän aurinkoenergian ja leijupetikattilan yhdistäminen integroiduksi ratkaisuksi** COMBO-CFB-projektin tuloksia
Tekijä(t)	Elina Hakkarainen, Suvi Suojanen, Matti Tähtinen, Toni Pikkarainen, Antton Tapani, Teemu Sihvonen, Markus Hurskainen, Hannu Mikkonen, Jari Lappalainen & Heidi Saastamoinen
Tiivistelmä	Keskittävä aurinkovoima (Concentrated Solar Power, CSP) on uusiutuva energiateknologia, jolla voidaan tuottaa joustavasti energiaa kulutuksen mukaan. Tyypillisesti laitokseen kytketään lämpövarasto, jonka avulla aurinkolämmön keräys ja sähkön tuotanto voidaan erottaa ja näin tuottaa sähköä riippumatta sen hetkisestä säteilytasosta. Varastoratkaisut CSP-tekniikoille, jotka tuottavat höyryä suoraan aurinkokentällä, ovat kuitenkin vasta kehitysvaiheessa. Hybridilaitos, jossa aurinkokenttä on yhdistetty konventionaalisen voimalaitokseen, on toinen vaihtoehto tuottaa sähköä kulutuksen mukaan. Hybridilaitoksen perusajatuksena on tasapainottaa vaihteleva aurinkoenergian tuotanto höyrykattilalla. Joustavuuden lisäksi hybridi tarjoaa muitakin mahdollisia etuja verrattuna erilliseen CSP-laitokseen, kuten pienentyvän polttoaineen kulutuksen ja päästöt, paremman kokonaishyötysuhteen ja matalammat tuotantokustannukset. Voimalaitosprosessi on kuitenkin hyvin dynaaminen, mikä aiheuttaa haasteita järjestelmän suunnittelulle ja operoinnille, erityisesti silloin jos auringon osuus tuotannosta on mitoitettu suureksi. Laitoksen dynaaminen tarkastelu suunnitteluvaiheessa on erittäin tärkeää, jotta voidaan ottaa huomioon eri osaprosessien väliset kriittiset vuorovaikutukset, jotka voivat vaikuttaa esimerkiksi kattilan lämmönsiirtopintojen ja eri turbiinivaiheiden tasapainoon. "Combination of Concentrated Solar Power (CSP) with Circulating Fluidized Bed (CFB) power plants" -projektin (COMBO-CFB) tavoitteena oli kehittää innovatiivinen, joustava ja tehokas hybridikonsepti, joka voi tasapainottaa vaihtelevaa uusiutuvaa tuotantoa. Konseptin kehitys sisälsi sekä kokeellista tutkimusta että dynaamista mallinnusta ja simulointia. Tutkimus keskittyi erilaisiin CSP-tekniikoihin, hybridikonsepteihin ja termokemiallisiin prosesseihin liittyvän tiedon kartuttamiseen, ja erilaisten hybridikonseptien tekniseen toteutettavuuteen. Tekninen toteutettavuus otti kantaa erilaisten konseptien etuihin, haasteisiin ja mahdollisiin parannusvaihtoehtoihin tulevaisuudessa. Kolmea erilaista konseptia tutkittiin projektissa tarkemmin: 1) Syöttöveden esilämmitys -konsepti, 2) Kylmä välitulistuslinja -konsepti, ja 3) Korkeapaineturbiini -konsepti.
ISBN, ISSN, URN	ISBN 978-951-38-8531-1 (URL: http://www.vtt.fi/julkaisut) ISSN-L 2242-1211 ISSN 2242-122X (Verkkojulkaisu) http://urn.fi/URN:ISBN:978-951-38-8531-1
Julkaisuaika	Huhtikuu 2017
Kieli	Englanti, suomenkielinen tiivistelmä
Sivumäärä	156 s. + liitt. 3 s.
Projektin nimi	Combination of Concentrated Solar Power (CSP) with Circulating Fluidized Bed (CFB) power plants
Rahoittajat	Tekes
Avainsanat	hybridilaitos, keskittävä aurinkovoima, CSP, voimalaitos, leijupetikattila, uusiutuva energia
Julkaisija	Teknologian tutkimuskeskus VTT Oy PL 1000, 02044 VTT, puh. 020 722 111

VTT TECHNOLOGY 296

Concentrated solar power and circulating fluidized bed power plant hybrids

Final results of the COMBO-CFB project

Concentrated solar power (CSP) is a renewable energy technology, which is able to provide dispatchable power according to demand. Dispatchability is typically achieved by decoupling solar thermal collection and power production with a thermal energy storage system. Hybrid system, in which solar field is integrated to a conventional power plant, is another option to produce renewable load-following power. The main idea in a hybrid system is to compensate the variation in solar thermal production with the steam boiler.

The project "Combination of Concentrated Solar Power (CSP) with Circulating Fluidized Bed (CFB) power plants" (COMBO-CFB) aimed at developing innovative, flexible and high-efficient hybrid concept, which is able to balance the distributed intermittent production. The research focused on the capacity building in terms of different CSP technologies, hybrid concepts and thermo-chemical processes, and in technical feasibility of the hybrid concepts, including the benefits provided by different concepts, challenges and possible future improvements.

ISBN 978-951-38-8531-1 (URL: http://www.vttresearch.com/impact/publications)
ISSN-L 2242-1211
ISSN 2242-122X (Online)
http://urn.fi/URN:ISBN:978-951-38-8531-1